Mechano-to-Neural Transduction of the Pacinian Corpuscle

A DISSERTATION
SUBMITTED TO THE FACULTY OF THE
UNIVERSITY OF MINNESOTA
BY

Julia Cecilia Quindlen

IN PARTIAL FULFILLMENT OF THE REQUIREMENTS
FOR THE DEGREE OF
DOCTOR OF PHILOSPHY

Professor Victor H. Barocas

October 2017

Acknowledgements

Thank you to Victor Barocas for meeting with me at the University of Pennsylvania almost six years ago and encouraging me to apply to the University of Minnesota. Thank you for taking me into your lab, even though you didn't have the funding for me, and allowing me to pursue a completely new project that satisfied both my biomechanical and neural research interests. I am incredibly thankful for the opportunity to develop a research project from scratch and your unwavering faith in my ability to do so. Thank you for being a devoted mentor and for always pushing me to be a better researcher, writer, and presenter. Thank you for reading my many paper and thesis drafts, answering my seemingly unending list of questions, and always making yourself available for a conversation or pep talk. Thank you for inspiring me to pursue an academic career and encouraging me along this path, especially in my (many) moments of self-doubt. You have set the bar incredibly high, and I will forever aspire to be the researcher and mentor you are.

Thank you to the Barocas Lab for being a fantastic group to work with over the last five years. Amy, you helped me through graduate school starting from before I even accepted my offer to the University of Minnesota. Your mentorship and guidance helped me navigate the highs and lows of graduate school, from assisting me with coursework during my first year to helping me with my WPE and OPE to teaching me how to write journal articles and give conference presentations. I am so thankful for your friendship both in and out of the lab. My graduate school experience would not have been the same without you. Ellen, thank you for being a fantastic undergrad to work with and for trusting me through the ups and downs of research. I am so excited to watch you succeed as a PhD student at the University of Delaware in the coming years. Rohit, Vahhab, Chris, and Shannen – thank you for making the office a fun place to work. Our Euchre games and office chats were often much-needed distractions during stressful days in the lab. Faisal and Vic, thank you for your never-ending technical help when I first joined the lab and introducing me to the multiscale code and MSI. I owe my immediate productivity to you two – thank you for helping me hit the ground running. Thank you to Hallie, Sara, Tina, Colleen, Inka, and Sarah for being wonderful role models of what it means to be a smart and successful female engineer. You all helped me during my first few years of graduate school, from providing invaluable feedback on my presentations to giving me career and research advice. To the undergraduate and graduate students who have worked on the PC project over the years – Ellen, Abby, Sarah, Nick, Alisha, and Tiffany – thank you for your dedication to the project and the hard work you put into helping this project evolve from Julia Island into a much larger entity.

Thank you to Martha Flanders for your guidance during the first few years of my PhD. I appreciate your patience with me as I learned the neuroscience necessary for my project. Your expertise in neuroscience was critical to helping me fill the gaps in my knowledge and turn my project into a truly interdisciplinary study.

Thank you to my PhD committee members for your guidance and support: Victor Barocas, Patrick Alford, Matthew Johnson, and Rajesh Rajamani. Thank you for your invaluable contributions to my research over the years.

Thank you to Beth Winkelstein, to whom I owe my entire research journey. Thank you for taking me into your lab as a sophomore at the University of Pennsylvania and providing an inclusive and stimulating research environment that allowed me to grow as a researcher and decide to pursue a graduate degree. Thank you for your mentorship during my graduate school search and for introducing me to Victor Barocas and the University of Minnesota. And finally, thank you for welcoming me back into SPRL as a post-doc to continue my research journey.

Thank you to the University of Minnesota for providing the facilities necessary to complete this thesis. I used the Minnesota Supercomputing Institute extensively during my PhD and could not have completed this thesis without their computational support. I used ABAQUS, COMSOL, and MATLAB licenses provided by MSI in many of the chapters of my thesis and relied on MSI's computational power to speed up my simulations. Thank you to the team at the Anatomy Bequest Program and the donors and their families for their generous contribution to scientific research. Thank you to Dr. Amy Moeller for your help in identifying and removing PCs from cadaver hands, making my mechanical experiments on isolated PCs possible. Thank you to the University of Minnesota for providing the financial resources (Interdisciplinary Doctoral Fellowship and Doctoral Dissertation Fellowship) that funded much of my thesis work. Thank you to the IGERT Systems Neuroengineering program for taking me on during my first year, even though my project was different from most of the research in the program. My IGERT support allowed me to attend the Society for Neuroscience conference every year, which was invaluable to my growth as a neuroscientist.

Thank you to the Urban Bean for being my second office. Your delicious coffee, plentiful outlets, and large tables were the perfect combination to enhance my productivity through the many stages of graduate school.

Thank you to all of my friends here in Minneapolis who have made this beautiful city my home. To the Calhoun Beach Run Club – thank you for introducing me to my love of marathon running and always giving me a fun and challenging way to relieve the stress of lab. Thank you to Bach Night for countless fantastic memories over the last five years. Your friendships are some of the greatest gifts that Minneapolis could have given me.

Thank you to my friends who never let distance get in the way of our friendship. To Kim and Beth, who traveled to Minneapolis more times that I can count – your constant visits meant the world to me. Thank you for the time and effort you two put into keeping our friendships strong.

Thank you to my family, who have supported my educational pursuits throughout my entire life. Thank you to my Grandparents, who always prioritized my education, and to my brother Jack, for lending a sympathetic ear to the pains of graduate school (and a place to stay as I kept returning to run the Boston Marathon year after year).

Thank you to my parents for your unwavering support. You encouraged me to leave my east coast comfort zone and move to Minnesota, which truly was the best graduate program for me. Thank you for all of the time you put into visiting me in Minneapolis so I never felt lonely or homesick, especially in the middle of cold Minnesota winters! I am proud to say that I have never met more supportive parents in my life. From your constant encouragement of my academic and research accomplishments to your unparalleled enthusiasm as marathon cheerleaders, you two truly are the best support system I could have asked for. Thank you just doesn't feel like enough.

And finally, thank you to Kiefer. It is impossible to list all of the ways you have helped me through my PhD. You've read all of my papers with deep enthusiasm, provided a shoulder to cry on, picked me up from lab late at night, prepared countless meals for me when I didn't have the time or energy to do so, ran with me at odd hours during incredibly busy weeks, and reminded me of my capabilities when I needed to hear it the most. Thank you for always encouraging me to put my thesis first and taking on more wedding planning responsibilities than most grooms could ever imagine. Thank you for moving to Philadelphia with me so that I can pursue a post-doc. Thank you for the endless support and encouragement, especially during these last few months. I know for a fact that I couldn't have done this without you. At times, it truly felt like you were carrying me through it all. I can't wait to become Dr. Quindlen, but I'm even more excited to become Dr. Hotek.

Dedication

This work is dedicated to my parents, the two most supportive people I have ever known. Without them, none of my achievements, academic or otherwise, would have been possible.

Thank you, Dad, for my engineering brain and thank you, Mom, for my academic curiosity.

Abstract

Cutaneous mechanoreceptors are responsible for our ability to distinguish between different touch modalities and experience the physical world around us. Mechanoreceptors are innervated by afferent mechanosensitive neurons that transduce mechanical stimuli into action potentials and terminate in specialized end organs. The Pacinian corpuscle (PC) has been studied more than any of our other mechanoreceptors due to its large size and ease of identification during dissection. The PC, which is found primarily within the dermis of glabrous skin, responds to low-amplitude, high-frequency vibrations in the 20-1000 Hz range. The PC functions as a bandpass filter to vibrations, an effect attributed to the structural and mechanical complexity of its end organ. The PC contains a central mechanosensitive nerve fiber (neurite) that is encapsulated by alternating layers of flat, epithelial-type cells (lamellae) and fluid. The overarching goal of this thesis was to unify the anatomical and electrophysiological observations of the PC via a detailed mechanistic model of PC response to mechanical stimulation, requiring a multiphysics, multiscale approach. First, we developed a multiscale finite-element mechanical model to simulate the equilibrium response of the PC to indentation while accounting for the layered, anisotropic structure of the PC and its deep location within the skin. Next, we developed a three-stage finite-element model of the PC's mechanical and neural responses to a vibratory input that accounted for the lamellar mechanics and neurite electrochemistry. This mechano-neural model was able to simulate the PC's band-pass filtration of vibratory stimuli and rapid adaptation to sustained mechanical stimuli. We then used this model to evaluate the relationship between the PC's material and geometric parameters and its response to vibration and developed dimensionless expressions for the relationship between these parameters and peak frequency or bandwidth. We then embedded multiple mechano-neural PC models within a finite-element model of human skin to simulate the mechanical and neural behavior of a PC cluster *in vivo*. We then performed a literature search to compile the structural parameters of PCs from various species and used our mechano-neural model to simulate the frequency response across species. Finally, we isolated PCs from human cadaveric hands and performed micropipette aspiration experiments to determine an apparent Young's modulus of the PC. The computational and experimental work performed in this thesis contribute to the understanding of the fundamental behavior of mechanoreceptors, which is a necessary first step towards the development of haptic feedback-enabled devices.

Table of Contents

LIST OF TABLES

Chapter 3: A Multiphysics model of the Pacinian corpuscle

Chapter 4: Computational parametric analysis of the mechanical response of structurally varying Pacinian corpuscles

Chapter 5: A finite-element model of mechanosensation by a Pacinian corpuscle cluster in human skin

Chapter 6: Micropipette aspiration of the Pacinian corpuscle

Chapter 7: An inter-species analysis of the Pacinian corpuscle’s frequency sensitivity

LIST OF FIGURES

Chapter 1: Introduction

Chapter 2: Multiscale mechanical model of the Pacinian corpuscle shows depth and anisotropy contribute to the receptor's characteristic response to indentation

Chapter 3: A Multiphysics model of the Pacinian corpuscle

Chapter 4: Computational parametric analysis of the mechanical response of structurally varying Pacinian corpuscles

Chapter 5: A finite-element model of mechanosensation by a Pacinian corpuscle cluster in human skin

Chapter 6: Micropipette aspiration of the Pacinian corpuscle

Chapter 7: An inter-species analysis of the Pacinian corpuscle's frequency sensitivity

CHAPTER 1: INTRODUCTION

1.1 Somatosensation and mechanoreceptors

Touch is essential to our everyday lives. Every physical action performed during a typical day, from simple tasks such as holding a glass of water to a surgeon's dexterous manipulation of tools, requires sensory feedback for successful completion. The sense of touch is mediated by our somatosensory system, which responds to a myriad of mechanical cues from our external world. Mechanoreceptors are responsible for our ability to distinguish between different touch modalities and feel the physical world around us.

Cutaneous mechanoreceptors are sensory neurons that detect a wide range of mechanical stimuli and relay the sensory information about a stimulus from the peripheral nervous system to the somatosensory cortex of the brain via the spinal cord [1]. There are four main types of cutaneous mechanoreceptors that innervate the glabrous (non-hairy) skin, among other regions: Merkel cells, Meissner corpuscles, Ruffini corpuscles, and Pacinian corpuscles (Figure 1.1). These mechanoreceptors are specialized to respond to different mechanical stimuli such as pressure, skin stretch, and vibration, but they can also work in concert to convey a population response about a natural, complex skin stimulus [2–5].

Cutaneous mechanoreceptors are innervated by afferent sensory neurons called low-threshold mechanoreceptors (LTMRs) that respond to non-painful mechanical stimuli [1]. These afferents have cell bodies located in the dorsal root ganglia or cranial sensory ganglia [1]. Merkle cells and Ruffini corpuscles are innervated by slowly adapting afferents of types I and II, respectively, which respond during the sustained portion of a constant skin pressure and have small receptive fields [6–8]. Meissner corpuscles and Pacinian corpuscles are innervated by rapidly adapting types I and II afferents (the latter of which is often referred to as a Pacinian afferent), which exhibit a response to changes in stimulus pressure (i.e. velocity, acceleration) and have large receptive fields [6–8]. While the innervating sensory neuron plays a role in determining the mechanical specialization of each cutaneous mechanoreceptor, the morphology of the tissue surrounding the neuron is also an important factor. A combination of structural, mechanical, and neurophysiological experiments on mechanoreceptors has suggested that the non-neuronal adventitial tissue of the receptor's end organ surrounding the afferent neuron may play an active role in the coupling between skin and the afferent and may be necessary for the receptor's specialized response to mechanical stimuli [9–11]. The study of any mechanoreceptor must therefore combine the electrophysiology of the afferent neuron with the structural and mechanical properties of its encapsulating end organ.

1.2 Pacinian corpuscles

The Pacinian corpuscle (PC; Figure 1.1C), on which this work focuses, was first identified in human fingers by Vater in 1741 [12,13] and was later described by Pacini, the receptor's namesake, in 1835 and 1840 [14,15]. Since then, the PC has been studied more than any of the other mechanoreceptors due to its large size (up to 3-4 mm in human skin [16]) and ease of identification during dissection [17]. The PC is the cutaneous mechanoreceptor responsible for the sensation of low-amplitude, high-frequency vibrations in the 20-1000 Hz range [18–22]. The PC has low spatial sensitivity across the surface of the skin, and the receptive field of a single PC may span an entire hand [2]. The

PC functions as a bandpass filter to vibrations, an effect attributed to its complex end organ [23,24]. For this reason, the structural and chemical properties of the end organ have been the subject of many experimental [25–27] and computational [10,23,24,28–33] studies.

PCs are distributed throughout the dermis and subcutaneous tissue of the fingers and palms of the human [17] and non-human [34] hand/forefoot, among other anatomical locations. The PC has an ellipsoidal shape with a typical long-axis length range of 1-4 mm in human digital PCs [16,17] and 1 mm for PCs from cat mesentery [35], with the short axis reported as approximately 66% of the long axis in the cat [35]. PC shape and size can vary depending on anatomical location within an individual [16,17], and PCs can also vary in size within a single section of skin or cluster (Figure 1.2).

1.2.1 PC inner structure

The inner structure of the PC is highly specialized to allow response to skin motion within its frequency sensitivity range. A central afferent sensory neuron (neurite) runs along the long-axis of the PC and is enclosed by an inner core, which is itself encapsulated by an outer core [36]. The inner core and outer core are separated by an intermediate growth zone that varies with age and contains cells that eventually become incorporated into the inner or outer core [36]. The outer core is enclosed by an external capsule [36]. The neurite and inner and outer cores are the three main structural regions of the PC and will be discussed in detail in the subsequent paragraphs.

1.2.1.1 Neurite

The PC’s neurite runs along the long axis of the receptor. The neurite is an Aβ fiber and is classified as a rapidly-adapting type II afferent based on the dynamics of its response to indentation. The neurite contains a node of Ranvier approximately 50 μm proximal to the neurite's point of entry into the PC capsule [35]. The neurite is myelinated outside of the capsule [35]. The neurite becomes narrower and loses its myelin sheath inside the capsule and ends in a small terminal bulb of approximately 8-12 μm diameter [35]. Receptor potentials [37] and action potentials [38] can be recorded on the neurite just outside of the PC capsule in response to vibration. Previous studies have also recorded potentials at the first node of Ranvier inside of the capsule [35,39], but many have debated whether or not the neurite can support action potentials. Identification of voltage-gated sodium channels on the neurite (and non-neural cells of the surrounding capsule) by Pawson et al. [40] confirms the ability of neurite to support action potentials [41] and also suggests that these voltage-gated channels may play a role in mechanotransduction.

In addition to voltage-gated channels, the PC neurite also contains nonvoltage-gated ion channels that are stretch-activated and selectively permeable to sodium [42]. These stretch-gated channels enable the central neurite to be the site of mechanotransduction within the PC. When the surface of the skin is deformed, this deformation propagates to the dermis, where it reaches the PC's external capsule. The deformation is then transmitted through capsule until it reaches and distorts the neurite. As a result, stretch-gated cation channels on the neurite membrane open, initiating a neural response [37].

Previous studies have used various types of microscopy to analyze cytoplasmic protrusions (filopodia) on the terminal portion of the neurite and have identified structural differences between the filopodia and the rest of the neurite [43–46]. These findings have led to the suggestion that different physiological processes may occur in the filopodia and that they may be the specific site of mechanotransduction on the neurite [43]. Filopodia are also located in other rapidly-adapting receptors, such as Meissner corpuscles and muscle spindles [18], further suggesting their importance in mechanotransduction. While it has been hypothesized [43] that filopodia are the sites of mechanoelectric conversion, it is unknown exactly how this process occurs. The presence of actin in filopodia draws a parallel to the stereocilia of inner ear hair cells [43,47] and supports the hypothesis that filopodia are mechanotransduction sites in the PC [27]. Experiments have also identified voltage-gated sodium channels [40] and an abundance of mitochondria [48] located on and at the base of filopodia, suggesting that this specific region of the neurite can support action potentials. Finally, their location within the PC, specifically with respect to the hemilamellae of the inner core, suggest that the neurite's filopodia may be ideally situated to detect mechanical deformations transmitted through the PC's capsule [46].

1.2.1.2 Inner core

The neurite is immediately surrounded by an inner core of tightly-packed, thin cytoplasmic lamellae [36]. The lamellae are bilaterally-arranged into symmetrical hemilamellae that surround the neurite [18,36,45]. The innermost lamellae and neurite are completely separated by connective tissue, and this tissue extends into the clefts between the two separated halves of the inner core [7,36]. Electron microscopy on PCs isolated from mature cat mesentery identified approximately 60 compact layers within the inner core [36]. The cells of the inner core are derived from Schwann cells [43,49] and may play a role in the PC's neural response to sustained mechanical pressure.

1.2.1.3 Outer core

The inner core is surrounded by the outer core, which makes up a large portion of the PC's capsule. The outer core is composed of concentrically-aligned lamellae, with approximately 30 layers present in the mature cat PC [36]. The lamellae contain multiple epithelial-type cells, with radially-increasing lamellar spacing [18]. These cells are extremely flattened, with thicknesses on the order of 200 nm [36]. Collagen fibrils are located on the outer surface of outer core lamellae, with collagen deposition increasing with PC age [36]. Each pair of adjacent layers is separated by a fluid-filled layer, which is prevented from flowing across lamellae by tight junctions between the lamellar cells and is therefore kept in successive layers [18,36,45]. The presence of these successive fluid layers contributes to the overall turgidity of the PC [45].

It has been suggested that the fluid-lamellar composition of the outer core, specifically the presence of the fluid layers, allows the outer core to function as a filter to vibratory stimuli [10,11,23,24,45]. Experimental removal of the outer core [11] caused the PC to behave as a slowly-adapting receptor as the recorded receptor potential in response to a sustained mechanical stimulus decayed in over 10x the amount of time required in an intact PC. In addition, the decapsulated PC only produced potentials in response to the onset, and not the offset, of a sustained mechanical stimulus. These results suggest that the capsule is essential to the coupling of the stimulus to the neurite and is therefore an integral mechanical component of the receptor's adaptation. The rapidly-adapting properties of the neurite supplying the PC, however, are not trivial and also contribute to the receptor's characteristic response [50]. Thus, the PC's outer core together with its rapidly-adapting neurite are responsible for the PC's role as a bandpass filter to vibrations [11,50].

1.2.2 Response to vibratory stimuli

Receptor potentials have been recorded from the PC's neurite [21,37], and it was found that these potentials increase with stimulus amplitude in a frequency-dependent manner [51]. Once the receptor potential reaches a threshold magnitude, an action potential is generated and propagates along the neurite [20,38]. The PC neurite exhibits a *response threshold*, which is the vibration amplitude at which the neurite begins to fire action potentials in response to the stimulus. As the vibration amplitude increases, the firing rate of the neurite also increases until it fires at the same rate as the vibration. At this amplitude, which is referred to as the *tuning threshold*, the neurite and stimulus phase-lock, and the PC fires one action potential per cycle [20]. In some electrophysiological recordings, the PC can fire action potentials at a rate of 2 spikes/cycle for high-amplitude vibrations [20]. The response and tuning thresholds are both frequency-dependent, and the resulting amplitude vs. frequency curves for each value shows a characteristic U-shape [20]. In a study performed on cat mesenteric PCs, the stimulus frequency at which peak sensitivity occurred was 270 Hz [20].

1.2.3 Response to sustained stimuli

In response to a sustained indentation, the PC fires action potentials at the onset and offset of the stimulus [50]. The PC only fires one or two action potentials in response to the onset of the pressure, which is attributed to the rapid (on the order of a few ms) decay of the receptor potential [52]. As mentioned previously, removal of the PC's capsule resulted in a slower receptor potential decay (~70 ms) in response to stimulus onset [11]. The decay of the receptor potential following the onset of a sustained pressure is attributed to both the mechanics of the capsule and the adaptation properties of the neurite [18]. The PC's firing during the onset of the stimulus depends on the strain rate and final strain of the ramp portion of the compression [50,53]. PCs do not fire spontaneously [18].

1.2.4 Anatomical location

The PC is found embedded deep within the skin and subcutaneous tissues [17,34,54–56] and in other anatomical regions such as ligaments [57–59], joint capsules [60–62], muscles [63,64], internal organs [25,36,65–67], in contact with periosteum of bones [34,54], and in the hypodermis [68]. The PC is notably found within the hand of humans and monkeys, localized to areas necessary for gripping and tool manipulation [34]. In the human hand, PCs are distributed throughout the fingers and palms and have been observed to occur in clusters close to digital nerves and blood vessels [17,69]. There are approximately 300 PCs in the adult human hand [17,69], and thousands of PCs have been reported in the fetal hand [70] suggesting that the number of PCs decreases with age. The density of PCs is typically reported to be higher in the fingers than in the palm of the human hand, as values between 44-66% of the total PCs in adult cadaveric hands were reported to be located within the fingers [17,70]. In both the human and monkey hands, PCs were predominantly found in the three central fingers of the hand [17,34]. The density of PCs, unlike that of other mechanoreceptors, does not vary considerably along the length of the finger [22]. This relatively uniform distribution, together with the large receptive field of PCs, suggest that the PC does not play a role in spatial discrimination of a stimulus [22].

The PC's location within the hand is of interest to hand surgeons, as PCs can be used to locate digital nerves during medical procedures [71,72]. Enlarged or aggregated PCs have also been implicated as the cause of pain or tenderness in the palm or fingers, especially when PC proliferation compresses the digital nerves [68,71,73]. PCs in the hand are also associated with Dupuytren's contracture, as histological studies have shown that PC size and number of lamellae increase with the disease [74].

1.2.5 Clustering

PCs are also often observed in clusters of multiple receptors (Figure 1.2), a phenomenon conserved across species. PC clusters have been identified in the human hand [17,75]; the monkey hand [34,55]; cat feet [46,54,76], ankle joint [77] and knee joint [61]; the rat ankle joint [49]; the elephant feet [78]; the raccoon forepaw [79]; and the interosseous region of the kangaroo leg [80]. The number of PCs found within a cluster varies between species, with clusters of 2-3 PCs in the human [81], 2-5 in the monkey [34,55], 3-4 on average in the elephant [78], and 2-11 in the cat [46,54,61,76,77].

1.2.6 Role in somatosensation

Mechanoreceptors are distinguished based on their response dynamics and the size of their receptor field, with the PC classified as a rapidly adapting type II receptor based on its sensitivity [2,8]. As stated previously, the PC is optimized to respond to high-frequency vibrations, while the other mechanoreceptors are optimized to other touch modalities (i.e. pressure, low-frequency vibrations) [2,18]. Traditionally, it was believed that touch modalities were segregated in the nervous system, as different afferent classes (rapidly vs. slowly adapting afferents) were responsible for the sensation of distinctly different mechanical stimuli from the periphery to the cortex [82]. More recently, however, the concept of segregation has been replaced with convergence. While each mechanoreceptor has its own optimal stimulus, multiple mechanoreceptors can be recruited in response to a single tactile stimulus [1,82]. Perceptions such as texture, object shape, and skin motion may receive input from multiple mechanoreceptor types.

Thus, while the PC is responsible for the sensation of high-frequency vibrations, it is also implicated in the detection of other naturally-occurring touch modalities. The perception of texture involves input from multiple mechanoreceptive afferents, and previous studies have shown that vibration is critical to texture perception [83]. Scanning a textured surface causes vibrations to propagate through the skin, which results in the spiking of PC afferents [84,85]. The PC is also important in slip detection. PC afferents fire spikes at the onset and offset of contact with an object [86] and can signal the occurrence of slip [87], making the receptors critical in object manipulation and grip control. PCs are also implicated in tool use, as they are responsible for the perception of vibrations transmitted through the object to the hand [70,88].

1.2.7 Implications in disease and aging

Previous structural studies [89] found that, with age, the human PC increases in size by the addition of lamellae until it eventually becomes distorted in structure, which is followed by a decrease in the number of PCs within the skin. While these anatomical and morphological changes in the receptor due to aging have been reported in the PC literature, the mechanical and functional responses of isolated aged PCs have not been probed. Previous studies have, however, investigated the vibration sensitivity changes that occur within the hand with age. Vibrotactile detection experiments by Verrillo [90] performed on subjects of various ages found that vibrotactile thresholds in the hand at higher frequencies (i.e., within the typical PC sensitivity range) increase with age. Verrillo proposed that the experimentally-observed increase in vibrotactile threshold may be due to a decrease in the number of PCs within the skin but added that the density of PCs could not explain this phenomenon alone. Verrillo therefore proposed that geometric changes, such as those reported by Cauna [89] (i.e., addition of lamellae, shape distortion) may be a mechanism for the decreased vibrotactile sensitivity in the Pacinian frequency range with age.

Vibrotactile sensitivity can also be affected by disease, such as diabetes. Peripheral neuropathy is a common complication of diabetes and can affect the sensation of vibration, among other sensory modalities and neural functions [91]. Diabetic skin biopsies [92] have shown denervation and neuronal structural changes, which can affect the cutaneous mechanoreceptors [93]. In diabetic monkeys, the PC capsule can undergo structural changes including irregular spacing between lamellae, thickening of outer lamellae, and a breakdown of inner lamellae, causing the capsule to appear deteriorated [94]. Functionally, PCs are shown to be implicated in diabetic neuropathy as vibrotactile thresholds increase in patients with diabetes [92,95,96]. Advanced glycation as a result of diabetes leads to many complications associated with the disease, as advanced glycation end products can induce cross-linking of proteins such as collagen and cause increased vascular stiffness [97–99]. The vasculature of the PC capsule [100] may be stiffened as a result of diabetes, or the adventitial tissue of the PC's end organ may also become stiff, as glycation has been shown to affect not only the stiffness of vascular tissue but also that of tissues such as cartilage [101], tendon [102], and other connective tissues (i.e., plantar tissue [103]).

1.3 Previous models of the PC and other mechanoreceptors

Because of its elegant structure and important role in the somatosensory system, the PC has been the subject of numerous theoretical modeling efforts over the years. Models have also been proposed to simulate the transduction of other cutaneous mechanoreceptors, and these models can complement and inform PC models. Broadly, PC models can be classified as *functional* or *mechanistic*. The functional approach, pioneered by Freeman and Johnson [104,105], emphasizes the relationship between the input stimulus and the neuronal output as a black-box process. Freeman and Johnson developed a simple receptor model [104,105] consisting of an electrical circuit to match neural data collected from slowly adapting (SA), rapidly adapting (RA), and Pacinian afferents in the macaque monkey hand in response to skin vibration. Their basic model contained 4 degrees of freedom, which were fit to the neural data from the three different mechanoreceptors (SA, RA, PC). Their analysis and model fitting focused on the temporal structure of the afferent discharge, including overall firing patterns and impulse phase [104], and the stimulus-response functions that relate neural discharge to vibratory amplitude at different frequencies [105]. The Freeman-Johnson model was later extended by Slavik and Bell [106], who introduced hyperexcitability and an absolute refractory period following each action potential to improve the model's fidelity to neural data. Further work by Bensmaïa [107], specifically to model the Meissner corpuscle, allowed the model to predict RA afferent response to arbitrary stimuli (including complex stimuli and non-repeating noise) in both psychophysical and physiological contexts. Grandori and Pedotti [108] employed a series of transfer functions to simulate the neurite receptor potential of a capsulated and decapsulated PC.

In contrast to the functional approach, the mechanistic approach, starting with the seminal work of Lowenstein and Skalak [23] and Holmes and Bell [28,29], emphasizes the underlying behavior of the PC as a physical entity rather than as a conceptual one. This approach has the advantage of being governed by physical laws (e.g., conservation of momentum or charge) and providing insight into *how* the PC functions, but it has the disadvantage of requiring much more information and not necessarily capturing the PC response as consistently as a functional model. Loewenstein and Skalak (LS) [23] proposed that fluid-lamellar interaction within the PC capsule causes the receptor to act as a high-pass filter to vibrations and developed a mechanical model of the PC outer core based on this hypothesis. The PC was modeled as a series of cylinders with a rigid core at the center. The cylinders were joined by parallel elastic and viscous connections between adjacent layers. Biswas et al. [32] extended the LS model, incorporating a viscous core and larger interlamellar spacing. Like LS, Biswas used concentric cylinders to approximate the structure of the PC, but they adjusted the radius and number of lamellae to model the effect of PC size, and used more realistic physical parameters. Additionally, Holmes and Bell [28] developed a mechanical model of the PC capsule that used a two-dimensional cross section as an approximation to the full capsule, modeled as thin orthotropic elastic shells separated by fluid layers. Holmes and Bell homogenized their model and obtained the hoop strain in the receptor membrane, which they later coupled to a receptor potential model [29] of stretch-activated channels. Güçlü et al. [109] compared static indentation experiments to ovoid and semi-infinite finite-element models of the PC, and both models produced similar results for the transmission of the displacement through the PC, suggesting that the ellipsoidal geometry is not the only factor responsible for the PC's mechanical response.

Some models exhibit both mechanistic and functional features, such as the current study and Lesniak and Gerling's [110] model of the mechanotransduction of a slowly adapting type I (SA-I) receptor. They used a finite-element mechanical model [111] of a cross section of fingertip skin to obtain the strain-energy density (SED) in the vicinity of a Merkle cell neurite complex. The SED was transformed into the receptor current within the SA-I via a sigmoidal function, bypassing the mechanics of the mechanoreceptor, and the receptor current was transformed into SA-I spiking via a leaky integrate-and-fire model. Thus, a mechanistic model for skin mechanics was combined with a functional model for neural dynamics. Mechanistic, functional, and hybrid models have all provided new insight into cutaneous mechanosensation and are necessary to simulate different aspects of this transduction process. In addition to the models designed to explain PC function on the receptor level, psychophysical studies have addressed the perceptual aspect of the Pacinian system. Studies by Bensmaïa et al. [112,113] have greatly informed us of the response of the Pacinian system and have found that both intensity and temporal components contribute to high-frequency discrimination of simple and complex stimuli.

1.4 Motivation and open questions

The PC has long intrigued biomechanicians, with seminal theoretical work done by Loewenstein and Skalak half a century ago [23]. More recently, the field of haptics and the emerging need for better haptic feedback systems [114] have inspired the development of computer models of how our peripheral nervous system, and specifically mechanoreceptors, encode vibrotactile stimuli. Models of the PC can provide insight into response properties necessary for the development of haptic devices, such as stimulus detection threshold and the distinguishability of different vibrotactile stimuli and locations. Due to the PC's importance in haptic sensing and the extensive literature available on the PC's structure and neural response, I aimed to investigate the mechano-to-neural transduction of the PC through a combination of mechanical and neural computational modeling and experiments.

Previous models of the PC discussed in Section 1.3 have address various aspects of the PC's response to mechanical stimuli. While these models have employed different approaches to investigate the relationship between the PC's properties, such as its ellipsoidal shape [109], lamellae [23,32], or location in the skin [30], these models have limitations (discussed in Section 1.3) and fail to unify all of the PC's anatomical components and response properties. In addition, in spite of the high degree of sophistication and creativity in PC models, the lack of complete data to specify the model parameters remains a considerable obstacle. To our knowledge, there has been no published study of PC mechanics that included an actual force or stress measurement and as a result, a wide range of values for the Young's modulus of the PC has been used in previous theoretical models.

The overarching goal of my thesis research was to unify the anatomical and electrophysiological observations of the PC via a detailed mechanistic model of PC response to mechanical stimulation, requiring a multiphysics, multiscale approach. My overall goal was to develop a comprehensive mechanistic model of both the mechanical and the neural response of the PC to stimulation while accounting for the three-dimensionality and detailed inner structure of the PC, the fine morphology and mechanosensitive channels of the neurite, and the receptor's *in vivo* location in the skin and within a cluster of multiple PCs. I also performed mechanical experiments on PCs isolated from human cadaveric hands to address the lack of mechanical data on PCs and characterize the apparent Young's modulus of PCs under steady-state experiments. Finally, I used my developed model to observe the differences in frequency sensitivity among PCs and their avian equivalent within different species.

The results of my thesis research are presented in the next six chapters. The next section lists a Summary of Accomplishments, which provides more detail about what will be discussed in the following chapters.

1.5 Summary of accomplishments

The key research studies of my thesis are organized as the following six chapters. The chapters are briefly outlined below.

Chapter 2: Multiscale mechanical model of the Pacinian corpuscle shows depth and anisotropy contribute to the receptor's characteristic response to indentation [115]. In this study, I used a multiscale finite-element mechanical model to simulate the equilibrium response of the PC to indentation. The key hypothesis of this study was that a layered, anisotropic structure, embedded deep within the skin, would produce the nonlinear strain transmission and low spatial sensitivity characteristic of the PC. I first modeled an isolated PC with fiber network aligned with the PC's surface to simulate the lamellar layers within the PC's outer core and compared the strain transmission through the PC with previously published experimental data. Next, I modeled a single PC embedded within the epidermis or dermis of the skin to simulate the receptive fields of PCs under indentation in each location.

Chapter 3: A multiphysics model of the Pacinian corpuscle [24]. I combined mechanical models of the PC with an electrochemical model of peripheral nerves to simulate the tactile response of the entire system. A three-stage model of response to a vibratory input was developed, consisting of (1) outer core mechanics, (2) inner core mechanics, and (3) neurite electrochemistry. Using this model, I was able to simulate the PC's band-pass filtration of vibratory stimuli and rapid adaptation to sustained mechanical stimuli. I was also able to simulate the effect of varying the number of lamellae within the PC outer core and model the resulting shift in frequency response.

Chapter 4: Computational parametric analysis of the mechanical response of structurally varying Pacinian corpuscles [33]. I sought to evaluate the relationship between the PC's material and geometric parameters and its response to vibration. I used the Stage 1 model of outer core mechanics developed in Chapter 3 and analyzed the effect of lamellar modulus, lamellar thickness, fluid viscosity, PC outer radius, and number of lamellae on the PC's frequency sensitivity. I combined all five structural parameters into dimensionless expressions for the relationship between the parameters and peak frequency or bandwidth.

Chapter 5: A finite-element model of mechanosensation by a Pacinian corpuscle cluster in human skin. I embedded the model developed in Chapter 3 in a skin mesh to simulate the mechanical and neural behavior of PCs in response to vibrations *in vivo*. I created a finite-element model of human skin containing two PCs to analyze the effect of skin and clustering on the PC's response to vibration. I analyzed the effects of separation distance between two PCs in a cluster and the location of these PCs with respect to the skin stimulus.

Chapter 6: Micropipette aspiration of the Pacinian corpuscle [116]. In the models created in Chapters 2-5, I used estimates of the PC's mechanical properties. In this study, I used micropipette aspiration (MPA) to determine an apparent Young's modulus for PCs isolated from a human cadaveric hand. The slope of the protrusion length vs. suction pressure plot resulting from MPA was used to calculate the apparent Young's modulus. Using 10 PCs, I calculated a Young's modulus of 1.40 ± 0.86 kPa, which is on the same order of magnitude as the Young's modulus used in previous models.

Chapter 7: An inter-species analysis of the Pacinian corpuscle's frequency sensitivity. I sought to compare the frequency sensitivity of PCs and Herbst corpuscles (HCs) from various species using my model discussed in Chapters 3-5. I first performed a thorough literature search to compile the structural parameters of PCs and HCs from various species based on the availability of histological images. I then used the equations for peak frequency and bandwidth derived in Chapter 4 to predict these frequency responses of each species.

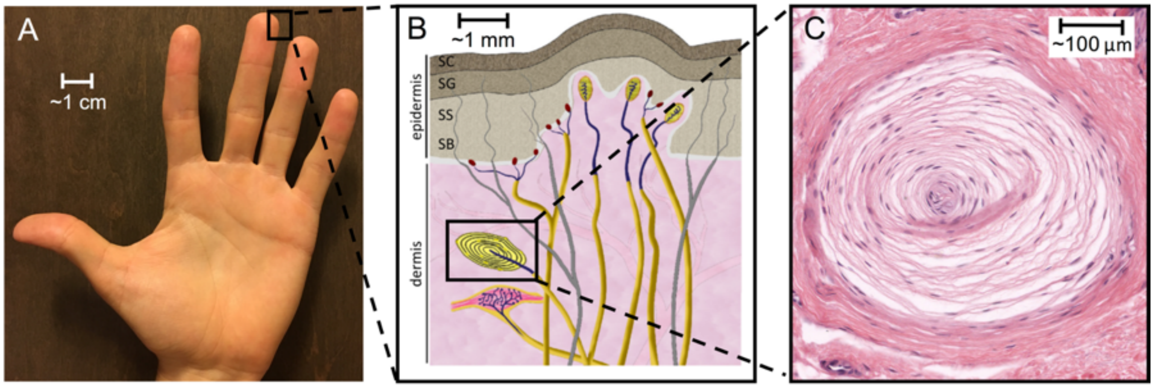

Figure 1.1: Schematic of human hand and mechanoreceptors. (A) Representative human hand, with scale bar on the centimeters scale. **(B)** The four types of mechanoreceptors in glabrous (non-hairy) skin with the PC shown in yellow and enclosed in the black box. Scale bar is on the millimeter scale. Image reprinted from Neuron, Vol. 79 Issue 4, Abraira VE and Ginty DD, The Sensory Neurons of Touch, pp. 618-639, 2013 with permission from Elsevier. **(C)** H&E staining of the cross section of a PC in a thick human skin slice. Scale bar is on the hundreds of microns scale. The image was provided by Dr. Christopher Honda from the University of Minnesota.

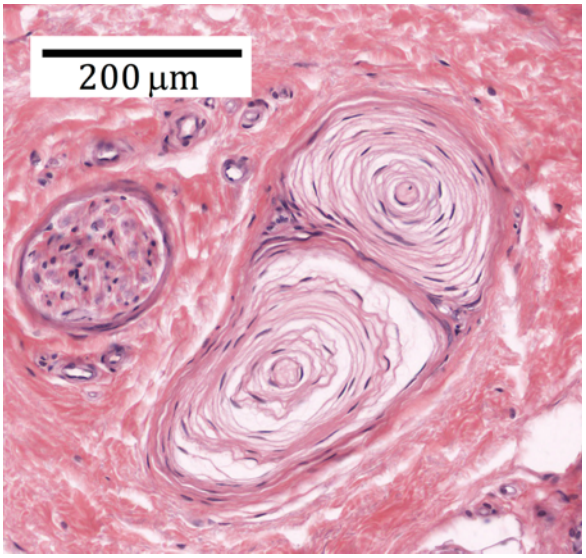

Figure 1.2: Cluster of two PCs in thick human skin slice. The scale bar corresponds to 200 microns. The image was obtained from the same sample of skin as Figure 1.1C after H&E staining and provided by Dr. Christopher Honda from the University of Minnesota.

CHAPTER 2: MULTISCALE MECHANICAL MODEL OF THE PACINIAN CORPUSCLE SHOWS DEPTH AND ANISOTRPHY CONTRIBUTE TO THE RECEPTOR'S CHARACTERISTIC RESPONSE TO INDENTATION

The content of this chapter was previously published as a research article in the journal *PLoS Computational Biology* by Quindlen, Lai, and Barocas [115].

2.1 Summary

This study focuses on how the PC's structural anisotropy and location in the skin contribute to its steady-state response. The PC is comprised of lamellae that surround the nerve fiber at its core. We hypothesized that a layered, anisotropic structure, embedded deep within the skin, would produce the nonlinear strain transmission and low spatial sensitivity characteristic of the PC. A multiscale finite-element model was used to model the equilibrium response of the PC to indentation. The first simulation considered an isolated PC with fiber networks aligned with the PC's surface. The PC was subjected to a 10 μm indentation by a 250 μm diameter indenter. The multiscale model captured the nonlinear strain transmission through the PC, predicting decreased compressive strain with proximity to the receptor's core, as seen experimentally by others. The second set of simulations considered a single PC embedded epidermally (shallow) or dermally (deep) to model the PC's location within the skin. The embedded models were subjected to 10 μm

indentations at a series of locations on the surface of the skin. Strain along the long axis of the PC was calculated after indentation to simulate stretch along the nerve fiber at the center of the PC. Receptive fields for the epidermis and dermis models were constructed by mapping the long-axis strain after indentation at each point on the surface of the skin mesh. The dermis model resulted in a larger receptive field, as the calculated strain showed less indenter location dependence than in the epidermis model.

2.2 Introduction

As mentioned in Section 1.2, the PC has low spatial sensitivity across the surface of the hand [2] and is located in the dermis of glabrous skin [1,109]. In addition, it has a ovoid shape (Figure 2.1) and a complex inner structure, which consists of an outer core containing 30 or more concentrically aligned collagenous lamellae [36]. The lamellae are believed to act collectively as a high-pass filter that shields the nerve fiber at the receptor center from low frequency, high amplitude stimuli [2,18,23]. The PC is a difficult organ to understand because its function involves a complex, interrelated set of biological, chemical, mechanical, and electrical phenomena. The overarching goal of this study was to address the fundamental mechanics of the PC and the role of its structure in determining how skin displacement is transmitted to the PC neurite.

The work of Güçlü *et al.*[109] was an important exploration of PC mechanics. The authors used finite-element modeling to investigate the role of the PC’s geometry in its mechanical response to static indentation. Experimental data in which PCs were indented by cylindrical contactors with step waveforms of various amplitudes were compared to the computational models. Semi-infinite plane and ovoid models produced similar displacements within the PC in response to static indentation, and neither model matched the localization of strain near the contractor seen in the experiment.

The purpose of this study was to test two specific hypotheses about the biomechanics of the PC. First, Güçlü *et al.* rejected the hypothesis that receptor *shape* leads to the observed mechanical behavior of the PC, leaving open the question of how the strain concentrates near the indentation site; herein, we tested the hypothesis that *mechanical anisotropy* contributes to the strain localization. Second, having concluded that a structural model of the PC is mechanically acceptable, we used that model to test the hypothesis that *deep embedding* within the skin contributes to the low spatial sensitivity and large receptive field of the PC.

2.3 Methods

2.3.1 Multiscale model

A multiscale scheme [117–119] was used to model the response of the PC to indentation. The method is summarized here and described in detail elsewhere [117–119]. A finite-element model at the macroscopic level was coupled with representative volume elements (RVE), each comprised of a fiber network, at the microscopic scale (Figure 2.2). Each finite element contained eight Gauss points, each with an associated RVE. Each RVE contained a network of 500-700 fibers in a constrained mixture (cf. [120,121]) with a nearly incompressible neo-Hookean matrix. In this study, each element received a unique set of fiber networks depending upon its location within the mesh.

Macroscopic-level deformations were passed down to the microscopic level, the networks within each RVE were thus stretched, and the force exerted by each fiber, F, was calculated using the fiber constitutive equation

$$F = \frac{A}{B}(\exp(BE_f) - 1) \tag{2.1}$$

where A is a measure of fiber stiffness, B is a measure of fiber nonlinearity, and E_f is the fiber Green strain computed from the fiber stretch, λ_f,

$$E_f = 0.5(\lambda_f^2 - 1) \tag{2.2}$$

From the fiber forces on the RVE boundaries, the volume-averaged Cauchy stress at each Gauss point within the macroscopic element was calculated as

$$S_{ij}^{macro} = \frac{1}{V}\int_V S_{ij}^{micro}\, dV = \sum_{bc} x_i F_j \tag{2.3}$$

where V is the RVE volume, S_{ij}^{micro} is the microscale stress, bc refers to summation over all network nodes on the RVE boundary, x_i is the boundary fiber cross-link i-coordinate, and F_j is the force acting on the boundary fiber cross-link by the fiber in the j-direction. The averaged stress balance was given as [118]

$$S_{ij,i} = \frac{1}{V}\oint_{dV} (S_{ij}^{micro} - S_{ij}^{macro}) u_{k,i} n_k \, dS \tag{2.4}$$

where u_k is the RVE boundary displacement and n_k is the normal vector to the RVE boundary. The displacements were updated until the stress balance (2.4) had equilibrated. Simulations were run on 64 cores at the Minnesota Supercomputing Institute.

2.3.2 Mesh generation

All finite-element meshes were generated in ABAQUS. A mesh convergence study on the isolated PC problem gave average errors of 5% in nodal displacement between the coarsest mesh and the finest mesh (which was used in the study). Based on this result and our previous studies [117], we expect our numerical results to have errors of at most 5%.

2.3.3 Microstructural model specifications

Delaunay networks were created to populate the RVEs within the multiscale model. To capture the anisotropy of the collagenous lamellae within the PC, the networks for each finite element were aligned with the PC's surface (Figure 2.3A). In the embedded models, the networks populating skin elements were made transverse orthotropic and aligned with the surface of the skin to reflect dermal collagen organization [122].

Material constants *A* and *B* for equation (2.2) were set at 114 μN and 10 respectively, obtained from fitting the multiscale model to data from a published study on dermal mechanics [123]. The Poisson's ratio for the neo-Hookean matrix was set at $\nu = 0.47$ for the simulations to model a nearly-incompressible matrix. The matrix shear modulus was set at $G = 4.2$ kPa [117]. The properties of the Pacinian corpuscle lamellae are not known, and estimates of the modulus of the lamellar layers have ranged from 1 KPa [124] to 0.5 MPa [23]. Neither of those bounds was based on a published mechanical measurement of the properties of collagen fibers within the PC; the small value was estimated based on assumed high compliance of the basement membrane, and is consistent with an anecdotal reference from the literature ([125] cited by [18]), and the latter was based on arterial wall. Recent work [124] has found that using a low modulus for the lamellar stiffness gives more accurate predictions of PC response in the high-frequency range, but collagen fibers have moduli in the MPa range [126], as have basement membranes from the renal tubule [127] and ocular lens [128–130]. It is thus clear that a better theoretical and structural description is needed, and it is likely that the choice of modulus will depend on the structure of that model. Since the emphasis of this work was on the effect of anisotropy, not on differences in stiffness between the corpuscle and the surrounding skin (which could be a very important factor and which should be explored in future studies), we chose to give the fibers in our PC model the same properties in as the fibers in the skin.

2.3.4 Macroscale model specifications: Isolated corpuscle

The isolated Pacinian corpuscle was meshed as a half-ellipsoid, with a major axis of length 1 mm and a minor axis of length 0.5 mm. The PC model contained 2984 hexagonal elements. The isolated PC model was subjected to 10 μm indentation by a 250 μm diameter indenter to simulate the experiments performed by Güçlü *et al.* and the associated finite-element model [109]. The indenter displaced nodes vertically, as shown in Figure 2.3A.

For consistency with the Güçlü experiments, the nodal displacements in the isolated PC model were analyzed. The displacement of nodes located along the top 100 μm of the z-axis was calculated after 10 μm indentation. Strain (ε_{yy}) along the long axis of the PC was calculated for comparison to the embedded model.

2.3.5 Macroscale model specifications: Embedded corpuscle

2.3.5.1 Model Preparation

A tissue-embedded PC was meshed as an ellipsoid with a major axis of 1 mm and a minor axis of 0.5 mm inside of a rectangular prism (Figure 2.3B). For the epidermis model, the domain was 1.5 mm x 1.5 mm x 0.75 mm, with the center of the PC located 0.375 mm beneath the surface. For the dermis model, the domain was 1.5 mm x 1.5 mm x 2.75 mm, with the center of the PC located 2.375 mm beneath the surface. The epidermis and dermis models had 2928 and 4380 hexahedral elements, respectively. The long axis of the PC was parallel to the surface of the skin.

The embedded PC models were subjected to 10 μm indentations at the surface of the skin. Nodes on the surface of the skin were indented individually in different simulations to construct the receptive field of the PC.

To observe the effect of PC orientation with respect to the skin surface, a dermally-embedded PC was modeled with its long axis perpendicular to the skin surface. This vertical PC model was subjected to 10 μm indentations at the skin surface.

2.3.5.2 Prediction of axial stretch on the PC

When the PC is mechanically stimulated, a receptor potential is produced and increases until a threshold is reached, and an action potential is initiated [18,20,21]. This study used the working model that stretch along the long axis of the receptor, and thus along the nerve fiber at the center of the PC, causes stretch-gated Na^+ channels along the axon to open and initiates the response of the PC [131].

Since the deformations involved are very small, the response of the PC to indentation for the embedded models was determined by calculating the linear strain along the long axis (y-axis) of the PC to simulate stretching of the axon,

$$\varepsilon_{yy} = \frac{l_y - l_{yo}}{l_{yo}} \tag{5.5}$$

where l_y is the length of the PC along the y-axis after 10 μm indentation and l_{yo} is the initial length of the PC along the y-axis. Length was calculated as the distance between the y-coordinates of two nodes located at the interface of PC and skin elements on the y-axis of the PC. In the case of the vertically-aligned dermally-embedded PC, the linear strain along the long axis (5.5) was measured with respect to the z-axis.

2.4 Results

2.4.1 Isolated corpuscle

The isolated PC was subjected to a 10 μm indentation with an indenter of diameter 250 μm to mimic the experiment and simulation of Güçlü *et al.* The multiscale model captured the nonlinear trend in displacement seen in the experimental data and not predicted by an isotropic linear elastic model (Figure 2.4A). The multiscale model populated with isotropic Delaunay networks rather than circumferentially-aligned networks also produced results similar to Güçlü *et al.*'s isotropic linear elastic model (data not shown). Figure 2.4B shows the displacement of nodes along a cross section through the x-z plane of the PC at y=0. As seen in Figure 2.4B, the multiscale model predicted a nonlinear spacing between nodes, with a greater nodal gap occurring with increasing depth.

The Von Mises stress was calculated at each element in the PC after 10 μm indentation for the cases of isotropic networks and circumferentially-aligned networks. In Figure 2.5, the isotropic case shows stress of approximately 2x higher magnitude around the indenter than those shown for the circumferentially-aligned case.

The strain along the long axis of the PC was calculated over 25 steps of 1 μm indentation. As seen in Figure 2.6, the strain along the long axis of the axon increased with indentation into the PC. The strain calculated for the isotropic network case was approximately 10x higher than that calculated for the circumferentially-aligned network case.

2.4.2 Embedded corpuscle

The long-axis strain along the PC resulting from indentation at various nodes along the surface was also compared for the epidermis and dermis models (Figure 2.7). The epidermal PC model showed large strain in response to loading directly above the PC that dropped off quickly as the indenter moved away from the PC. This drop-off implies more spatial sensitivity and thus a smaller receptive field. The dermal PC model shows less indenter position dependence and thus a larger receptive field.

The Von Mises strain was calculated within every element in the dermal- and epidermal-embedded cases after 10 μm indentation for indentations above the center of the PC and 750 μm down its long and short axes. As seen in Figure 2.8, the Von Mises strain in the PC in the dermis case shows little variation when the structure is indented at different locations. In both cases, PC strain is less than that of the immediately surrounding tissue because of its greater degree of anisotropy. The strain in the PC in the epidermis case shows greater variations with indenter location.

The long-axis strain along the PC resulting from 10 μm indentation at various nodes along the surface of the skin was compared for horizontally-aligned and vertically-aligned PCs embedded within a dermal mesh (Figure 2.9). The horizontal PC model showed positive strains or no strain resulting from indentation. The vertical PC model always showed negative strains in response to indentation. This result shows that indentation within the receptive field of a horizontally-aligned PC always results in positive axial stretch of the neurite. Indentation of the vertical model does not result in neurite stretch.

2.5 Discussion

This study used a multiscale finite-element model to determine that the structure of the PC is an important contributor to the nonlinear behavior of the receptor. In addition, it showed that the deep dermal location of the PC provides it with lower spatial sensitivity.

Several factors must be considered when interpreting our results. First, the mechanical stimulus was a fixed indentation into the PC with no transient effects. As such, this study addresses the location and magnitude of the stimulus but it does not take stimulus frequency into account when determining the PC mechanical response, as others have [23]. A static model was chosen as suitable for comparison with experiment [109], but it would not be appropriate for simulating the vibrotactile response. While Hubbard [10] also investigated PC mechanics, the results from the current paper cannot be directly compared to that study, which placed the PC within a hinged apparatus rather than stimulating with a vertical indenter. Therefore, the experiments performed by Güçlü *et al*. were used to validate the current model. Second, the PC was treated as incompressible, and no fluid movement was allowed within the PC even though such flow is known to be important [23]; thus, our model must be interpreted as the instantaneous response of the PC. The time-dependent response of the PC is necessary to address, as it is crucial to the PC's role as a high-pass filter to vibration [21,23], so insights from the current study should center on instantaneous response. Also, the experimental PC literature [20,21,51] focuses appropriately on the use of directly applied sinusoidal displacements to elicit the response of the PC to vibratory stimuli, providing a rich data set on the dynamical response of the PC. A model of PC mechanics should include a dynamical component (fluid flow, viscoelasticity, or both) to account for the phase difference that can occur between skin and PC stimulation, and also between PC stimulation and receptor response.

The mechanical model used in this study also simplified the structure of the PC to account only for anisotropy within the receptor and not for its specific components and detailed structure. The receptor capsule is composed of concentrically-arranged collagenous lamellae through which mechanical forces are transduced. The lamellae consist of condensed cell layers separated by layers of pressurized fluid [28]. The structure of the capsule is believed to play an important role in determining which mechanical forces are transmitted to the axon [39]. Each lamella contains a single layer of flat squamous epithelial type cells, with interlamellar spacing increasing with distance from the inner core [18]. Tight junctions between cells within each lamella prevent fluid flow across lamellae, but flow within the fluid layer between adjacent lamellae is possible and is significant at low frequencies. Loewenstein and Skalak first proposed that the role of the PC capsule's lamellar structure is that of a series of mechanical high-pass filters to shield the nerve fiber at the center of the receptor from low frequency, high amplitude stimuli [23]. To place this model in the broader context, it is more advanced than that of Güçlü, which is isotropic and linear elastic, but does not provide the single-lamellar-level description of Lowenstein and Skalak or of subsequent variations thereon [30,124]. The multi-scale approach of the current model, in which RVE's are introduced with position-dependent fiber orientations, could be extended to more complex microstructures as greater structural information becomes available. It is also notable that the lamella-based models [23,30,124] can account for the apparent viscoelasticity of the tissue by incorporating interlamellar flow; our model would not be able to do so but could incorporate a continuous viscous contribution similar to that derived previously [28] in a homogenized model of the PC. Clearly, there is need for a more detailed microstructural model that can address other aspects of PC behavior and perhaps can resolve the disconnect between the high stiffness typical of collagenous tissues and the low stiffness reported experimentally [125] and used to describe vibrotactile mechanics of the PC [124].

The mechanical model presented in this study simplified the neurophysiology of the PC action potential generation into axial stretch of its central nerve fiber. The solid black line in Figure 2.7 indicates the division between the positive and negative stretch. Because the exact mechanism of axon excitation is unknown, it is possible that the neurite could also be stimulated during compression along the long axis. Long-axis compression could, for example, be experienced as positive stretch in other directions due to neurite incompressibility. Thus, while it is possible that long-axis compression could lead to axon excitation, only long-axis stretch was considered in this study. It was initially proposed by Gray & Ritchie [131] that sensory receptors respond to mechanical stimulation resulting from nerve stretch. After PC compression studies performed by Hubbard in 1958 were unable to measure a change in axon length within the error of measurement, other possible mechanical mechanisms for transduction were proposed [10]. Specifically, Hubbard proposed that a change in the ratio between the major and minor axes of the cross section of the nerve fiber leads to a change in surface area and thus membrane stretch. Figure 2.10 shows a comparison between the model of axon stretch along the long axis used in this study and the area change proposed by Hubbard. Both long-axis strain and area strain increase monotonically with indentation into the PC. The area change of the PC is approximately six times the long-axis strain after 25 μm of indentation.

The orientation of the PC with respect to the surface of the skin was analyzed in this study. The results presented in Figure 2.9 show that indentation within the receptive field of a horizontally-aligned PC always results in either axial stretch of the neurite or no neurite stretch. Indentation within the receptive field of a vertically-aligned PC always results in neurite compression. The assumption used in this study that PC action potential generation is the result of axial stretch of the neurite and not axial compression means that the vertically-aligned PC was never activated by static compression. This study only shows the results of two PC orientations to static compression. A vibratory stimulus would involve both application and removal of an indenter due to oscillations, creating a more complex field that would likely include long-axis stretch in both cases. Thus, it is expected that different results on PC orientation would be obtained from models of vibration. It has previously been shown [132] that the electrophysiological response of an intact PC or its decapsulated nerve terminal changes polarity as it is rotated 90 degrees along its long axis. The same study also showed that a decapsulated terminal reversed the polarity of its neural response when compressed horizontally to the nerve or vertically to the nerve and proposed that the bilateral arrangement of cells around the terminal is responsible for changing how compression is transmitted to the neurite in these different orientations. It has also been shown [133] that compression of an intact PC along its long axis requires a much stronger stimulus to cause depolarization than that required in compression along the short axis. The current study models the transmission of mechanical stimuli through the lamellae to the neurite, and showed differences with PC orientation, but does not address the electrophysiological effects reported by others [132,133]. A combined model (cf. [28,134]) could lend greater insight into the interaction between mechanical and electrophysiological events.

Incorporation of isotropic Delaunay networks into the PC multiscale model rather than circumferentially-aligned networks (data not shown) resulted in a lack of shape dependence similar to that observed in Güçlü's finite-element study [109]. The current study thus confirms the finding that the ellipsoidal shape of the PC is not per se responsible for the observed mechanical behavior. In addition, the use of isotropic Delaunay networks further confirmed Güçlü‘s result that a homogeneous isotropic model of the PC cannot predict the experimentally observed displacement pattern in response to indentation. This study showed that the internal anisotropic structure is an important factor leading to the nonlinear displacements through the PC. The nonlinear reduction in displacement of lamellae located closer to the central core is in agreement with the hypothesis that the lamellar structure can help protect the nerve from large deformations under large skin surface loads.

The current model bases the mechanical properties of the networks representing the skin on data from uniaxial mechanical tests on dermis [123]. There are many factors that can influence the mechanics of skin, which can vary with anatomical location, proximity to blood vessels, thickness, body weight, hair-cycle stage, skin disease, and experimental conditions such as humidity [135–138]. Specifically, mechanical and structural properties such as viscoelasticity and anisotropy of skin can vary with age and anatomical location [138]. The mechanical properties of a skin sample are influenced by structural components such as the collageneous fiber network and the presence of different layers, which exhibit different mechanical properties, within the skin [30,136,137,139]. Selecting different data for fitting of the skin element mechanical properties used in this study would likely change the quantitative results of the current study due to differences in the aforementioned factors. The overall qualitative results of this study, however, are not expected to change. The mechanics of skin can also vary depending on the type of load applied, as skin behaves differently under compression and tension [135,136]. In vivo skin can also be in different amounts of tension depending on anatomical location, the body position, and the individual

[138]. All of the aforementioned factors could be considered in future models, with the current model functioning as a basis for subsequent studies and as a low-order model of skin behavior.

Past experiments have shown that the isolated PC is a highly sensitive mechanoreceptor with nanometer sensitivity [2]. The simulations performed in this study model the sensitivity of an isolated and embedded PC to micrometer-scale indentations. Sensitivity thresholds of the PC have been reported previously as 3 nm applied directly to the PC and 10 nm applied to the surface of the skin [2]. In the current study, the smallest indentation tested on the isolated PC was 1 μm, which corresponds to an amplitude of approximately 7 μm applied to the skin after comparison of the strain along the long axis of the PC in the isolated and dermis-embedded models. This ratio could change for a more anatomically detailed model, in which multiple receptors rather than just one are located within the dermis. There are currently no published data on the mechanics on a PC embedded in skin.

While this work focused on the PC, its results can also provide insight into other cutaneous mechanoreceptors. The embedded PC simulations showed that a PC located in the dermis of the skin was able to replicate the low spatial sensitivity of a PC *in vivo*. The PC embedded in the epidermis had a higher spatial sensitivity within the receptive field tested in the simulations. Receptors located closer to the surface of the skin, such as the Meissner corpuscle and Merkel cell-neurite complex, show decreased receptive fields and thus increased spatial sensitivity to mechanical events on the skin surface [140]. The current study could also be expanded to include the different geometries and cutaneous locations of other mechanoreceptors.

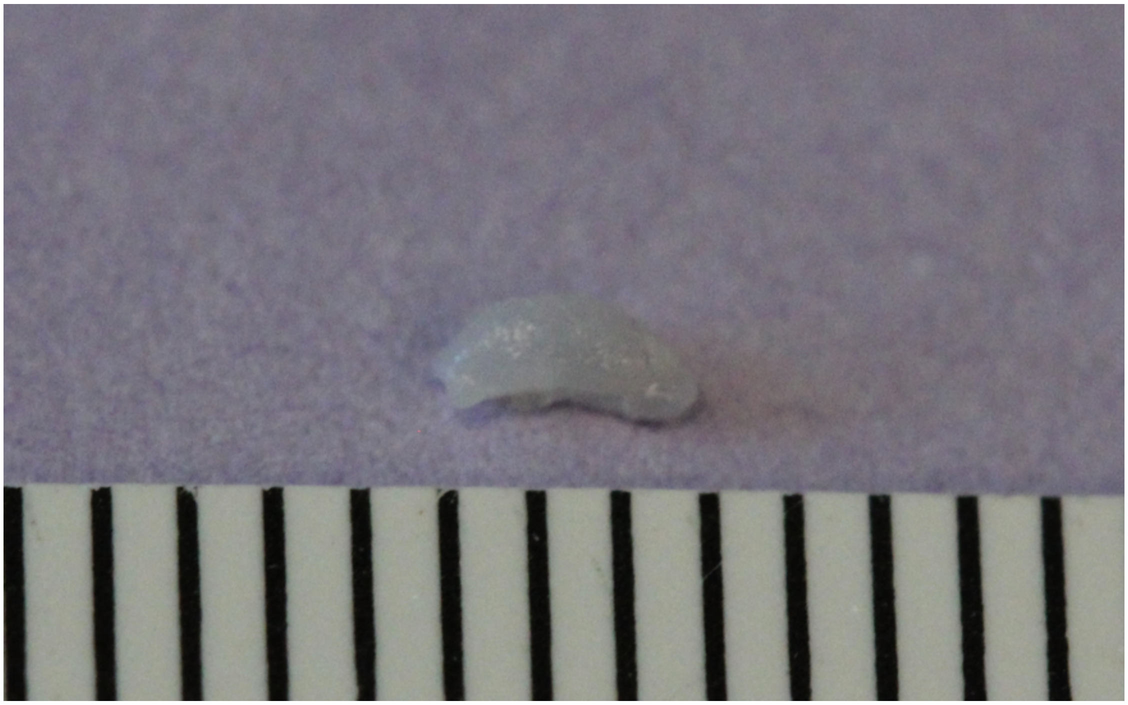

Figure 2.1: Excised PC. PC removed from a human cadaveric hand. Tick marks on the ruler correspond to 0.5 mm. Sample was obtained from cadaveric tissue provided, with approval, by the University of Minnesota Anatomy Bequest Program.

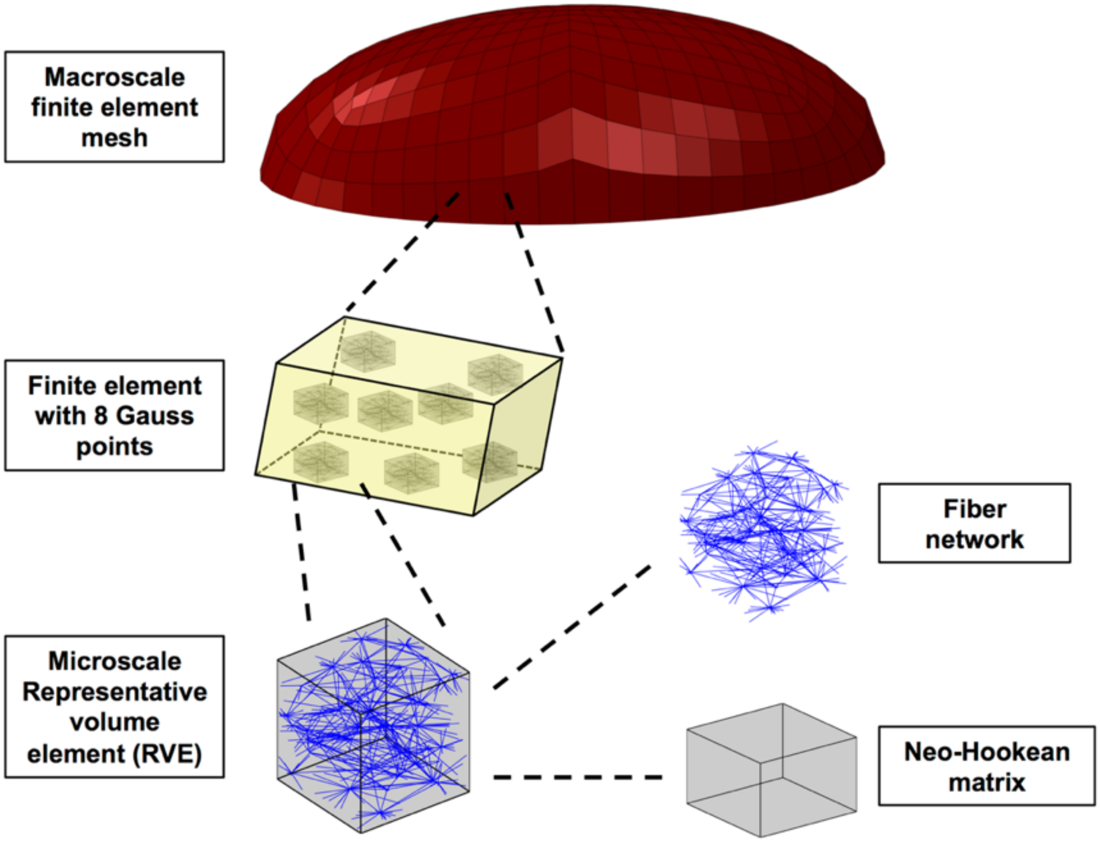

Figure 2.2: Multiscale model diagram. The multiscale model of the PC includes a macroscale finite-element mesh with representative volume elements (RVEs) of microscale fiber networks and neo-Hookean matrix.

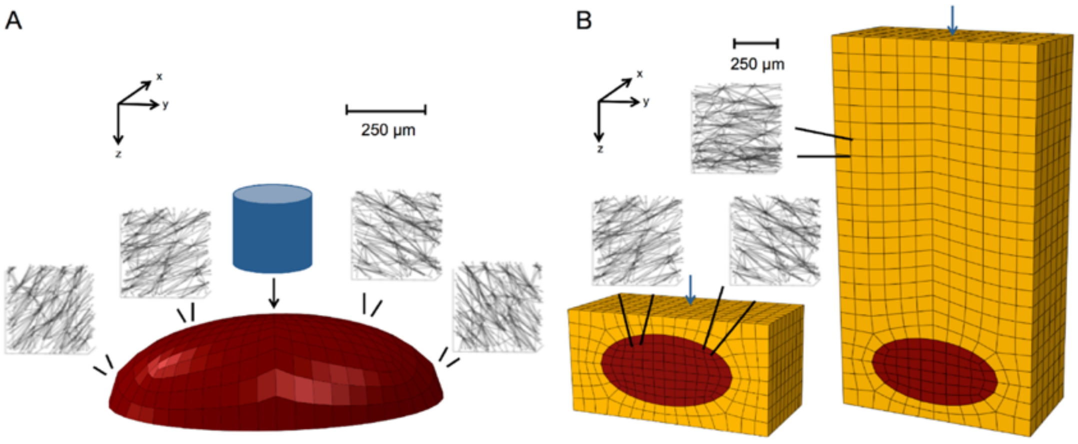

Figure 2.3: Finite-element meshes and representative networks. (A) The isolated PC model was populated with circumferentially-aligned Delaunay networks and indented with an indenter of diameter 250μm. **(B)** The epidermis and dermis PC models were populated with circumferentially-aligned Delaunay networks in the PC elements (red) and transversely isotropic Delaunay networks in the skin elements (gold). Single nodes on the surface of the meshes were indented.

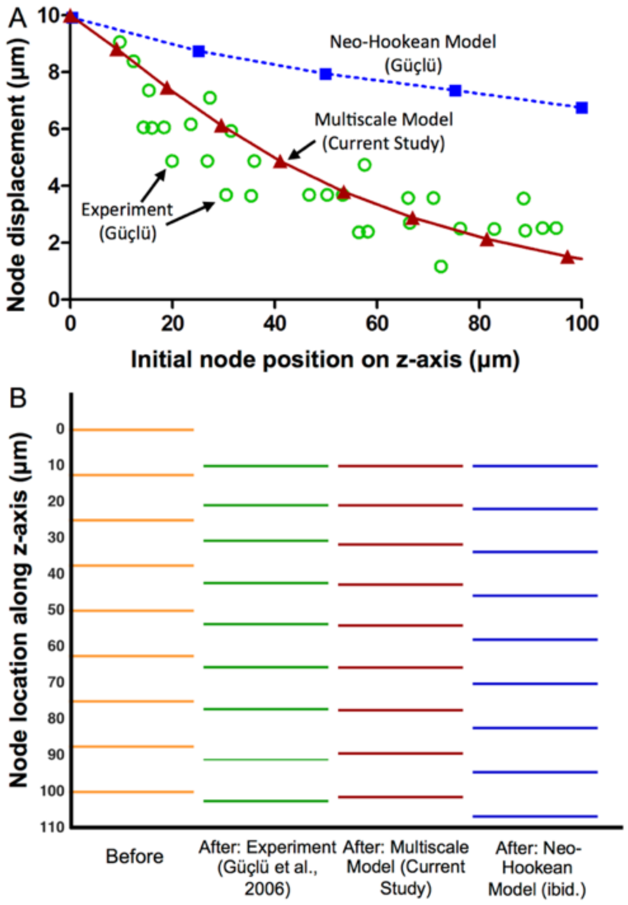

Figure 2.4: Comparison between model and experiments [7]. (A) Rapid, nonlinear drop in displacement with distance from the indenter site observed experimentally (green circles, from Güçlü) is matched by the current model (red triangles, solid line) but not by a linear elastic model (blue squares, dotted line; from Güçlü). **(B)** To visualize the nonlinearity, lines were drawn to represent the initial (first column) and final (second column) of the nodes in the indentation experiment. The multiscale model (third column) matched the experimental data much better than the linear elastic model (fourth column). These results confirm Güçlü's observation that a linear elastic model cannot capture the response of the PC and demonstrate the ability of a structurally-motivated anisotropic model to do so.

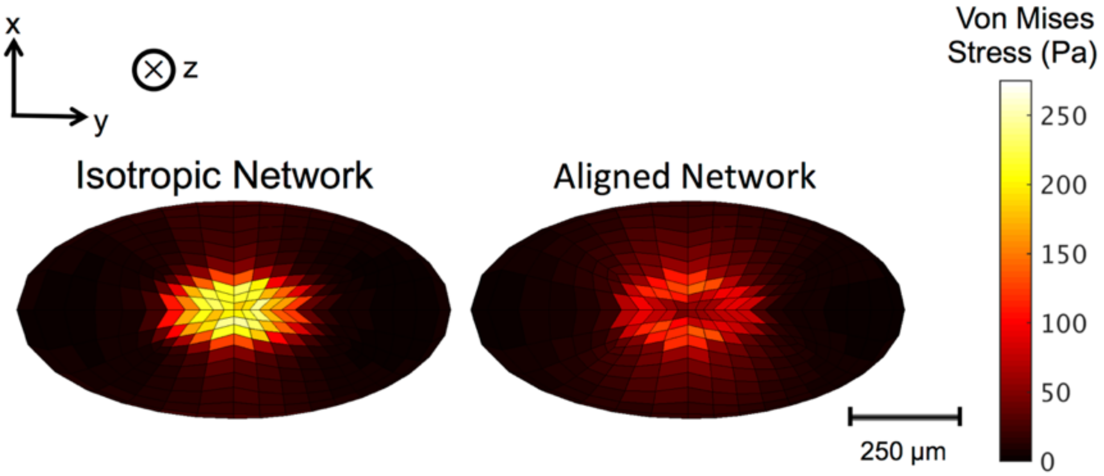

Figure 2.5: Von Mises stress in isotropic and aligned network cases. Von Mises stress along the top (surface layer) of the PC after 10 µm indentations (in the +z direction) with a 250µm diameter indenter for simulations run with isotropic networks (left) or circumferentially-aligned networks (right). The isotropic network case shows higher stress around the indenter than that shown in the aligned network case.

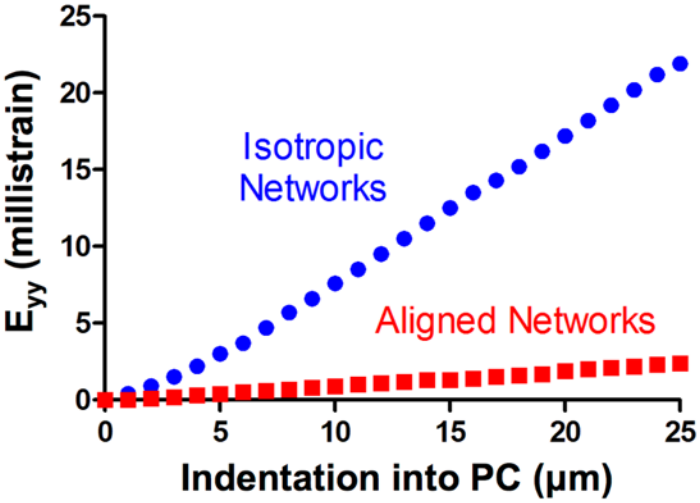

Figure 2.6: Long-axis strain in isotropic and aligned network cases. The strain along the long axis of the PC was calculated after 25 steps of 1 μm indentation. The cases of circumferentially-aligned (red squares) network and isotropic (blue circles) networks are shown. While the long-axis strain increases monotonically with indentation into the PC in both network cases, the isotropic network case showed higher strain than the aligned network case.

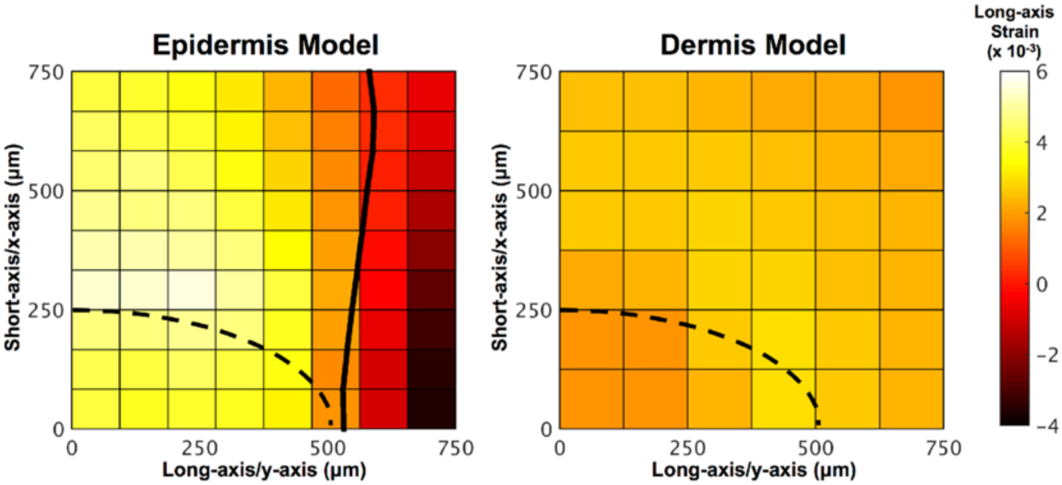

Figure 2.7: PC long-axis strain resulting from surface indentation at various nodes. Surface indentation sensitivity plot showing the long-axis strain along the PC resulting from 10 μm indentation at various nodes along the surface of the epidermis (left) and dermis (right) models. The dotted black line indicates the position of a quarter of the PC beneath the surface of the skin. The solid black line on the epidermis plot indicates the contour line for zero strain, which is the strain value below which the neurite would not be expected to respond to indentation.

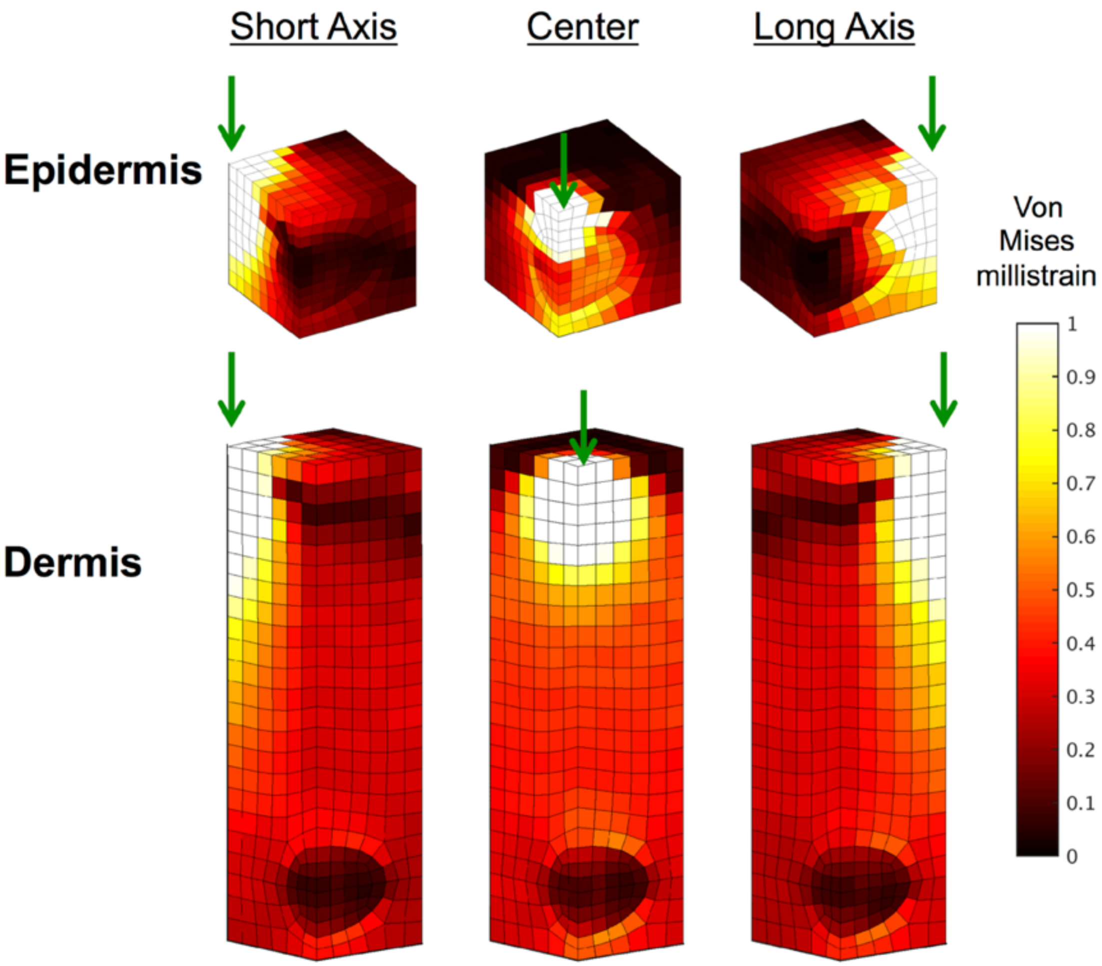

Figure 2.8: Von Mises strain resulting from surface indentation at different locations. The Von Mises strain (millistrain) at each element in the epidermis (top) and dermis (bottom) cases calculated after 10 µm indentation at three different locations on the surface (750 µm down the short axis of the PC, directly above the center of the PC, 750 µm down the long axis of the PC). The green arrows indicate the location of indentation. The large-strain region around the indenter reaches the epidermally-located PC but does not penetrate to the depth of the dermally-located PC. Only one quarter of the embedded PC mesh is shown due to symmetry.

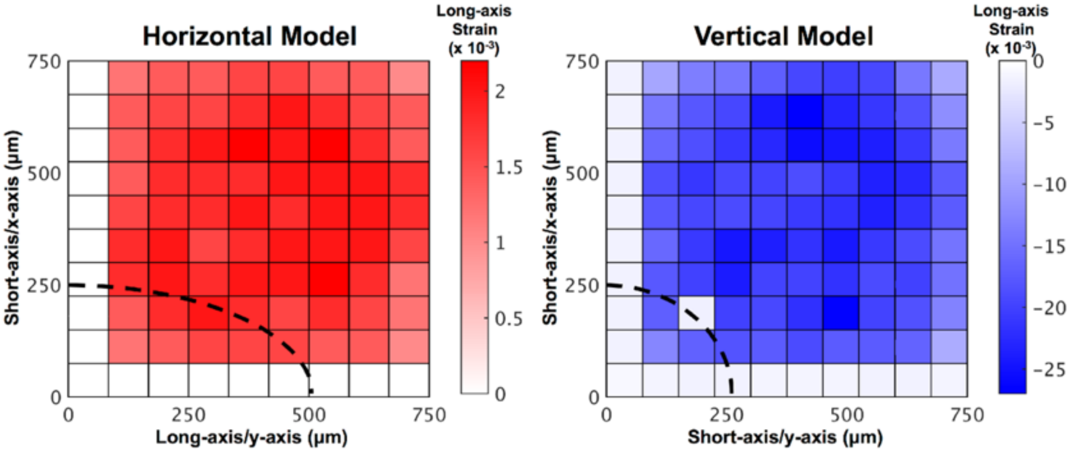

Figure 2.9: PC long-axis strain for horizontal and vertical PC alignment in skin mesh. Surface indentation sensitivity plot showing the long-axis strain along the PC resulting from 10 μm indentation at various nodes along the surface of the skin in a PC oriented with its long axis parallel to the surface of the skin (left, Horizontal) and its long axis perpendicular to the surface of the skin (right, Vertical). Both models contain a dermally-embedded PC. The dotted black line indicates the position of a quarter of the PC beneath the surface of the skin. The scale bars indicate the long-axis strain values for each model.

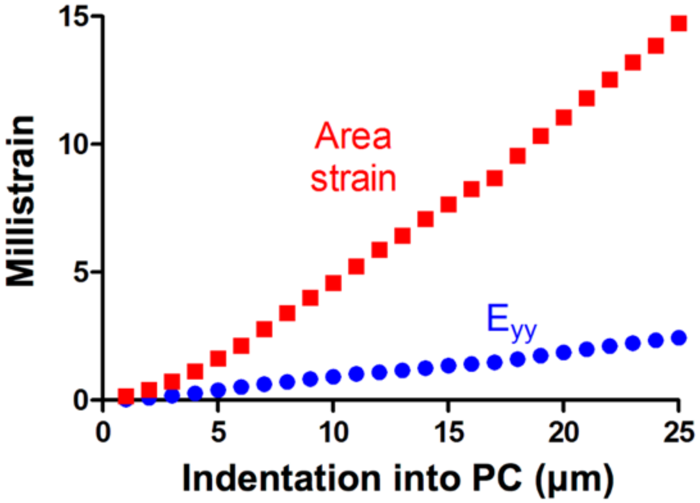

Figure 2.10: Comparison between long-axis strain and area strain. The long-axis strain of the PC (blue circles) and the area strain of the PC (red squares) were calculated for 25 steps of 1 μm indentation. Both long-axis strain and area change increase monotonically as the PC is indented.

CHAPTER 3: A MULTIPHYSICS MODEL OF THE PACINIAN CORPUSCLE

The content of this chapter was previously published as a research article in the journal *Integrative Biology* by Quindlen, Stolarski, Johnson, and Barocas [24].

3.1 Summary

This work combines mechanical models of the PC with an electrochemical model of peripheral nerves to simulate the tactile response of the entire system. A three-stage model of response to a vibratory input was developed, consisting of (1) outer core mechanics, (2) inner core mechanics, and (3) neurite electrochemistry. The model correctly predicts the band-pass nature of the PC's frequency response, showing that the PC structure can amplify oscillatory strains within its target frequency band. Specifically, strain induced by a vibratory stimulus is amplified by a factor of 8-12 from the PC surface to the neurite. Our results also support the hypothesis that PC rapid adaptation is affected by the lamellar structures without requiring neuronal adaptivity. Simulated different-sized PCs showed a shift in frequency response, suggesting that clusters of different-sized PCs could enable more nuanced tactile encoding than uniform clusters. By modeling the PC's mechano-to-neural transduction, we can begin to characterize the mechanosensation of other receptors to understand how multiple receptors interact to create our sensation of touch.

3.2 Introduction

The specialization of cutaneous mechanoreceptors to different mechanical stimuli is partially due to the morphology of the adventitial tissue that surrounds the afferent nerve fiber [2]. Specifically, the inner structure of the PC (Section 1.2.1) is highly specialized to allow response to skin motion within its frequency sensitivity range (20-1000 Hz [2,20,21]). For example, the outermost structural zone of the PC – the outer core – contains approximately 30 concentrically-arranged collagenous lamellae [36] that contain flat epithelial-type cells [18]. Each pair of adjacent layers is separated by a fluid-filled layer, which is prevented from flowing across lamellae layers by tight junctions between the lamellar cells [18,36]. This fluid has long been hypothesized to contribute to filtering of vibratory stimuli between the outer core and neurite [23]. The central neurite is the site of mechanical-to-neural transduction within the PC. In response to mechanical deformation, stretch-gated cation channels on the neurite membrane open, initiating a neural response [131]. It has been proposed that both voltage-gated and nonvoltage-gated ion channels participate in the transduction process [42], with mechanogated channels hypothesized to be located near the neurite's filopodial [43].

Because of its elegant structure and important role in the somatosensory system, the PC has been the subject of numerous theoretical modeling efforts over the years, as discussed in Section 1.3. This study focuses specifically on two distinct neural responses of the PC to mechanical stimulation: band-pass filtering of oscillating stimuli [20,21] and rapid adaptation to sustained stimuli [50]. Although such behavior is relatively easy to capture with a functional model [105,108], and previous mechanistic models [23,32] have shown some aspects of the band-pass behavior, the detailed filtering mechanism and the adaptation of the PC to steady stimuli remain open topics. Building on the work described in Section 1.3, we aim to unify these observations via a detailed mechanistic model of PC response to mechanical stimulation, requiring a multiphysics, multiscale approach. To our knowledge, the current study was the first to provide a comprehensive mechanistic model of both the mechanical and the neural response of the PC to stimulation while accounting for the fine morphology of the neurite and the three-dimensionality of the PC. In addition to its fundamental significance as a window into the inner workings of a component of our tactile system, this work also lays the foundation for developing new ideas in design of haptic feedback systems and/or neural prosthetics. Modeling the mechano-to-neural response of the PC to a vibrotactile stimulus is a first step towards understanding vibrotactile perception in glabrous skin, and it can provide insight into response properties necessary for the development of haptic devices, such as stimulus detection threshold and the distinguishability of different vibrotactile stimuli and locations [114].

The objective of this study was to address three separate aspects of PC behavior: (1) The PC's structure allows it to act as a band-pass filter to vibration, (2) PC size affects the mechanical and thus the neural response of the PC, and (3) The structure of the end organ is conducive to receptor adaptation to a sustained stimulus.

To achieve our objectives, a three-stage computational model (Figure 3.1) was developed and used to address how the PC's characteristic structure and morphology govern its neural response to mechanical stimulation. The model consists of three separate models applied in series: (1) A finite-element mechanical model of the PC's outer core in MATLAB, (2) A finite-element mechanical model of the inner core and neurite in COMSOL, and (3) An electrochemical model of the neurite in NEURON. The input to

Stage 1 is a mechanical stimulus applied to the outer surface of the PC, and the output of Stage 3 is the neural response to that stimulus.

3.3 Methods

The three-stage model depicted in Figure 3.1 was created.

3.3.1 Stage 1: Outer core spherical shell mechanical MATLAB model

A detailed model of the lamellar layers of the PC outer core was developed to account for fluid-solid interaction and to model the mechanical transmission of vibratory stimuli through the outer core. Elastic shells were separated by lubricating layers, with an incompressible core at the center. This model was developed in MATLAB and is depicted in Figure 3.2.

3.3.1.1 Lamellar component (spherical shells)

The mechanics of the lamellae were modeled with the equations of equilibrium for spherical shells based on classical shell theory [141]. The following conditions for equilibrium of linear shell theory were met:

- *Thin structure*. Typical lamellae are ~ 0.2 um thick (cat mesentery [36]) and have surface dimensions of microns to millimeters [18,35], so the thickness is very small compared to the other length scales in the problem. This thinness allows the geometry of each layer to be treated in terms of a single position (midsurface) and thickness.
- *Small displacements and strains*. The PC is sensitive to vibrational stimuli in the nm-μm amplitude range [18,20,70], much smaller than the characteristic surface dimensions of the lamellae.
- *Negligible inertia*. The dimensionless quantity

$$\frac{\rho R^2\omega^2\left(1-\nu^2\right)}{E} \sim 0.0001 \tag{3.1}$$

for the parameter values used and frequencies of 1000 Hz, indicating that the applied oscillations are much slower than the natural frequencies of the sphere (see Ref. [142]), so inertia may be neglected, and the shells may be treated as in quasi-static mechanical equilibrium.

As a further simplification of the tissue mechanics, the lamellae were approximated as spherical shells. Since the PC is actually ellipsoidal, the spherical model represents one limit, while the cylindrical models of Loewenstein and Skalak [23] and Biswas et al. [32] represent the other. For each shell, force and moment balance equations were defined (Eqs. 3.2-3.18). Geometric variables for each shell are depicted in Figure 3.3.

(1) Equations of equilibrium

$$(\sin\varphi N_\varphi),_\varphi + N_{\theta\varphi},_\theta - (\cos\varphi)N_\theta + Q_\varphi \sin\varphi + aq_\varphi \sin\varphi = 0 \tag{3.2}$$

$$(\sin\varphi N_{\varphi\theta}),_\varphi + N_\theta,_\theta - (\cos\varphi)N_{\theta\varphi} + Q_\theta \sin\varphi + aq_\theta \sin\varphi = 0 \tag{3.3}$$

$$(\sin\varphi Q_\varphi),_\varphi + (\sin\varphi)N_\varphi - (\sin\varphi)N_\theta + Q_\theta,_\theta + aq_m \sin\varphi = 0 \tag{3.4}$$

$$-(\sin\varphi M_{\varphi\theta}),_\varphi + M_\theta,_\theta - (\cos\varphi)M_{\theta\varphi} + aQ_\theta \sin\varphi = 0 \tag{3.5}$$

$$(\sin\varphi M_\varphi),_\varphi + M_{\theta\varphi},_\theta - (\cos\varphi)M_\theta - aQ_\varphi \sin\varphi = 0 \tag{3.6}$$

where N is used to denote membrane forces, Q represents shear forces, and M indicates bending or torsional moments; the radius of the shell is a, and q is the load vector.

(2) Constitutive equations

$$N_\varphi = \frac{Eh}{1-\nu^2}(\varepsilon_{\varphi\varphi} + \nu\varepsilon_{\theta\theta}) \tag{3.7}$$

$$N_\theta = \frac{Eh}{1-\nu^2}(\varepsilon_{\theta\theta} + \nu\varepsilon_{\varphi\varphi}) \tag{3.8}$$

$$N_{\varphi\theta} = \frac{Eh}{2(1-\nu)}\varepsilon_{\varphi\theta} \tag{3.9}$$

$$M_\varphi = \frac{Eh^3}{12(1-\nu^2)}(\kappa_\varphi + \nu\kappa_\theta) \tag{3.10}$$

$$M_\theta = \frac{Eh^3}{12(1-\nu^2)}(\kappa_\theta + \nu\kappa_\varphi) \tag{3.11}$$

$$M_{\varphi\theta} = \frac{Eh^3}{12(1+\nu)}\kappa_{\varphi\theta} \tag{3.12}$$

where h is shell thickness, E is Young's Modulus, ν is Poisson's ratio, ε signifies the membrane strain tensor, and κ is the curvature tensor.

(3) Kinematic equations

$$\varepsilon_{\varphi\varphi} = \frac{1}{a}(u_\varphi,_\varphi + u_n) \tag{3.13}$$

$$\varepsilon_{\theta\theta} = \frac{1}{R_o}(u_\theta,_\theta + (\cos\varphi)u_\varphi + (\sin\varphi)u_n) \tag{3.14}$$

$$\varepsilon_{\varphi\theta} = \frac{1}{a}u_\theta,_\varphi + \frac{1}{R_o}(u_\varphi,_\theta - (\cos\varphi)u_\theta) \tag{3.15}$$

$$\kappa_\varphi = -\frac{1}{a}\left[\frac{1}{a}(u_n,_\varphi - u_\varphi)\right],_\varphi \tag{3.16}$$

$$\kappa_\theta = -\frac{1}{R_o^2}(u_n,_\theta - (\sin\varphi)u_\theta),_\theta - \frac{\cos\varphi}{aR_o}(u_n,_\varphi - u_\varphi) \tag{3.17}$$

$$\kappa_{\varphi\theta} = \frac{1}{2}\left\{-\frac{1}{a}\left[\frac{1}{R_o}(u_n,_\theta - (\sin\varphi)u_\theta)\right],_\varphi - \frac{1}{aR_o}(u_n,_\varphi - u_\varphi),_\theta + \frac{\cos\varphi}{R_o^2}(u_n,_\theta - (\sin\varphi)u_\theta)\right\} \tag{3.18}$$

where

$$R_o = a \sin\varphi \tag{3.19}$$

and the components of the displacement vector are u_n, u_θ, and u_φ (Figure 3.3).

3.3.1.2 Interlamellar fluid component

The behavior of the inter-lamellar fluid was modeled using Eq. 3.20, which describes fluid flow through a thin layer on a spherical surface. The lubrication approximation was used because of very thin geometry.

$$\sin\varphi \frac{\partial H}{\partial t} - \frac{1}{r^2} \frac{\partial}{\partial \varphi} \left(\frac{H^3}{12\mu} \sin\varphi \frac{\partial p}{\partial \varphi} \right) = 0 \tag{3.20}$$

where φ is angle measured from the vertical, H is fluid layer thickness, r is fluid layer centerline radial position, μ is fluid viscosity, and p is fluid pressure.

3.3.1.3 Fluid-lamellae coupling

Consider a series of lamellar shells (k = 0 to N) with interspersed fluid layers (m = 1 to N), with fluid layer m separating lamellae m-1 and m, and lamella k separating fluid layers k and k+1. Lamella 0 borders the inner core, to be discussed separately, and lamella N is the outer surface of the structure. Under the assumptions of linearity and negligible inertia, shell k must always be at equilibrium with the fluid layers above and below it, and the problem is linear, so when the mechanical equilibrium equations are discretized via finite-elements, the resulting equation can be expressed as

$$\mathrm{A}^{\mathrm{k}}\mathrm{u}^{\mathrm{k}} + \mathrm{B}^{\mathrm{k}}\mathrm{p}^{\mathrm{k}} - \mathrm{B}^{\mathrm{k}}\mathrm{p}^{\mathrm{k+1}} = 0 \tag{3.21}$$

where A represents a linear spatial differential operator describing the lamellae and the B's result from the fluid pressure in the surrounding fluid domain. In the fluid layer, since the pressure field depends on the velocity of the lamellae via $\partial H / \partial t$ and the equations are again linear in in p and v and the amplitude of the oscillation is small enough that the H^3 term may be treated as a constant, we have

$$C^{m-1}v^{m-1} - C^{m}v^{m} + D^{m}p^{m} = 0 \tag{3.22}$$

where C and D are likewise linear. For a forcing frequency ω, we can postulate a solution of the form

$$u = u_s \text{sin}\omega t + u_c \text{cos}\omega t \tag{3.23}$$

$$p = p_s \text{sin}\omega t + p_c \text{cost}\omega t \tag{3.24}$$

which implies that

$$v = \omega u_s \text{cost}\omega t + (-\omega) u_c \text{sin}\omega t \tag{3.25}$$

Substituting into the original equations and grouping sine and cosine terms gives

$$A^{k}u_s^{k} + B^{k}p_s^{k} - B^{k}p_s^{k+1} = 0 \tag{3.26}$$

$$A^{k}u_c^{k} + B^{k}p_c^{k} - B^{k}p_c^{k+1} = 0 \tag{3.27}$$

$$(-\omega)\, C^{m-1}u_c^{m-1} - (-\omega)\, C^{m}u_c^{m} + D^{m}p_s^{m} = 0 \tag{3.28}$$

$$\omega\, C^{m-1}u_s^{m-1} - \omega\, C^{m}u_s^{m} + D^{m}p_c^{m} = 0 \tag{3.29}$$

which can then be solved for the p's and u's simultaneously. For example, in the case of two lamellae (0 and 1) and one fluid layer (1), the equations would be as follows:

$$\begin{bmatrix} A^0 & 0 & -B^0 & 0 & 0 & 0 \\ 0 & A^0 & 0 & -B^0 & 0 & 0 \\ 0 & -\omega C^0 & D^1 & 0 & 0 & \omega C^1 \\ \omega C^0 & 0 & 0 & D^1 & -\omega C^1 & 0 \\ 0 & 0 & B^1 & 0 & A^1 & 0 \\ 0 & 0 & 0 & B^1 & 0 & A^1 \end{bmatrix} \begin{bmatrix} u_s^0 \\ u_c^0 \\ p_s^1 \\ p_s^2 \\ u_s^1 \\ u_c^1 \end{bmatrix} = f \tag{3.30}$$

where f, the right-hand-side vector, is zero except for any non-zero boundary conditions (if f is zero, the solution is the trivial solution that u = v = p = 0 everywhere). The non-zero terms in f are tied to stimulus functions.

The solution of this system by the standard Galerkin finite-element method gives u and p as a function of position (from the finite-element basis functions and nodal values) and time (from the sine and cosine dependences in Eq. 3.25).

3.3.1.4 Parameter selection

Two parameter sets (Table 3.1) were considered based on the work of Lowenstein and Skalak [23] (henceforth LS) and Biswas et al. [32] (henceforth BMS, including examining different fluid viscosities). Pressure was applied to the surface of the outer shell (from $\varphi = 0°$ to 90°) using a pressure field of the form

$$p(\varphi, t) = \left[\frac{1}{3} + \cos(2\varphi)\right]\sin(\omega t) \tag{3.31}$$

This form was selected so as to integrate to zero over the sphere's surface and thus ignore purely hydrostatic contributions. The pressure was applied to the outer surface at frequencies from 10 Hz to 100 MHz. It is important to note that while outside both the normal detection range of the PC and assumptions of the current model, the upper bound of the applied frequency was necessary to simulate the model's response when LS parameters were used. After initial analysis, the BMS parameters were chosen for use in subsequent simulations. Thus, the elastic modulus of each lamella was 1 kPa, and the fluid viscosity was 1.4 mPa-s. The thickness of each lamellar layer was set at increasing values between 0.1 and 0.4 μm using a Weibull function, as suggested by Biswas et al. [32]. The number of shells was set at 30 [18,36], except for simulations in which the PC size varied.

3.3.1.5 Sustained pressure simulations

The PC response to steady pressure was simulated by applying square wave displacements to the outer shell. PC simulations were run at sinusoidal inputs of 0.5 Hz,1.5 Hz, …, 1000.5 Hz. The resulting displacements (u) of the inner and outer shells at each frequency were summed according to Eq. 3.32 to obtain the resulting displacements (Δ) from a square wave indentation.

$$\Delta(t) = \frac{4}{\pi} \sum_{f=0.5}^{1000.5} \frac{u_s \sin(2\pi ft) + u_c \cos(2\pi ft)}{2f} \tag{3.32}$$

3.3.2 Stage 2: Inner core and neurite mechanical COMSOL model

Inner core and neurite simulations were performed on the COMSOL finite element platform using the *Solid Mechanics* interface and a *Frequency Domain* study to compute neurite mechanics in response to vibrations from the innermost shell in Stage 1.

The inner core was modeled as a 600 μm sphere of material. The neurite was modeled as a cylinder with length 600 μm and diameter 3 μm [35]. The neurite had a bulbous ending with a diameter of 10 μm at the distal end to represent the geometry of the ultra-terminal portion of the neurite. Five filopodia (2 central, 3 distal) were attached to the neurite as shown in Figure 3.4. Each filopodium was modeled with a length of 1.6 μm and a diameter of 0.6 μm [18]. The domain was discretized into 153,803 tetrahedral linear finite elements.

The neurite domain was modeled as an isotropic linearly elastic material with a Young's modulus of 7kPa [143], Poisson's ratio of 0.49, and density of 1000 kg/m^3. The inner core domain was specified to be 100 times stiffer than the neurite, as no values for the stiffness of the tightly-packed inner core are reported in the literature. Damping was modeled by an isotropic loss factor of 0.2. The inner core's outer boundary received a prescribed displacement equal to that of the innermost shell in Stage 1. Simulations were run at 10-1000 Hz. The first principal strains at the base of each filopodium were measured at each phase of indentation for the COMSOL simulations at various frequencies.

3.3.3 Stage 3: Electrochemical neurite model

NEURON is a simulation environment that can be used to model single neurons or networks of cells. A topological model of the finite-element neurite modeled in COMSOL was constructed in NEURON. The geometry of the neurite included four structural groups:

(1) Region A: five filopodia (three distal, two central), modeled as dendrites,
(2) Region B: a neurite along the inner core of the PC, modeled as two somas connected at the two central filopodia,
(3) Region C: a bulbous soma at the ultra-terminal portion of the neurite, and
(4) Region D: the neurite's spike initiation zone, modeled as an axon.

The model parameters are found in Table 3.2. The topology of the NEURON model can be seen in Figure 3.5. The spatial grid listed in Table 3.2 was used. A mesh convergence study was performed, and it was found that a tenfold refinement produced less than a 1% change in the computed firing rate, so the mesh was deemed sufficiently refined.

Hodgkin-Huxley channels were inserted into Regions A and C, as both voltage-gated and nonvoltage-gated channels have been located in PCs and may be involved in mechanotransduction [40,42]. The sodium channel conductance in Region A was set to 0.12 S/cm^2, the default in NEURON. The sodium channel conductance in Region B was set to vary from 0.12 S/cm^2 at the proximal end to 0.24 S/cm^2 at its connection to Region C to represent an increase in channel density.

Point process current clamps were inserted at the base of each of the five filopodia (Region D) (Figure 3.6A). The opening of stretch-gated cation channels resulting from strain at the base of each filopodium was approximated by an increase in injected current. Strains at the base of each filopodium were obtained from the COMSOL simulations (Figures 3.6B and 3.6C). Absent direct information about PC cation channels, mechanotransducer currents from rat DRG sensory neurons [144] were used. A sigmoidal curve of activation (Figure 3.6D) was constructed based on the activation time constants of a rapidly relaxing current [144]. The first principal strain at the base of each filopodium during one oscillation at 120 Hz is shown in Figure 3.6C, and the resulting channel activation is shown in Figure 3.6E. The sigmoid function output was inserted as current at the base of the corresponding filopodium in the NEURON model at the indentation frequency.

Simulations were run in NEURON (Version 7.3) for 1000 ms with a time step of 25 μs. The resting membrane potential was initiated to NEURON's default of -65 mV for each simulation. The membrane potential was recorded at the promixal end of the axon.

3.4 Results

Simulations were run at frequencies spanning 10 Hz - 100 MHz to observe the effect of varying the input frequency in a sinusoidal oscillation applied to the PC's outer surface. The three-stage model was then used to explore the effect of PC size on the transmission and encoding of vibratory stimuli, and finally to predict the response to a sustained stimulus.

3.4.1 Frequency sweep

3.4.1.1 Stage 1

It has been suggested [18,23] that interaction between fluid and lamellae in the PC's outer core is responsible for the PC's role as a high-pass filter to vibrations. A detailed mechanical model of the alternating fluid and lamellar layers in the outer core was developed. The Stage 1 model contained 30 layers of concentric spherical shells separated by thin lubricating fluid layers.

Sinusoidal oscillations applied to the outer surface of the Stage 1 model caused the inner shell to strain in a frequency-dependent manner (Figure 3.7A). Two different sets of parameters were considered: those from the classic work of Loewenstein and Skalak [23] (LS), and those from more recent analysis by Biswas, Manivannan, and Srinivasan [32] (BMS). Simulations run using the BMS parameters resulted in peak strains within the frequency range of PC sensitivity [18,20], with the peak shifting to lower frequencies with increasing fluid viscosity. Simulations run using the LS parameters peaked at a frequency outside of the PC sensitivity range. All subsequent simulations were run using BMS parameters and a fluid viscosity of 1.4 mPa-s.

The deformation of each shell layer was recorded. Figure 3.7B shows the deformation of five representative shells at maximum displacement during a 150 Hz simulation. Although the displacements are smaller for more central layers, the relative displacement is largest near the core. This effect is quantified in Figure 3.7C, which shows that the radial stretch ($\Delta r/r_o$) of shells increased with proximity to the inner core for a 1 μm amplitude vibration at 150 Hz. Thus, at the optimal frequencies for inner:outer shell displacement, the outer portion of the PC is acting as a *strain amplifier*, producing roughly four times larger strains in the inner core than would occur in a homogenous structure. The lamellar structure of the outer core is not merely a high-pass filter, eliminating low-frequency information through fluid motion [23]; it also amplifies the strain in the PC's target frequency range.

3.4.1.2 Stage 2

A second computer model was created to account for the morphology of the PC neurite, whose complex structure could not be captured in the spherical model of Stage 1. A COMSOL model was created that included both the spherical inner core and an anatomically realistic [18,35] neurite. Simulations of the inner core and neurite were performed in COMSOL's frequency domain mode to compute neurite mechanics in response to vibrations of the inner core.

The inner core surface in the COMSOL model was displaced by the amount predicted by the Stage 1 model for the innermost shell. Regions of largest strain occur near the filopodia at the central and distal ends of the neurite (Figure 3.8), suggesting that mechanogated cation channels at the base of the filopodial [27] would be well positioned to transduce information about the applied deformation. At peak displacement, strain was amplified from the inner core surface to the neurite by a factor of 2 at the bases of the central filopodia and a factor of 3 at the bases of the distal filopodia. Thus, combining the Stage 1 and Stage 2 model results, we see that the strain at the base of a filopodium can be ten times larger than that at the PC's outer surface.

3.4.1.3 Stage 3

An electrochemical model was created in NEURON to convert the strain on the neurite membrane into the opening of stretch-gated cation channels located at the filopodial bases, and the firing rate in response to current injection gated by the Stage 2 neurite strains was calculated. Bolanowski and Zwislocki's experimental firing rates recorded from PCs stimulated with sinusoidal indentations at increasing displacement [20] are shown opposite simulated neurite firing rates from the Stage 3 model (Figures 3.9A and 3.9B). The displacement range between the tuning and response thresholds increased with indentation frequency in experiments by Bolanowski and Zwislocki (Figure 3.9C) and simulations (Figure 3.9D). In both experiments and simulations, low frequency indentations required the highest amplitudes to elicit action potentials, with intermediate and high frequencies requiring smaller amplitudes. Simulations showed peak sensitivity (i.e., response to the smallest amplitude stimuli) at 150 Hz, which was also the indentation frequency that produced the largest neurite strains in Stage 2. The sensitivity of the model PC at intermediate frequencies could be adjusted further to match Bolanowski and Zwislocki's data by varying, e.g., interlamellar fluid viscosity, lamellar stiffness, and number of lamellae. We chose not to do so in the current study because of the relatively small amount of experimental data and our desire to capture the general trend instead of one specific PC.

3.4.2 PC size sweep

Stage 1 model simulations were run for spheres of 2 to 30 layers, and the radius of the simulated spherical PC increased with the number of layers. The strain transmitted through the lamellar layers is shown for different frequencies and PC sizes in Figure 3.10A. As the number of layers increased, the peak amplification factor increased, and the frequency at peak amplification shifted to the right (Figure 3.10B). The difference in amplification could potentially allow a cluster of different-sized PCs to encode more amplitude information (because different PCs would have different sensitivity) and/or more frequency information (because of different peak frequencies) than a single PC or a cluster of identical and therefore redundant PCs.

A more detailed view of the difference in response can be seen in Figures 3.10C and 3.10D, which show phase plots of inner shell vs. outer shell displacement for two PC sizes (20 and 30 shells) during 100 Hz and 1 kHz simulations. For a purely elastic system, the inner and outer shell displacements would be in phase, and the plot would be a line; a more circular plot indicates a greater role of interlamellar fluid viscosity and more energy dissipation. In the 100 Hz – 1 kHz frequency regime, higher frequency (Figure 3.10D vs. 3.10C) leads to a more elastic response, and adding more layers increases the viscous effect. Our results for 100 Hz vs. 1kHz (Figures 3.10C and 3.10D), are consistent with those of the previous model by Biswas et al., in which the PC stiffness increased with increasing frequency, as indicated by a lower lamellar compliance [32].

3.4.3 Sustained indentation

To simulate sustained pressure, square wave displacements were generated via a Fourier series and applied to the Stage 1 model. The outer shell was stimulated by a square wave with a period of 2 s (as seen in Figure 3.11A). In response, the inner shell of the PC showed large displacements at the onset and offset of the square wave, as seen in Figures 3.11B and 3.11C. Thus, the PC adapts mechanically in response to the sustained pressure, as the inner core is displaced only during onset and offset of the stimulus, as seen experimentally [50]. The mechanical displacements from square wave indentation were passed through Stages 2-3 of the model, which resulted in action potentials only at stimulus onset and offset, reproducing the rapid adaptation seen in the literature [11].

3.5 Discussion

The major contribution of this work is a comprehensive model that includes the entire mechanotransduction process of the PC by combining three stages that deal with specific components of the process, simulating PC response to both vibratory and sustained indentation, and accounting both for PC core structure and neurite morphology. A unique aspect of this work is the focus on the mechanical properties and a realistic anatomical description, including the three-dimensional structure of the outer core, the neurite, and the neurite's filopodia. The focus on three-dimensional structure sets this model apart from previous studies [23,32], as our model includes the neurite morphology and represents the outer core as a series of spheres, rather than as a series of cylinders. While the shape of the PC is more ellipsoidal than spherical, it has been shown that the ellipsoidal shape alone does not affect the displacement through the PC in static indentation simulations [109]. Therefore, it is likely that modeling concentric ellipsoidal instead of spherical shells in Stage 1 will not have a large effect on the overall results of the current study. Another key advantage of this model is that it provides insight into two key factors that are integral to the PC's transduction process (lamellar compression and neurite strain). By integrating three distinct and detailed stages describing individual components hypothesized to play a role in transduction, we were able to assess the importance of various factors while also simulating the entire transformation of a mechanical input into a neural output.

A 10 Hz – 1 kHz frequency sweep was performed for all three stages of the model, extending to 100 MHz in Stage 1. In Stage 1, we identified how a vibratory displacement was transmitted from the outer to the inner shell and observed how these results changed with PC size and mechanical properties (Figures 3.7A and 3.10A). In Stage 2, we simulated the strain at the base of five filopodia on the neurite surface (Figures 3.6B and 3.8). In Stage 3, we performed a frequency sweep while also adjusting stimulus amplitude and calculated the resulting action potential firing rates (Figure 3.9B). Lamellar compression, neurite strain, and spiking sensitivity peaked in the 120-150 Hz range for the selected mechanical properties. This frequency range can be adjusted by varying mechanical and geometric properties in the simulations. The Stage 1 frequency sweep results show that incorporating the layered PC structure introduces the band-pass filtering response, as suggested previously [23], and that increasing the number of layers in the outer core increases filter sensitivity (Figure 3.10A). This study suggests that it is not only the presence of fluid and shells but also the three-dimensional geometry and the interaction between adjacent layers that allow for stretch amplification in layers closer to the core and the subsequent activation of mechanogated channels on the neurite.

Our model also provides insight into how the interaction between lamellae and the interlamellar fluid affects the PC's mechanical response, suggesting that three mechanical regimes arise. At low stimulation frequency, only the outer shells move in response to indentation, and the inner shells do not move. At the other extreme of very high stimulation frequency, fluid viscosity causes the entire structure to deform with no phase shift, with this effect becoming more pronounced with the number of layers (Figure 3.10D). In the middle regime, viscosity plays an important role as it transmits pressure between adjacent shells and causes a phase shift between the inner and outer shells (Figure 3.10C). These results are in agreement with those of Biswas et al. [32], in which the phase response moves towards 90° in the middle frequency regime (1-50 Hz) and decreases at lower and higher frequencies. In addition, Biswas et al.'s results also show that phase shift increases with increasing number of shells.

A unique feature of this model is the quantification of strain amplification from the PC surface to the location of mechanogated channels on the neurite and the three-dimensional distribution of this strain. Strain was amplified by a factor of 4 from the PC outer shell to the inner shell in Stage 1 and is again amplified by a factor of 2-3 from the inner shell to the neurite surface. Thus, PC strain amplification from the surface to the location of mechanogated cation channels occurs by a factor of 8-12. The magnitude of strain amplification is affected by factors such as PC size (Figure 3.10A) and location of mechanogated channels on the neurite surface (Figure 3.8A). These results, combined with the high sensitivity of mechanogated channels [145], help explain how the PC, with a length scale on the order of millimeters, is sensitive to vibrations in the nm-μm amplitude range [18,20,70].

The PC is typically found within glabrous skin and subcutaneous tissue [18]. The current study focused on an isolated PC, as no electrophysiological data currently exist for PCs embedded within their native tissue. It is important, however, to consider the PC's location within the skin to understand how the surrounding tissue influences the PC's response to tactile stimuli, which has been the focus of previous studies [30,115,146,147]. Quindlen et al. [115] modeled the effect of embedding the PC within skin at different depth levels (dermis vs. epidermis) during static indentation and concluded that the PC's depth contributes to the size of its receptive field, with deeper PCs exhibiting larger receptive fields and thus lower special sensitivity. Embedding our three-stage model within a skin model would affect the stimulus amplitude delivered to the PC surface and provide insight into the neural response to varying the spatial location of the vibrotactile stimulus. Other studies [148] have investigated the propagation of vibrations and found that information about a vibrotactile stimulus is transmitted across the surface of the hand. The current model could be combined with a model of skin mechanics to simulate the propagation of mechanical waves both across the surface of skin and into the depth of skin to study how spatially-distributed PCs respond to a vibrotactile stimulus.

The distribution and number of PCs can vary among species [18,34] and among individuals within species [17]. The shape and size of PCs can also vary between anatomical locations and with age [16–18]. Our study indicates that as the PC increases in size (e.g., with increased age [16]), which is modeled by the addition of new lamellae [16], its ability to amplify strain increases (Figure 3.10B). The filtering properties of the simulated PC also change, as its pass band also widens with increasing size, consistent with previous theoretical studies [32]. Additionally, PCs can be found in clusters of multiple receptors, which can result in overlap between receptive fields [81], and the receptors within a cluster may have different sizes (Figure 3.1B). Experiments on isolated PCs [149] concluded that activity from more than one PC may be required to reach a psychological threshold, suggesting that the distribution of sensitivities within a population of PCs would determine the overall response of the group. Our results indicate that clustering PCs of different sizes would result in a population of various sensitivities. For example, our simulations (Figures 3.10A and 3.10B) suggest that adjacent PCs consisting of 20 and 30 shells would result in a pairing of receptors most sensitive to 50 and 120 Hz vibrations, respectively. Clustering of different sized PCs may be an efficient way to send information about a complex vibratory stimulus and may improve cutaneous sensation. PCs in a cluster are typically aligned along the same long axis [18], further suggesting that a cluster of PCs may work together to sense different components of a complex stimulus rather than functioning individually to detect different stimuli. Likewise, difference in PC size across clusters may also result in more nuanced tactile encoding. It is important to recognize that the model presented in this study does not simulate the propagation of neural activity between higher order neurons; therefore, our model simulates the strain experienced by the nerve fiber of the first order neuron that innervates a single PC and does not simulate the complex integration of neural activity within a cluster. While simulating the collective neural activity and signal processing of a cluster of PCs would require a more complex, higher-order model, the results of this study suggest a possible reason why a cluster may contain PCs of different shapes and sizes and how the inhomogeneity may affect the information encoded in a vibrotactile stimulus.

In the current study, mechanogated channels were assumed to open in response to increased strain, causing an influx of cations and neurite depolarization. Previous studies have used various microscopy techniques to analyze cytoplasmic protrusions (filopodia) on the terminal portion of the neurite and have identified structural differences between the filopodia and the rest of the neurite [43–46]. These findings have led to the suggestion that different physiological processes may occur in the filopodia and that they may be the site of mechanotransduction on the neurite [43]. Filopodia are also located in other rapidly-adapting receptors, such as Meissner corpuscles and muscle spindles [18]. While it has been hypothesized [43] that filopodia are the sites of mechanoelectric conversion, it is unknown exactly how this process occurs. The presence of actin in filopodia draws a parallel to the stereocilia of inner ear hair cells [43] and supports the hypothesis that filopodia are mechanotransduction sites in the PC [27]. Experiments have also identified voltage-gated sodium channels [40] and an abundance of mitochondria [48] located on and at the base of filopodia, suggesting that this region of the neurite can support action potentials. In the present study, we hypothesized that mechanogated channels were localized to the base of the neurite's filopodia rather than distributed along the entire length of the neurite due to published micrographs [43] that suggest this localization. We placed three filopodia at the terminal region of the neurite and two filopodia jutting into the cleft at the central region of the neurite [18,45]. The resulting high strains at the filopodial bases in Stage 2 simulations (Figure 3.8A) suggest that filopodia may be amplifying strain, so mechanogated channels at the filopodial base may be well positioned for mechanotransduction. Incorporating the detailed morphology of the neurite in our model allows us to observe the mechanical influence of the filopodia and its effect on the neurite strain, which governs the behavior of the mechanogated channels in our NEURON model and thus the simulated neural response to mechanical inputs.

Loewenstein and Mendelson [11] removed most of the capsule from isolated PCs and observed that the bare PC behaved as a slowly adapting receptor. They hypothesized that the PC's rapidly adapting response was purely a result of the mechanical properties of the capsule. More recent experiments by Pawson et al. [27] on isolated PCs have shown the receptor's characteristic rapid adaptation may be more than a purely mechanical effect and may involve chemical interactions between neurotransmitters since the application of GABA receptor antagonists resulted in action potential firing during a sustained pressure, while the application of glutamate receptor antagonists resulted in a decrease in the number of static spikes. Pawson et al. hypothesized a mechanochemical response in which GABA is released from the modified Schwann cells of the PC inner core at stimulus onset to inhibit glutamatergic excitation. Our results show that a sustained stimulus is transmitted through the PC's lamellae to the inner core at the stimulus onset and offset, but the inner core recovers rapidly to its original configuration. When a sustained stimulus was passed through our entire three-stage model, neural spiking occurred only at the onset and offset of the stimulus, with spiking occurring throughout the entire stimulus in a decapsulated model. While these are purely *mechanical* results that confirm the rapidly adapting properties of the PC, it is also possible that a *mechanochemical* process exists. Our study focuses on the role of the mechanogated channels in the PC's response to vibratory and sustained indentation, but it is possible that glutamate release could cause the PC to fire action potentials during a sustained stimulus.

While this work focuses on the role of mechanogated cation channels located at the filopodial bases, other ion channels may also play a role in the PC's mechano-to-neural transduction. Specifically, ion channels located on the non-neuronal cells of the PC's inner core may be involved in the transduction process. Acid-sensing ion channels (ASICs), which belong to the degenerin/epithelial sodium channel (DEG/ENaC) superfamily and are non-voltage gated channels, are expressed in sensory neurons and have been proposed to play a role in mechanotransduction [42,150–152]. Previous immunohistochemical studies have investigated the presence of ASICs in PCs and found ASIC1 protein expression in the neurites of human PCs [153] and ASIC2 expression in the neurites and inner core lamellar cells of human and murine PCs [152–154]. ASIC2 has also been detected in human Merkel cells and Meissner corpuscles [154]. The role of ASIC2 in PC mechano-to-neural transduction remains unclear. While ASIC2 knockout has not been shown to significantly alter cutaneous mechanosensation in mice [155], the presence of ASIC2 in low-threshold mechanoreceptors suggests a role in mechanotransduction [154]. In addition, immunocytochemical studies have detected voltage-gated sodium and potassium channels [40] and positive labeling for glutamate and glutamate receptors [26] on the inner core lamellar cells of the cat PC. In this study, we treated the lamellae of the PC capsule as purely mechanical components. However, the localization of ASIC2, voltage-gated channels, and glutamate on the non-neuronal cells of the inner core suggest a possible chemical involvement of the inner core in mechanotransduction.

The quantified neural output in the Stage 3 model is the mean action potential firing rate resulting from the opening of mechanogated cation channels, which is simulated by an injection of positive current into the neurite membrane proportional to the first principal strain measured at that location. The mean firing rate was selected as the measured output parameter due to the availability of firing rates measured in isolated PCs in the literature. Experimental PC firing rates in response to mechanical vibrations can approach 2X the stimulus frequency at high indentation amplitudes [20]. This plateau at a 2:1 firing rate is not predicted in the current model, suggesting that there are other features of the PC response beyond those captured in the current model. In addition, experimental PC spiking is probabilistic and thus it is important to note that the model created in this study is fully deterministic, and stochastic variations could be introduced to capture the probabilistic nature of the physiological response of the PC. Other studies [21] have recorded the receptor potentials of isolated PCs during sinusoidal vibrations, which were not addressed in the current study but can provide information about optimal NEURON parameters for a model of the PC neurite. There are other factors, such as the refractory period and temporal precision of PC afferent neural spiking, that have been the focus of other studies [104,106] that aim to more accurately reproduce the PC's entrainment to vibratory stimuli and model the temporal components of the resulting action potentials. In addition, the values for sodium channel conductance and resting membrane voltage in this model were set to the default parameter values in NEURON, which are based on the squid giant axon [41]. The usage of squid axon parameters as opposed to those of a mammalian neuron is a limitation of the Stage 3 model. The Stage 3 model is a conceptual model used to tie the mechanical contribution of the lamellae and neurite to the neural activity of the PC and could be further improved by including channel and membrane properties more similar to those of the mammalian PC neurite as such data become known. The model created in this study was a simple model created to measure the PC's firing rate and more complex neural phenomena can be analyzed into a future, larger study of PC firing.

3.6 Conclusions

The three-stage model developed in this study provides information about how mechanical properties, outer core structure, three-dimensional neurite morphology, and mechanogated channel activation play a role in the mechano-to-neural transduction of the PC. By addressing each component separately, we identified key aspects that affect the receptor's sensitivity. By addressing the components as a whole, we simulated the entire process in which a mechanical stimulus is transduced into a neural response within a single PC. By understanding this process in the PC, we can also begin to characterize the mechanosensation of other receptors and nerve endings and to explore how hundreds of receptors in a single hand interact to send detailed sensory feedback to our somatosensory cortex and create our sensation of touch.

Table 3.1: Stage 1 shell and fluid parameters

	LS [23]	**BMS** [32]
Elastic Modulus (Pa)	5e5	1e3
Lamellae Thickness (μm)	1	0.1-0.4
Viscosity (mPa-s)	1	1.4, 3.5, 7
Reference	Loewenstein and Skalak (1966)	Biswas, Manivannan, and Srinivasan (2015)

Table 3.2: Stage 3 topological parameters

Region	Section	Structure	Parameter	Value Used	Reference
A	Filopodia	Dendrite	Total number	5	
			Length	1.6 μm	Bell et al. (1994)
			Diameter	0.6 μm	Bell et al. (1994)
			Number of segments	1	
B	Terminal region of neurite	Soma	Total number	2	
			Length	300 μm	Quilliam and Sato (1955)
			Diameter	3 μm	Quilliam and Sato (1955)
			Number of segments	4	
C	Ultra-terminal bulbous ending	Soma	Total number	1	
			Length	10 μm	Quilliam and Sato (1955)
			Diameter	10 μm	Quilliam and Sato (1955)
			Number of segments	1	
D	Spike-initiating zone	Axon	Total number	1	
			Length	247 μm	Quilliam and Sato (1955)
			Diameter	5.8 μm	Quilliam and Sato (1955)
			Number of segments	4	

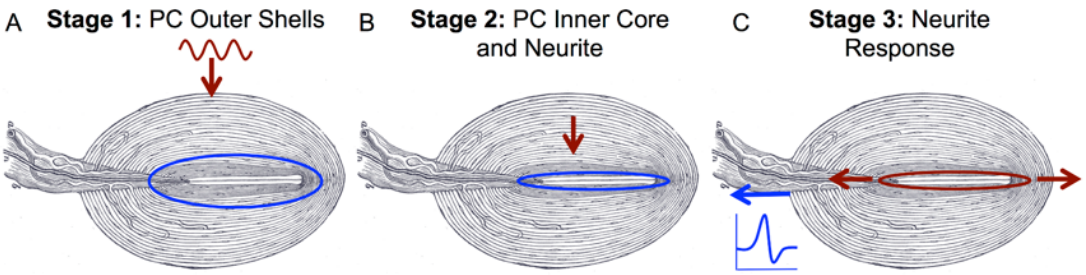

Figure 3.1: Schematic of three-stage model. (A) The PC outer shell (base image obtained from Ref. [156]) was mechanically stimulated (red), and inner core displacements (circled in blue) were obtained. **(B)** The PC inner core was stimulated (red) with the output of Stage 1, and neurite strains (circled in blue) were obtained. **(C)** Neurite stretches from Stage 2 (red) were used to control ion channel dynamics in a neural model, and action potentials (blue) were measured.

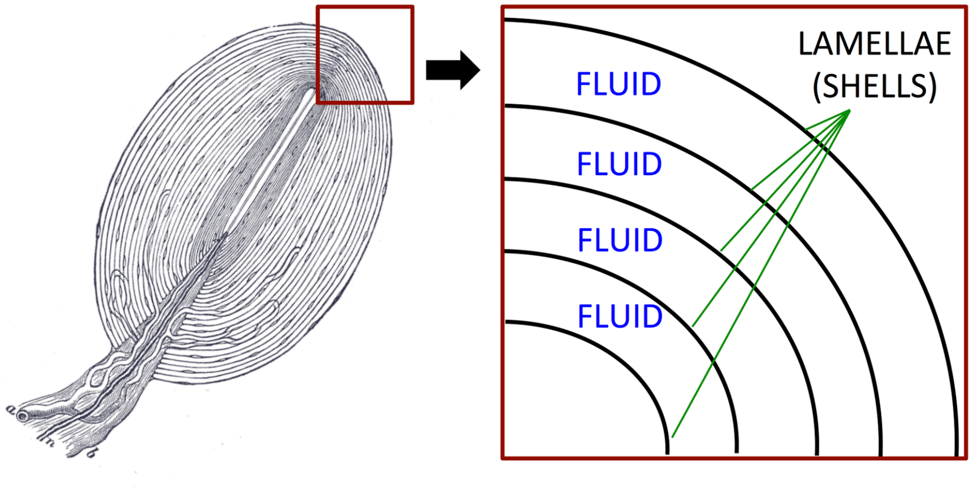

Figure 3.2: PC Sketch and Model Representation of the outer core. The PC in the model was represented as a series of shells (lamellae) with lubricating fluid in between each layer to account for the PC lamellar organization (left, base image obtained from Ref. [156]).

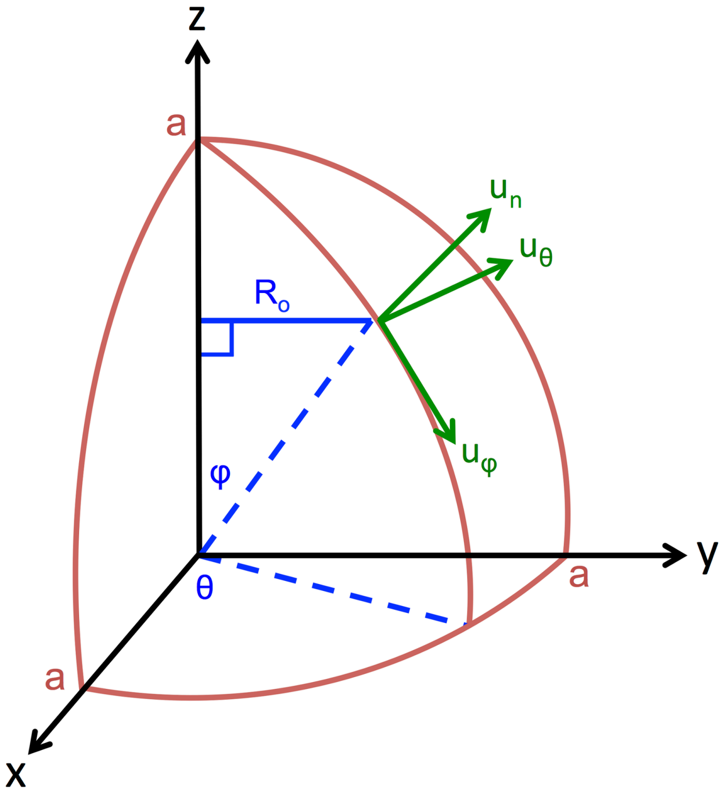

Figure 3.3: Stage 1 model. Variables used in Eqs. 3.2-3.19 to describe the geometry of each shell in the Stage 1 model.

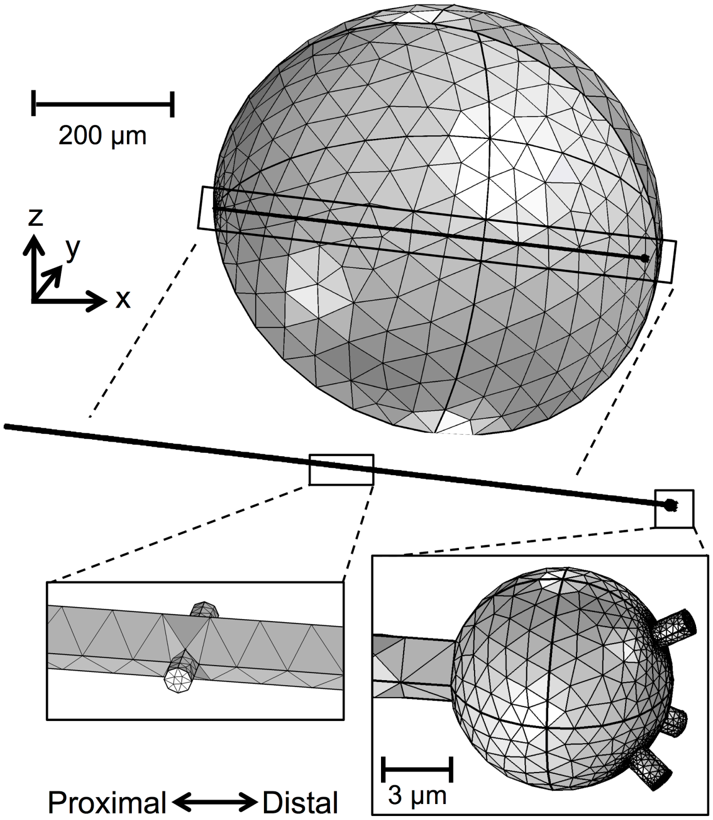

Figure 3.4: Stage 2 model. Inner core model from COMSOL, with areas of the neurite and its central and distal segments in detail.

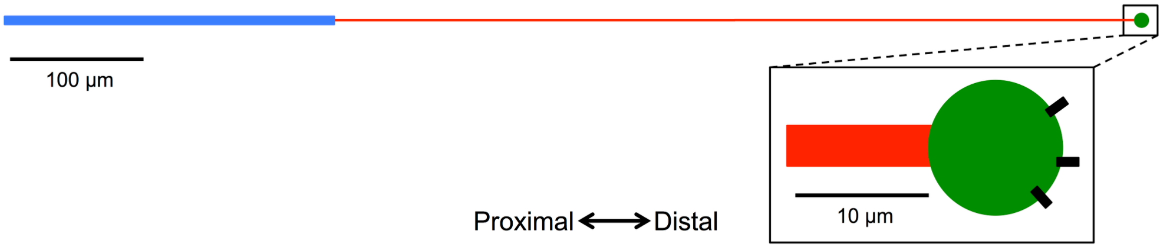

Figure 3.5: Stage 3 model. The topological connections of the spike-initiating zone (blue), terminal region of neurite (red), and ultra-terminal bulbous ending (green) used in the NEURON model. The terminal region of the neurite, including its distal filopodia (black) are shown in detail.

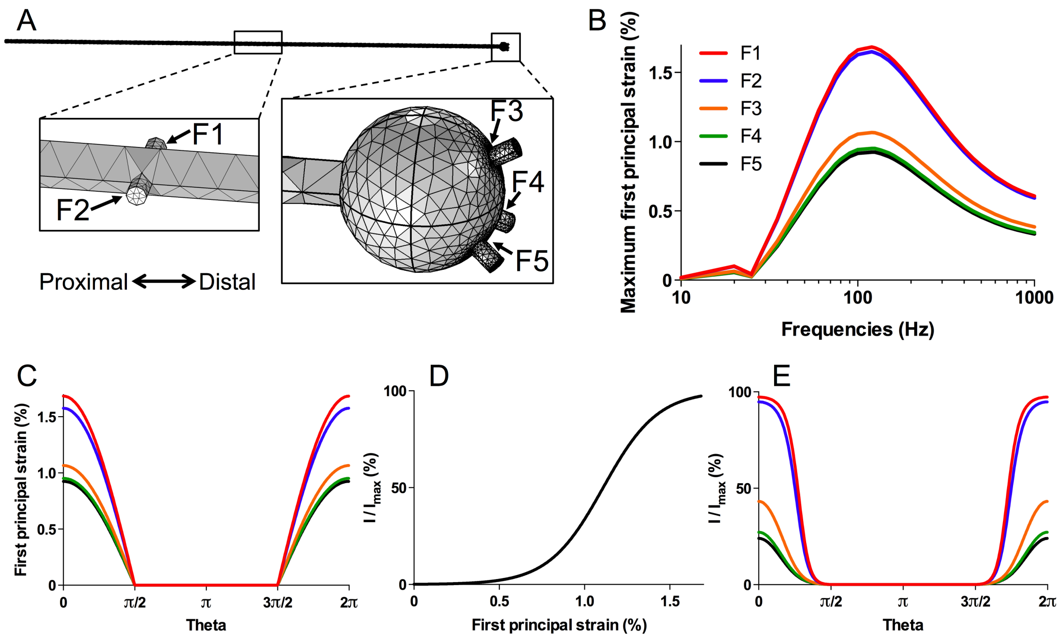

Figure 3.6: First principal strain to current conversion. **(A)** Neurite geometry from COMSOL with the five filopodia labeled F1-F5 for labeling in subsequent figures. **(B)** Maximum first principal strain at the base of each filopodium labeled in (A) at various indentation frequencies. **(C)** First principal strain at the base of each of the five filopoia during one oscillation of indentation for a 120 Hz simulation. **(D)** Sigmoid used to convert first principal strain into mechanically-transduced currents (percentage of maximum current). **(E)** Currents obtained for the 120 Hz simulation in (C).

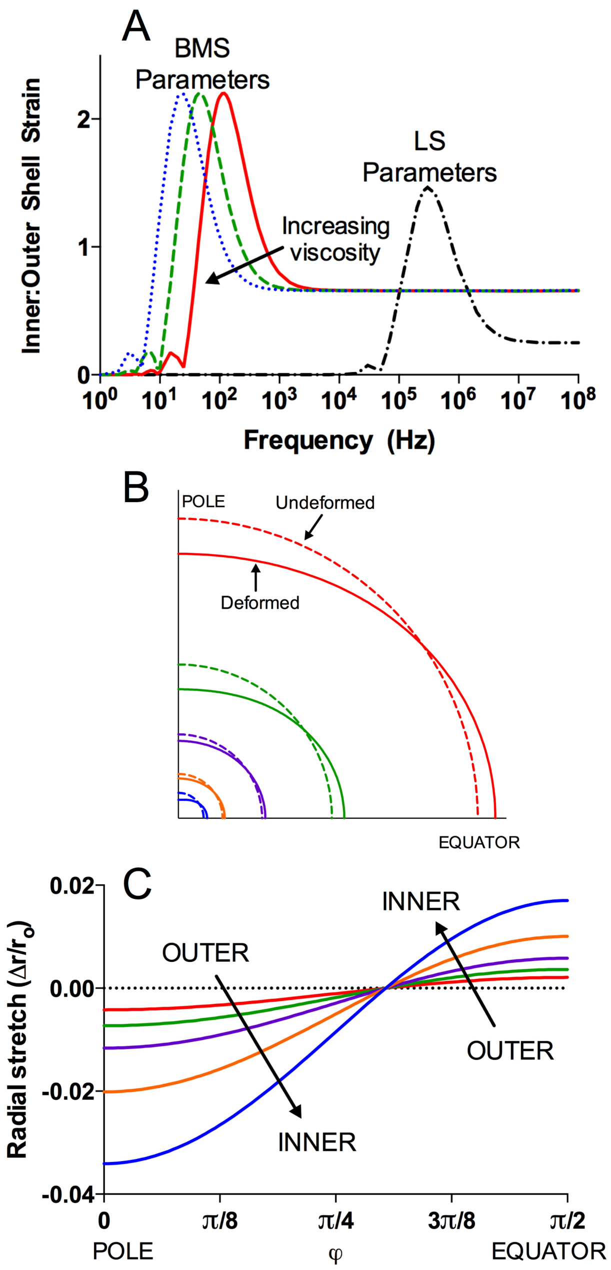

Figure 3.7: Stage 1 frequency variability results. (A) Ratio of the maximum radial strain for the innermost to outermost shells vs. frequency. Strain was calculated as $\Delta r / r_o$ at the innermost and outermost shell, where Δr is the maximum displacement and is r_o the original radius of the shell. Simulations run using BMS parameters resulted in peaks in the

frequency range of PC sensitivity, with the peak shifting to lower frequencies with increasing fluid viscosity. BMS simulations were run with viscosities of 1.4, 3.5, and 7.0 mPa-s. **(B)** Undeformed and deformed geometries of five shells. Shells 1, 8, 16, 23, 30 (distance from the core increases with increasing shell number) were plotted at peak displacement for 1.4 mPa-s viscosity simulations at 150 Hz. For visualization purposes, all displacements were artificially increased by a factor of 30. PC deformation had a larger effect on shape for layers closer to the core. **(C)** Radial stretch for five shells vs. angle φ measured from the indentation point ("POLE"). In the assumed spherical geometry, $\varphi = 0$ is the indentation point ("POLE") and $\varphi = \pi/2$ is the band around the sphere ("EQUATOR"). Deformation to the PC surface resulted in larger magnitudes of stretch in shells closer to its center. The radial stretches are plotted for the layers shown in (B) at peak displacement in a 150 Hz simulation with 1 μm indentation amplitude.

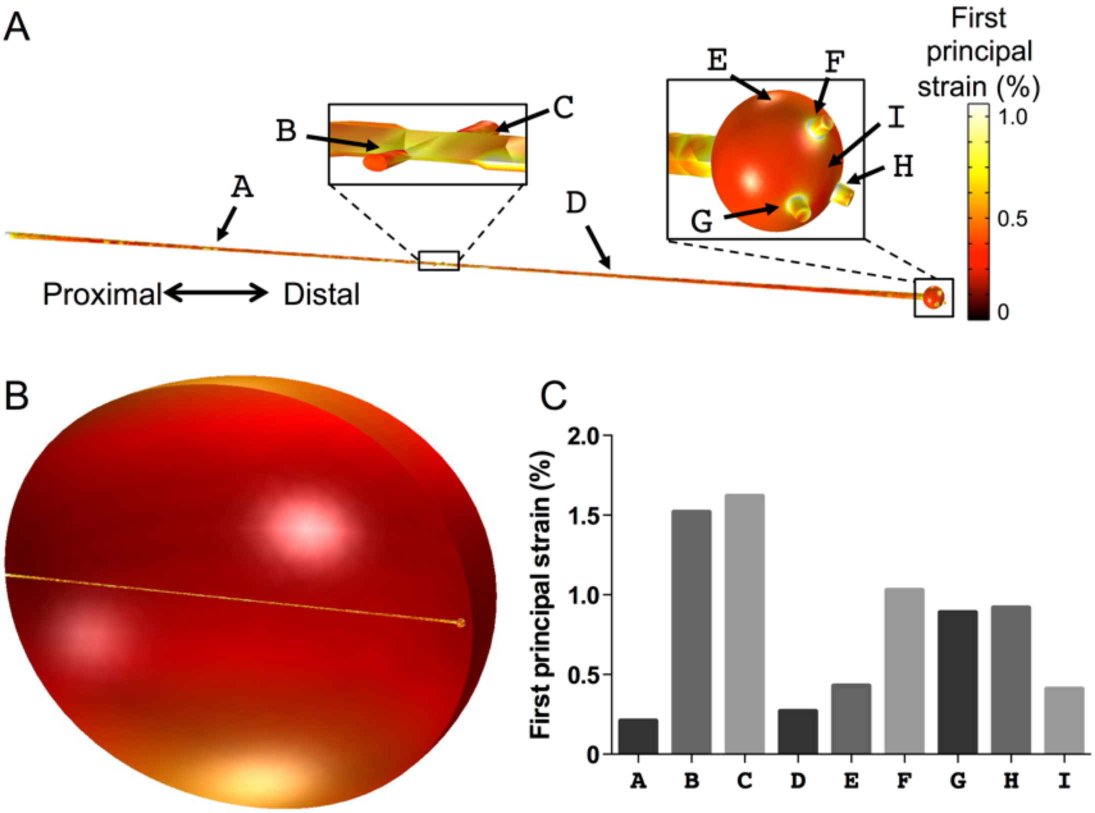

Figure 3.8: Stage 2 results at peak displacement in a 150 Hz simulation. (A) First principal strain along the surface of the neurite. A region of higher strain is located at the base of the filopodia. The strain is plotted at peak displacement in a 150 Hz simulation. **(B)** First principal strain on the inner core + neurite model. The strain is plotted from the same simulation as in (A). **(C)** Values of strain at the locations indicated in (A).

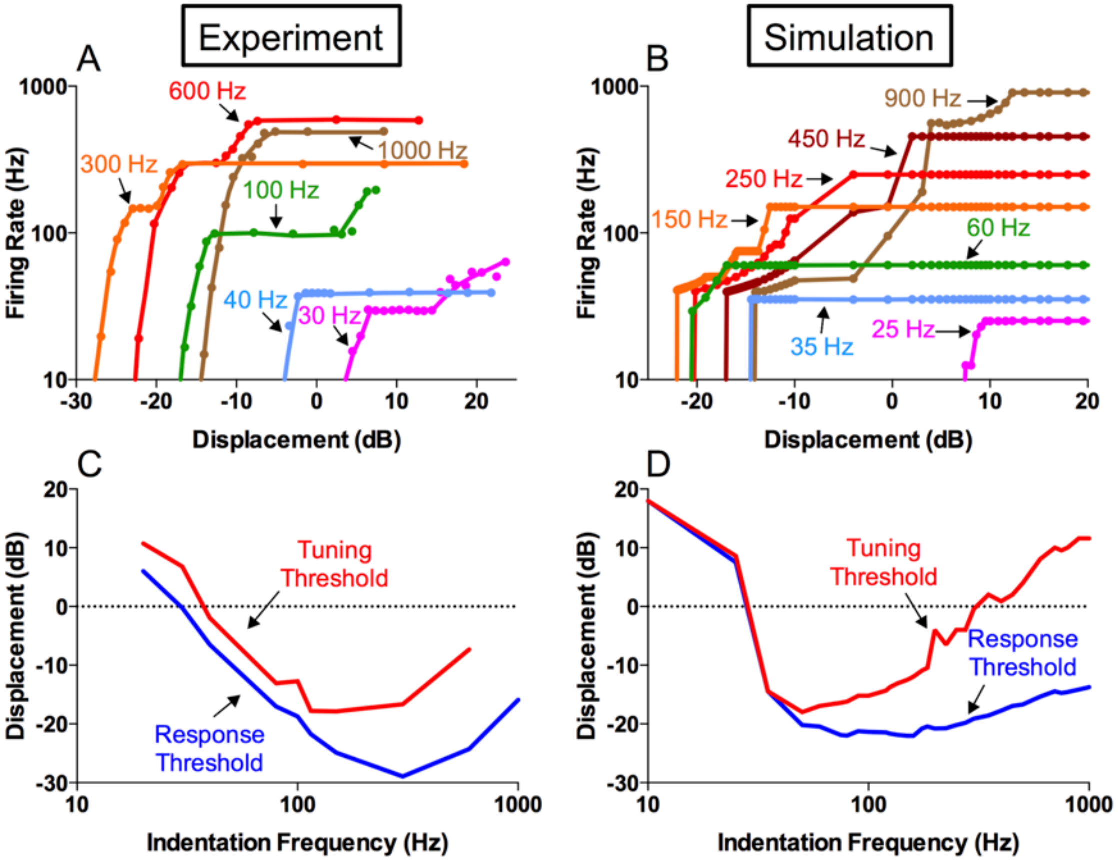

Figure 3.9: Stage 3 frequency sweep results. (A) Experimental [20] and **(B)** simulated neurite firing rates resulting from displacements at various frequencies. The data sets were color-coded so that the peak frequency (Experiment: 300 Hz, Simulation: 150 Hz) is orange. Amplitude is reported as displacement in dB relative to a 1 μm indentation. **(C)** Experimental [20] and **(D)** simulated firing rates obtained from (A) and (B). C and D show the Response Threshold (blue, the displacement at which the firing rate was greater than zero) and the Tuning Threshold (red, the displacement at which the firing rate was equal to the indentation frequency).

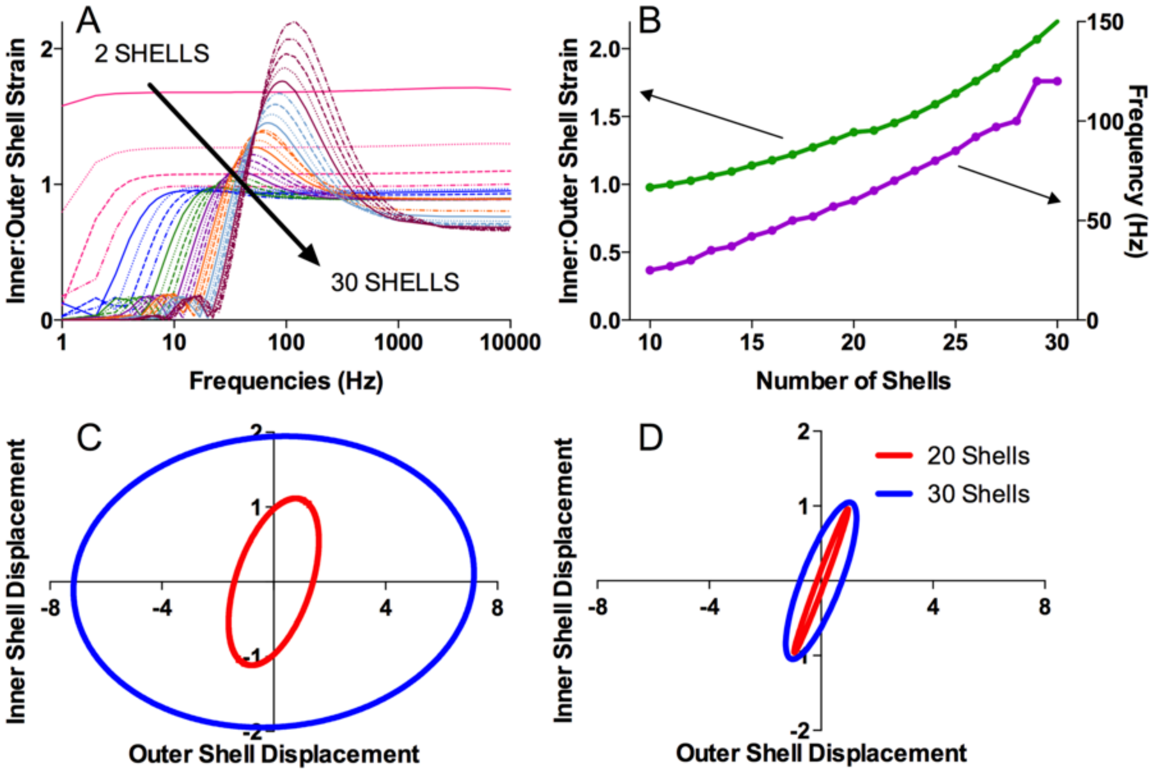

Figure 3.10: Stage 1 size sweep results. (A) Ratio of innermost to outermost maximum radial strain vs. frequency for spheres of 2-30 shells. Strain was calculated as $\Delta r / r_o$ at the innermost and outermost shell, where Δr is the maximum displacement and is r_o the original radius of the shell. **(B)** Peak strain ratio (green) and frequency (purple) at peak strain ratio for spheres of 10-30 shells. **(C-D)** Phase space diagrams of 20 (red) and 30 (blue) shelled spheres during (C) 100 Hz and (D) 1 kHz simulations. Inner and outer shell displacements are reported in arbitrary units.

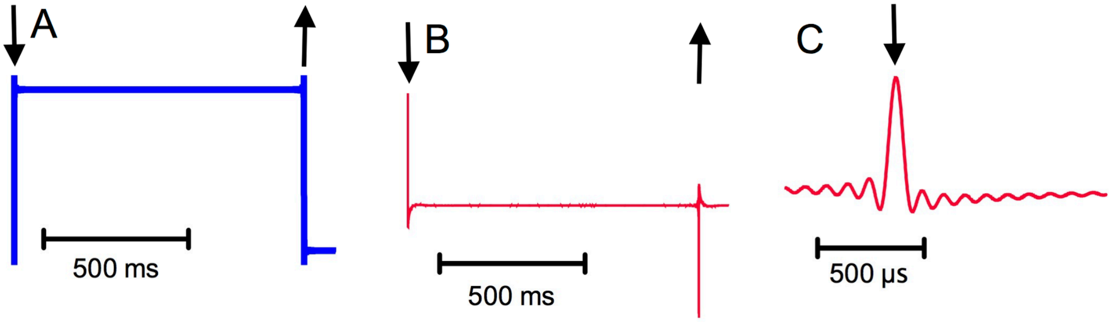

Figure 3.11: Stage 1 square wave indentation results. (A) Outer and **(B)** inner shell displacements in square wave simulations from summation of 0.5-1000.5 Hz simulations. Down and up arrows indicate stimulus onset and offset, respectively. **(C)** Inner displacement zoomed-in on stimulus onset response in (B).

CHAPTER 4: COMPUTATIONAL PARAMETRIC ANALYSIS OF THE MECHANICAL RESPONSE OF STRUCTURALLY VARYING PACINIAN CORPUSCLES

The content of this chapter was previously published as a research article in the *Journal of Biomechanical Engineering* by Quindlen, Schepis, Güçlü, and Barocas [33].

4.1 Summary

In this study, we sought to evaluate the relationship between the PC's material and geometric parameters and its response to vibration. We used a spherical finite-element mechanical model based on shell theory and lubrication theory to model the PC's outer core. Specifically, we analyzed the effect of the following structural properties on the PC's frequency sensitivity: lamellar modulus (E), lamellar thickness (h), fluid viscosity (μ), PC outer radius (R_o), and number of lamellae (N). The frequency of peak strain amplification (henceforth "peak frequency") and frequency range over which strain amplification occurred (henceforth "bandwidth") increased with lamellar modulus or lamellar thickness, and decreased with an increase in fluid viscosity or radius. All five structural parameters were combined into expressions for the relationship between the parameters and peak frequency, $\omega_{peak} = 1.605x10^{-6} N^{3.475} \frac{Eh}{\mu R_o}$, or bandwidth, $B = 1.747x10^{-6} N^{3.951} \frac{Eh}{\mu R_o}$. Although further work is needed to understand how mechanical variability contributes to functional variability in PCs and how factors such as PC eccentricity also affect PC

behavior, this study provides two simple expressions that can be used to predict the impact of structural or material changes with aging or disease on the frequency response of the PC.

4.2 Introduction

The mechanical contributions of (1) the adjacent fluid and lamellar layers and (2) the overall structure of the PC's capsule have been the focus of a number of previous models of the receptor's response to mechanical stimuli, which is discussed in more detail in Section 1.3. In seminal work, Loewenstein and Skalak [23] developed a mechanical model of the PC outer core, in which the capsule was modeled as a series of elastic and viscous cylinders. Holmes and Bell [28,29] modeled the capsule as a two-dimensional cross section of orthotropic shells and fluid layers and coupled the hoop strain of the receptor membrane to a receptor potential model of stretch-gated channels. Srinivasan and co-workers [30–32] later built upon Loewenstein and Skalak's work and adjusted the size and number of lamellae located within the simulated PC capsule. We [24] modeled the mechanics of the PC outer core with alternating spherical layers of elastic shells and fluid-filled spaces and also varied the number of lamellae within the capsule. A non-lamellated finite-element model by Güçlü et al. [109] investigated the contribution of the PC's ellipsoidal shape to its mechanical response under indentation and found that the shape alone could not accurately model the PC's static deformation. A subsequent finite-element model [115] that accounted for the circumferentially-aligned structure of the capsule reproduced the capsular deformation of Güçlü et al.'s [109] experimental data.

The aforementioned models have greatly informed us on how the structural components of the PC's capsule can influence its mechanics, specifically its function as a band-pass filter to vibrational stimuli. Increasing the number of lamellae within the PC outer core widens the pass band of the PC's filtering behavior and increases its ability to amplify mechanical strain through the lamellar layers [24,32]. While the number of lamellae in cat mesenteric PCs has been previously reported as 30 [36], this number can vary with age as the intermediate growth zone cells become incorporated into the inner or outer cores [36]. Specifically, the number of lamellae and the spacing between layers increase during the first two postnatal months in the rat [49], and PCs increase in size with age in humans until age 70, after which they begin to shrink [16]. PC size has also been shown to vary with anatomical location within the human [17] and the monkey [34] hand.

The material properties of the capsule, specifically the elastic modulus of the capsule's lamellae and the viscosity of the fluid components, determine the PC's mechanical behavior. While these parameters, to our knowledge, have not been measured experimentally and reported in an archival document, different values have been estimated from other physiological systems for use in previous models. Values in the kPa range [24,32,109,115], comparable to those of single cells and skin, and the MPa range [23], similar to arterial wall, have been selected as the lamellar elastic moduli, and viscosities ranging from one [157] to ten times that of water [24,32] have been used to model the fluid component of the capsule. Previous theoretical and computational studies have shown that increasing the fluid viscosity shifts the PC's frequency sensitivity to lower frequencies [24]. Thus, the geometric organization of the PC and the material properties of the components that make up its capsule can greatly influence the receptor's mechanical response to vibration, which in turn affects the PC's frequency sensitivity regime.

Evaluating this structure-function relationship is essential to understanding the PC's role in our somatosensory system.

A significant challenge in the use of the models described above, including our own, is that the complex, multiphysical nature of the problem leads to complicated computational models that have long run times. For simulations of a single PC in isolation, the range of possible PC structures, the range of possible PC tissue properties, and the range of possible conditions to be studied collectively place a large demand on any computational model. There are dozens of PCs in a single finger [17], and the PC's large receptive range means that many can be engaged by a single stimulus on the skin surface. If one wishes to explore the behavior of a PC population distributed within the skin and with natural variation in properties, it is valuable if not necessary to have available simplified expressions for the property-dependent response of the PC. Thus, after conducting a broad parametric study, we reduced our variable space by the formation of appropriate dimensionless groups and fit simple expressions for the peak frequency and response bandwidth of a PC in terms of its material and structural properties.

4.3 Methods

The overall objectives of this study were to provide a comprehensive analysis of the PC's mechanical response to vibrations as influenced by the material and geometric properties of the outer core and, if possible, to generate simple expressions for the PC response as a function of these properties. To achieve these objectives, we used a previously-published model [24] of the mechanotransduction process within a single, isolated PC to relate structural factors to mechanical tuning of the PC.

4.3.1 Computational PC model

A three-stage model of the mechano-to-neural transduction process of the PC was previously created [24] and is described in more detail in Chapter 3. Briefly, the model simulates the neural signal that is elicited within the PC neurite in response to a vibratory mechanical stimulus applied to the outer core. The model consists of three separate sub-models applied in series to describe the entire process through which a mechanical input is transduced into an electrical output:

1. The Stage 1 model is a finite-element mechanical model of the PC outer core created in MATLAB (Figure 4.1B). Alternating layers of fluid (modeled as Newtonian via lubrication theory) and lamellae (modeled as linear elastic shells) are coupled to account for the fluid-lamellar interaction in the outer core.
2. The Stage 2 model is a finite-element mechanical model of the PC inner core and neurite created in COMSOL. The deformation of the innermost shell in the Stage 1 model is transferred to the outer boundary of the inner core of the Stage 2 model.
3. The Stage 3 model is an electrochemical model of the neurite created in NEURON. In this model, the opening of stretch-gated cation channels on the neurite's surface is approximated by current injection in the electrochemical neurite model. Strains measured on the neurite's surface in the Stage 2 model are converted into current by a sigmoidal function, and the current is then inserted into the corresponding location in the Stage 3 model. The output of the Stage 3 model is the membrane potential of the neurite resulting from the mechanical input applied to the Stage 1 model.

The three-stage model [24] provides insight into the mechano-neural coupling that occurs within the PC, but each individual stage can also be used independently. The Stage 2 and Stage 3 models were not required to estimate how a surface wave is transmitted into the PC, so only the Stage 1 model was used in the current work.

As mentioned above, the multilayer model of the PC outer core accounts for both the lamellar layers and the fluid-filled spaces within the capsule. This model can therefore account for the fluid-solid interaction as mechanical vibrations are transmitted through the outer core. The PC was modeled as symmetric about the pole-to-neurite axis (in/out of the page in Figure 4.1) and symmetric about a plane orthogonal to that axis and passing through the neurite. The model contained an incompressible, inviscid fluid core at the center, which was surrounded by alternating layers of elastic shells and lubricating fluid. The mechanics of the lamellae were modeled with the equations of equilibrium for spherical shells [142], and the fluid behavior was modeled using lubrication theory (details in [24]). The thickness of each lamella was initially set at increasing values between 0.1 and 0.4 μm using a Weibull function [32]. The individual lamellar thicknesses always increased with distance from the inner core in the parameter sweeps ran in this study.

The multilayer model was run at various parameter values (Table 4.1) to examine the relationship between the PC's structure and mechanical response. Only material and geometric parameters in the PC's outer core were adjusted. Varying inner core and neurite parameters would also affect the PC's physiological response to vibrations, but doing so was deemed outside the scope of the current study.

Two features of the resulting mechanical simulations were analyzed to describe the response of the PC to the vibrational stimuli: (1) **peak frequency**, defined as the frequency at which the ratio of inner shell strain (radial displacement divided by initial radius) to outer shell strain was highest, and (2) **bandwidth**, defined as the frequency range for which the ratio of inner to outer shell strain was greater than 1 (indicating strain amplification through the PC capsule).

Based on the Buckingham Pi theorem, for six model parameters (modulus E, viscosity μ, lamellar thickness h[†], PC outer radius R_o, number N of lamellae, and stimulus frequency ω or bandwidth B) and three dimensions of interest (force, length, and time), there should be three independent dimensionless groups. The number of lamellae, being dimensionless, is trivially one group, and the obvious other two groups are a Deborah number (μω/E, μB/E) and an aspect ratio (h/R_o). Thus, we attempted to characterize the peak frequency and bandwidth as a function of the other parameters of the forms

$$\omega_{peak} \sim \left(\frac{E}{\mu}\right)\left(\frac{h}{R_o}\right)^{\alpha} f(N) \tag{4.1}$$

$$B \sim \left(\frac{E}{\mu}\right)\left(\frac{h}{R_o}\right)^{\beta} g(N) \tag{4.2}$$

where the exponents α and β and the functions f and g were not known a priori.

4.3.2 Lamellar modulus sweep

Because similar results were obtained for the same values of E/μ in our initial calculations regardless of whether μ or E was adjusted, E was varied from 1 mPa to 1GPa

---

[†] In this work, we use the term "lamellar thickness" to refer to the thickness of a solid lamella. One could use other terms and variables, such as the lamellar spacing (i.e. the thickness of the fluid layer between adjacent lamellae), but we chose to use lamellar thickness defined to be the thickness of the solid component. Lamellar spacing is not included in the variable list because it can be expressed in terms of the lamellar thickness, number of lamellae, and PC radius, so it is not an independent variable in our treatment of the problem.

in subsequent simulations and μ was held constant at 1.4 mPa-s (Table 4.1). The number of lamellae was varied between 2 and 30. For these simulations, the individual lamellar thicknesses were between 0.1 (innermost lamella) and 0.4 μm (outermost lamella), as stated previously, and the PC outer radius ranged from 23.5 μm (2 shell case) to 255.6 μm (30 shell case).

4.3.3 Thickness and radius sweep

The geometric parameters h and R_o were also varied in separate simulations (Table 4.1). The number of lamellae was varied again between 2 and 30. As in the modulus sweep, the initial thicknesses of the lamellae were set between 0.1 and 0.4 μm, with thickness increasing with distance from the core. The set of lamellar thicknesses was multiplied by a single multiplier (φ) that varied from 0.02 to 8, resulting in minimum and maximum average lamellar thicknesses of 2.2 nm (12 layers, φ=0.02) and 1.47 μm (30 layers, φ=8). The outer PC radius was also varied. To do so, the initial radius of each lamellar layer within the PC was multiplied by a single radius multiplier (λ). The PC radius multiplier was varied from λ=0.5 (outer radius of 26.05 μm in the 12 shell case) to λ=10 (outer radius of 2.56 mm in the 30 shell case). For these simulations, E was set at 1 kPa and μ to 1.4 mPa-s.

4.4 Results

4.4.1 Computational model results

The multilayer model was run at the structural parameter values listed in Table 4.1. The specific studies are described in turn in the subsequent paragraphs.

4.4.2 Lamellar modulus sweep

The resulting ratios of inner to outer shell strain for PCs with 2-30 shells are plotted in Figure 4.2 for lamellar modulus (E) values of 100 Pa, 1 kPa, and 10 kPa. A 10-fold increase in E resulted in a 10-fold increase in peak frequency. The peak frequency and bandwidth (Figure 4.3A) at various ratios of lamellar modulus to fluid viscosity (E/μ) and numbers of shells (N) were calculated for 12-30 shells (Figures 4.3B and 4.3C).

4.4.3 Thickness and radius sweep

The peak frequencies measured for simulations in which lamellar thickness (Figure 4.4A) and radius (Figure 4.4B) were varied was calculated for 12-30 shells. In general, as the average lamellar thickness (h) increased, or as more of the capsule became solid, the peak frequency also increased. As the outer radius (R_o) increased, or as more of the capsule became fluid, the peak frequency decreased. Two example PCs run in the lamellar thickness sweep, shown in Figures 4.4C and 4.4D, demonstrate how the different model parameters interact. The structures are very different – the PC in Figure 4.4C is smaller and has fewer, thicker lamellar layers – but they produce roughly the same peak frequency. Thickening the layers tends to make elastic effects more important relative to viscous effects, shifting to higher peak frequencies, as seen by the positive slope of the lines in Figure 4.4A (a similar effect is seen for increasing modulus in Figure 4.3B, and the opposite effect is seen when increasing PC radius, Figure 4.4B, which increases viscous effects by increasing interlamellar spacing). This tendency to shift towards higher frequencies is countered, however, by a tendency to decrease the peak frequency as the number of shells decreases, an effect attributable to an increase in lamellar spacing as the number of shells decreases and/or to more elastic-like behavior for many narrowly-spaced layers. The net result of these two competing effects is that a PC comprising a few thick, tightly-spaced layers (Figure 4.4C) can have the same peak frequency as a larger PC comprising many thinner, more widely spaced lamellae (Figure 4.4D).

As expected from the scaling analysis, the curves collapsed when plotted vs. h/R_o (Figure 4.5). As h/R_o increased, the peak frequency and bandwidth both increased, and adding more shells to the model predicted that both response properties would increase for a given h/R_o value.

4.4.4 Eh/μR₀ analysis

Lamellar modulus, lamellar thickness, fluid viscosity, and PC radius were considered together in the single ratio $Eh/\mu R_o$ as suggested by the scaling analysis and the linear relationships in Figure 4.5. The peak frequency (Figure 4.6A) and bandwidth (Figure 4.6B) resulting from simulations run at different values of $Eh/\mu R_o$ for 12-30 shells were calculated. When the value $Eh/\mu R_o$ was analyzed, the results for E/μ and h/R_o collapsed onto each other, indicating that the ratio $Eh/\mu R_o$ was driving the overall behavior of the simulated PCs.

Finally, the peak frequency and bandwidth were expressed in terms of both N and $Eh/\mu R_o$. Equation 4.1 was fit to the data collected from all simulations, and the following equation for peak frequency was obtained with an R-squared value of 0.961 (Figure 4.7A, reorganized in Figure 4.7B):

$$\omega_{peak} = 1.605x10^{-6} N^{3.475} \frac{Eh}{\mu R_o} \tag{4.3}$$

Equation 4.2 was fit to the bandwidth data collected from all simulations, and the following equation for bandwidth was obtained with an R-squared value of 0.9466 (Figure 4.7C, reorganized in Figure 4.7D):

$$B = 1.747x10^{-6} N^{3.951} \frac{Eh}{\mu R_o} \tag{4.4}$$

It is important to note that all simulation data obtained in this study appear in Figure 4.7 and follow the relationships in Equations 4.3-4.4. Thus, given the lamellar modulus, lamellar thickness, fluid viscosity, outer radius, and number of shells within a PC, one can calculate its peak frequency or bandwidth using a single equation rather than running the full simulation.

4.5 Discussion

In this work, we investigated how the structural properties of the PC affect its frequency sensitivity in a computational model. We used a mechanical model of the PC capsule to predict how various material (lamellar elastic modulus, fluid viscosity) and geometric (number of shells, outer radius, lamellar thickness) parameters affect strain amplification through the lamellar layers of the PC capsule.

Aging and disease can affect many different aspects of the central [158] and peripheral [159] nervous systems that may impact vibrotactile sensitivity, but due to the focus of this study only those changes associated with the structure of the PC are discussed in the subsequent paragraphs. Previous structural studies [89] found that, with age, the human PC increases in size by the addition of lamellae until it eventually becomes distorted in structure, which is followed by a decrease in the number of PCs within the skin. While these anatomical and morphological changes in the receptor due to aging have been reported in the PC literature, the mechanical and functional responses of isolated aged PCs have not been probed. Previous studies have, however, investigated the vibration sensitivity changes that occur within the hand with age. Vibrotactile detection experiments by Verrillo [90] performed on subjects of various ages found that vibrotactile thresholds in the hand at higher frequencies (i.e., within the typical PC sensitivity range) increase with age. Specifically, Verrillo's experiments showed that while the peak frequency was not shifted, the sensitivity threshold at that frequency increased. While Verrillo does not report a shift in peak frequency with age, his threshold measurements were only obtained at 11 frequencies spanning 25-700 Hz, and it is unknown whether a shift would have been observed if more frequencies were studied. It is also important to note that the vibrotactile thresholds reported by Verrillo likely represent the activity of more than one type of mechanoreceptor, so we must be wary of drawing direct comparisons between these data and the results of our single PC model. A number of other experimental studies have investigated changes in vibrotactile sensitivity with age in various anatomical locations such as the foot [160,161], ankle [162], wrists [96], and knees [96]. In those studies, only vibrotactile threshold and not peak frequency was measured and too few measurements were taken to determine whether or not a shift in peak frequency occurred with age. Verrillo proposed that the experimentally-observed increase in vibrotactile threshold may be due to a decrease in the number of PCs within the skin but added that the density of PCs could not explain this phenomenon alone. Verrillo therefore proposed that geometric changes, such as those reported by Cauna [89] (i.e., addition of lamellae, shape distortion) may be a mechanism for the decreased vibrotactile sensitivity in the Pacinian frequency range with age. While the current study analyzed the peak frequency and not vibrotactile thresholds, we did see that increasing the number of lamellae (Figure 4.2) not only shifted the peak frequency to higher frequencies but also increased strain amplification at the peak frequency, which would directly affect the threshold. Increasing the number of shells in our simulations increased strain amplification, which would cause a decrease in threshold amplitude, so the addition of new lamellae alone cannot explain the experimentally-observed increase in threshold. Shape distortion, which cannot be explored by a spherical model, may also play a role by affecting the interlamellar spacing in the capsule, or there may be mechanical changes in the lamellae with age.

Vibrotactile sensitivity can also be affected by disease, such as diabetes. Peripheral neuropathy is a common complication of diabetes and can affect the sensation of vibration, among other sensory modalities and neural functions [91]. Diabetic skin biopsies [92] have shown denervation and neuronal structural changes, which can affect the cutaneous mechanoreceptors [93]. In diabetic monkeys, the PC capsule can undergo structural changes including irregular spacing between lamellae, thickening of outer lamellae, and a breakdown of inner lamellae, causing the capsule to appear deteriorated [94]. Thickening of lamellae would cause the peak frequency to increase proportionally, according to Equation 4.3. Irregular spacing between lamellae would also affect the peak frequency, as the amount of the capsule that is fluid or solid affects the frequency response (Figures 4.4A and 4.4B). Functionally, PCs are shown to be implicated in diabetic neuropathy as vibrotactile thresholds increase in patients with diabetes, showing a decrease in sensitivity to vibration [92,95,96]. Advanced glycation as a result of diabetes leads to many complications associated with the disease, as advanced glycation end products can induce cross-linking of proteins such as collagen and cause increased vascular stiffness [97–99].

The vasculature of the PC capsule [100] may be stiffened as a result of diabetes, or the adventitial tissue of the PC's end organ may also become stiff, as glycation has been shown to affect not only the stiffness of vascular tissue but also that of tissues such as cartilage [101], tendon [102], and other connective tissues (i.e., plantar tissue [103]). If such stiffening were to occur within the PC capsule in the form of increased lamellar modulus (E), the peak frequency would be expected to increase proportionally with E (Equation 4.3), and the bandwidth would also increase (Equation 4.4). If increased stiffness due to glycation causes the peak frequency of the PC to shift to frequencies higher than the maximum firing rate allowed in the afferent nerve due to its refractory period, then this could result in the inability of the nerve to fire at the frequency of vibration. Vascular stiffening can also result from aging [99], so the conclusions pertaining to PC stiffening could also apply to vibrotactile sensation changes that occur with aging. The results of the current study suggest that structural changes resulting from the diabetes or other diseases could contribute to the observed functional changes seen in patients.

PC structure can also be affected by denervation and reinnervation, which have been studied in the rat [163]. In early postnatal rats, denervation results in rapid PC regeneration [164]. In adult rats, however, mature PCs survive denervation and can be reinnervated with new axon terminals [163,165]. The inner core diameter can be reduced following denervation in adult rats [165]. Reinnervation of these PCs can lead to unusual structural development. Reinnervated mature rat PCs can contain several axon terminals enclosed by multiple inner cores within a single outer core [166,167]. The mechanical and functional changes resulting from the altered structures of denervated and reinnervated PCs can also be analyzed with the model used in the current study.

A number of experiments [10,11,20,21,51] and models [23,24,30–32] have demonstrated that the lamellae of the PC capsule collectively act as a mechanical filter and allow the dynamic portions of a mechanical vibration to reach the neurite. Bell and Holmes [29] previously created a theoretical model of the PC in which a mechanical model [28] of the capsule was coupled to a model of the receptor potential via the hoop strain on the receptor membrane. The model predicted tuning curves in response to sinusoidal pressure inputs for intact PCs similar to those recorded experimentally [20]. When the modeled PC was decapsulated, the shape of the predicted tuning curves remained unchanged, suggesting that the capsule did not play a role in the filtering response in their model. While it is possible that mechanical filtration by the capsule may not be the only factor involved in the PC's response to vibration, as hypothesized previously by Bolanowski [168], our study suggests that the capsule and its structural properties play a major rule in determining the frequency response of the PC. The contrast in the importance of the capsule between Bell and Holmes' model [29] and the current model is likely a result of the different modeling approaches taken in the two studies. Rather than treating the collagen layers as individual shells, Bell and Holmes treated them as membranes (i.e., they ignored bending stiffness) and used homogenization theory to derive continuous equations for their model. Bell's argument for using membrane theory is that the lamellae are thin, but since the displacements are also very small, we do not consider bending stresses negligible compared to stretching stresses.

When stimulated with a sustained pressure stimulus, the PC fires action potentials only during the on and off portions of the stimulus (dynamic portions) and not during the static portion [50], which classifies the PC as a rapidly adapting mechanoreceptor. It was first believed that the PC's rapid adaptation was purely due to the mechanical properties of the capsule [10,23]. Pawson et al. [27], however, later attributed the rapid adaptation to a mechanochemical, rather than a purely mechanical, response of the PC to sustained pressure. Their experiments suggest that γ-aminobutyric acid (GABA) released from PC lamellae inhibits the glutamatergic excitation (originating from the neurite or PC capsule) that is responsible for sustained pressure action potentials. This GABAergic inhibition thus leads to the characteristic absence of action potentials during the static portion of a sustained stimulus seen in the rapidly adapting PC. The lamellar cells therefore play both a mechanical and chemical role in the rapid adaption of the PC, as they release GABA and potentially glutamate to modulate the response. It has been hypothesized that the neural response of PCs to dynamic mechanical stimuli, such as a high-frequency vibration, is a result of mechanical transmission of the stimuli through the PC capsule which causes stretch-gated cation channels on the PC neurite to open and initiate action potentials, and a recent modeling study by our group was able to simulate experimental neural firing using this hypothesis [24]. It is unclear, however, whether the filtering function of the PC in the case of high-frequency vibration is solely mechanical, or if there is also a mechanochemical role of lamellae. While the current study considers the lamellae to play a purely mechanical role in the PC's response to vibration, there could also be electrochemical modulation by the lamellar cells that affects the frequency tuning of PCs. Tuning curves were collected in the study by Pawson et al. described above [27] in response to sinusoidal displacements in the 10-400 Hz frequency range in the presence and absence of the pharmacological agents (GABA; GABA receptor antagonists, gabazine and picrotoxin; glutamate receptor antagonist, kynurenate) used in the sustained indentation experiments. There was no significant difference in the sensitivity of the PC's frequency response with the addition of the pharmacological agents, as all but one tuning curve did not change in the presence of the drugs. These results suggest that if the PC's response to dynamic stimuli does involve mechanochemical mechanisms, then they are different from those involved in the response to sustained stimuli.

The current study, which addresses how structural variability of the PC capsule may lead to mechanical variability, could be combined with an electrochemical model [24] of the PC neurite to elucidate how mechanical variability leads to functional variability. While a model such as the one presented here, combined with an electrochemical neurite model, could inform us of the relationship between structural, mechanical, and functional variability of the PC, this information also needs to be obtained *in vivo*. Previous studies have addressed the structural [34,65,78], mechanical [10], and functional [20,21] variability of PCs, yet no study has obtained all three measurements on the same sample. Unpublished experimental wave penetration data for cat mesenteric PCs show a substantial degree of mechanical variability in the receptor's response to different vibration frequencies, but the structural parameters of the tested PCs were not recorded. The current study provides a mechanistic explanation for how structural variability can lead to the observed mechanical variability in the unpublished experiments. To our knowledge, no experimental study has been able to measure directly the correlation between structural and mechanical variability in the PC. The computer simulations performed in this study provide a first glimpse into the relationship between these two facets of PC variability, but future vibration experiments on isolated PCs are necessary to validate the results of these simulations.

Functional variability of PCs may be extremely valuable in allowing mammals to experience a wide range of vibrotactile sensations. PC structural variability can enable more nuanced encoding of vibrations by providing different frequency sensitivities. For example, by having multiple PCs within a cluster that are tuned to different frequencies, one could better distinguish subtle differences in stimulus than one could with a single PC or a cluster of identical PCs. The current study suggests that slight differences in structural variability (e.g., the addition of one lamellar layer) may greatly affect the mechanical (and thus functional) variability of a single PC. By understanding how structural, mechanical, and functional variability interact, we can begin to understand how the somatosensory system is optimized to process the complex vibrotactile stimuli ubiquitous in our physical world.

Table 4.1: Structural parameters used in model simulations. Step sizes were scaled to the values, with 20 modulus steps per decade, and extra steps were added when necessary for resolution purposes.

Parameter	**Parameter Range**	**Number of Parameter Values Studied**	**Relevant References**
Number of lamellae (N)	2-30	29	[36]
Lamellar modulus (E)	1 mPa-1 GPa	261	[23,24,32,109,115]
Viscosity (μ)	1.4 mPa-s	1	[24,32]
Lamellae thickness (h)	2.20 nm-1.47 μm	67	[32,36]
Outer radius (R_o)	26.05 μm-2.56 mm	191	[35]

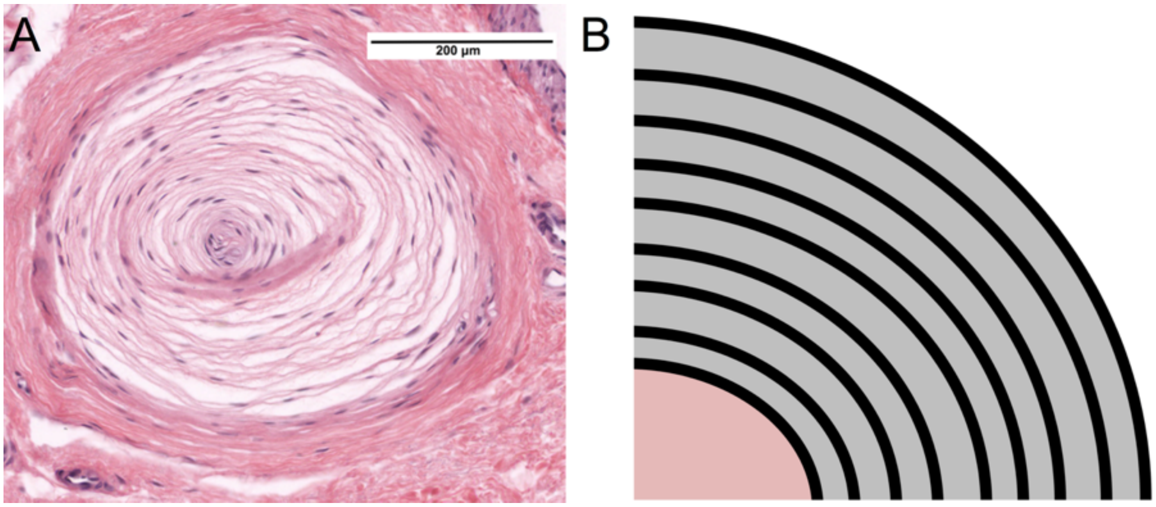

Figure 4.1: Histological and model PCs. (A) Image of a single PC in a thick human skin slice. Image obtained from thick human skin after H&E staining and provided by Dr. Christopher Honda from the University of Minnesota. The PC was sectioned perpendicular to the long axis of the receptor. Lamellae can be seen as concentric pink lines in the cross section. **(B)** Representation of the PC outer core in the multilayer (Stage 1) model. The solid black lines represent lamellae and the shaded grey regions represent the interlamellar fluid. The pink area represents the inner core (modeled in Stage 2).

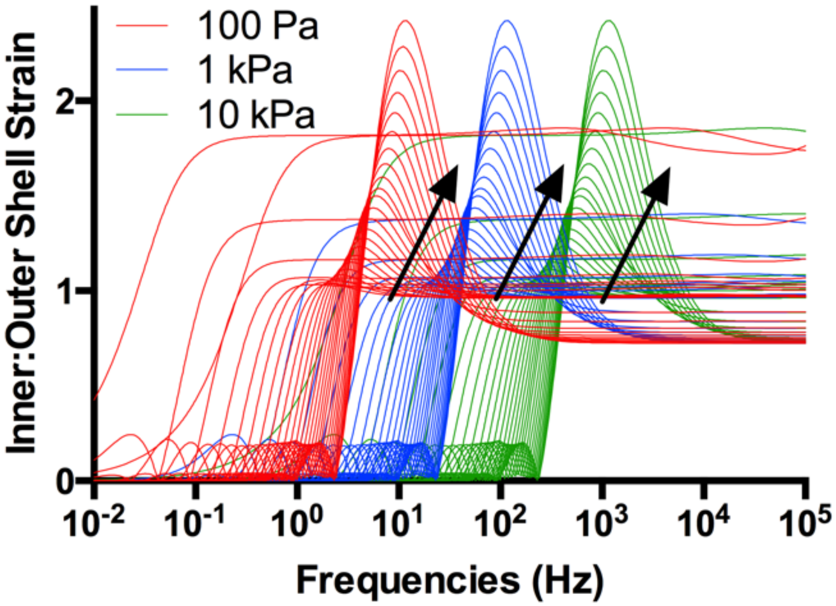

Figure 4.2: Ratio of inner to outer shell strain at various lamellar moduli. The ratio is plotted for simulations run with lamellar moduli of 100 Pa (red), 1 kPa (blue), and 10 kPa (green). Each modulus was run for PCs with 2-30 shells, with increasing shell number indicated by the black arrows.

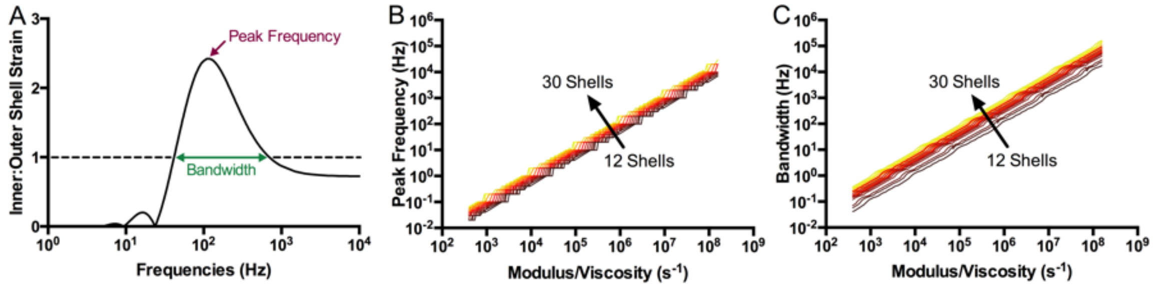

Figure 4.3: Peak frequency and bandwidth for various ratios of lamellar modulus to fluid viscosity (E/μ). (A) The peak frequency was the frequency at which the highest ratio of inner to outer shell strain occurred, which is the frequency of peak strain amplification. The bandwidth was the frequency range over which the ratio of inner to outer shell strain was greater than 1 (dashed line), indicating strain amplification through the PC capsule. **(B)** The peak frequency was calculated for different values of E/μ. The peak frequency at E/μ is plotted for 12-30 shells, with increasing shell number indicated by the arrow and hotter color. **(C)** The bandwidth was calculated for different values of E/μ, with increasing shell number indicated by the arrow and hotter color.

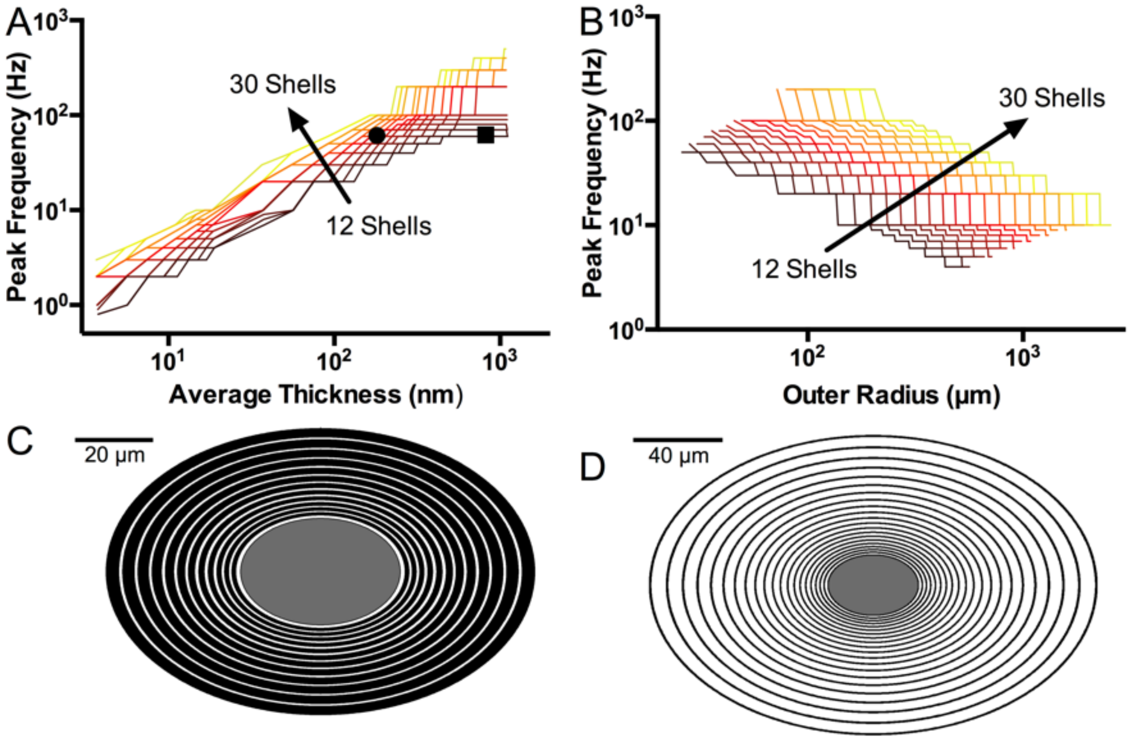

Figure 4.4: Peak frequency plotted for various average lamellar thicknesses (h) and radii (R_o). (A) The peak frequency was calculated for simulations run at different values of h with 12-30 shells. The square and circle icons represent where the PCs shown in (C) and (D) would fall on this graph. Increasing shell number is indicated by the arrow and hotter color. **(B)** The peak frequency was calculated for simulations run at various R_o. **(C)** 12 shell PC run at parameters indicated by the filled square in (A). Black indicates solid lamellae, white indicates fluid-filled spaces, and grey indicates the inner core. **(D)** 20 shell PC run at parameters indicated by the filled circle in (A).

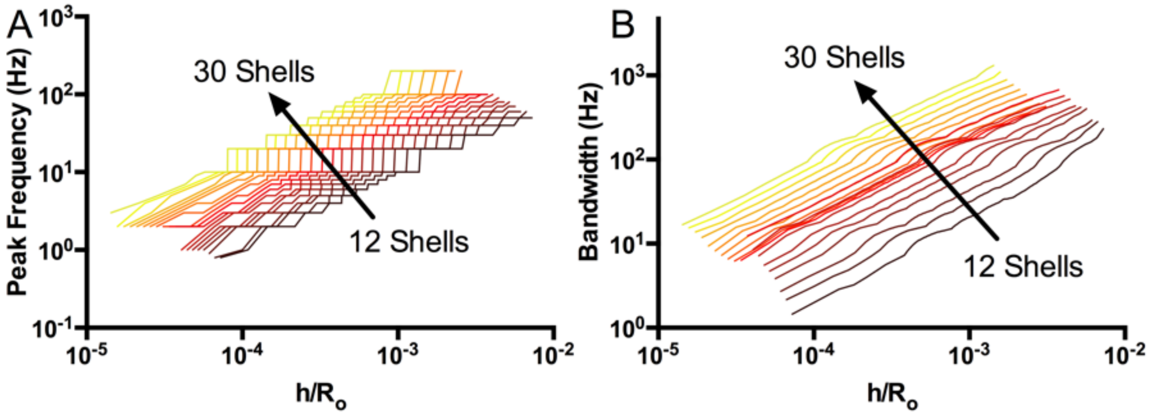

Figure 4.5: Peak frequency and bandwidth vs. h/R$_o$. (A) Peak frequency calculated for various values of h/R$_o$ at 12-30 shells with increasing shell number indicated by the arrow and hotter color. **(B)** Bandwidth calculated for various values of h/R$_o$ at 12-30 shells with increasing shell number indicated by the arrow and hotter color.

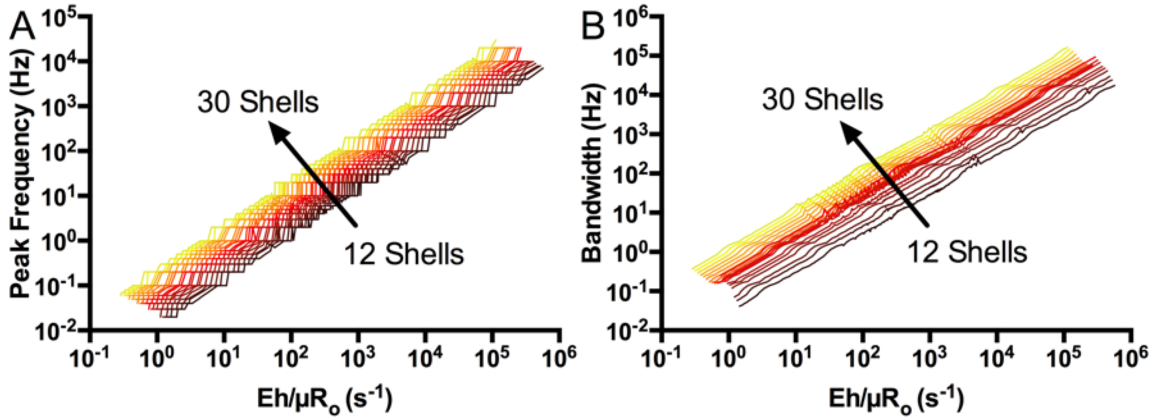

Figure 4.6: Peak frequency and bandwidth vs. Eh/μR$_o$. (A) Peak frequency calculated from simulations run at various values of Eh/μR$_o$ for 12-30 shells, with increasing shell number indicated by the arrow and hotter color. **(B)** Bandwidth calculated from simulations run at various values of Eh/μR$_o$, with increasing shell number indicated by the arrow and hotter color.

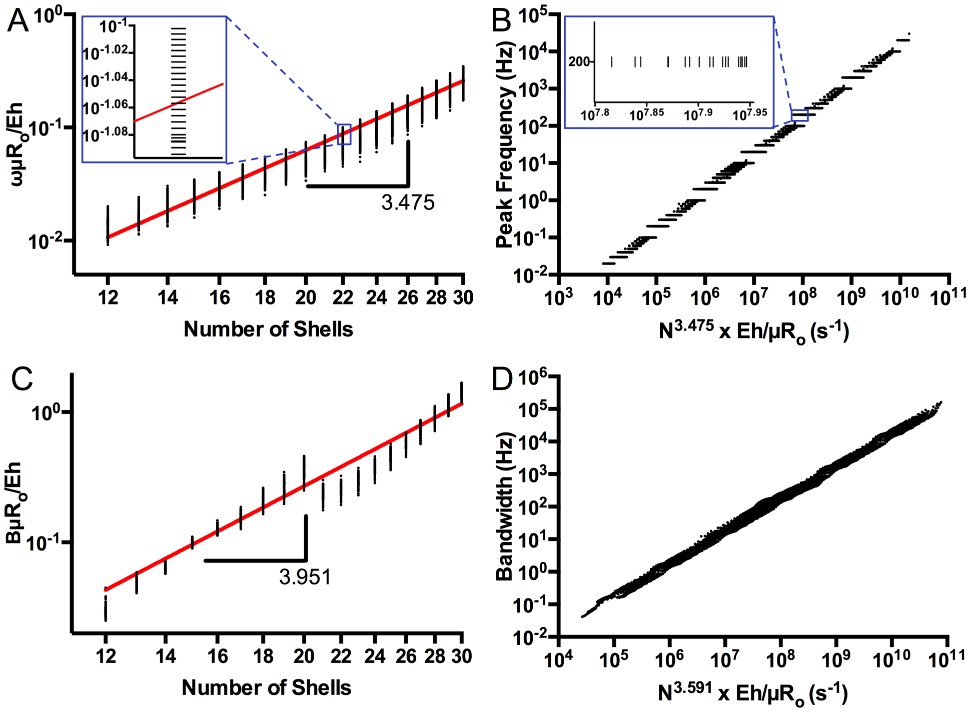

Figure 4.7: Relationship between the five structural parameters (E, h, μ, R_o, N) and the peak frequency (ω) and bandwidth (B). **(A)** The value $\omega\mu R_o/Eh$ was plotted against the number of shells (N) in a log-log plot for all data points from the simulations. A power-law fit gave an exponent of 3.475, with the best-fit line shown in red. A zoomed-in view of individual data points is shown. Each simulation is marked with a horizontal line in the zoomed-in view. **(B)** Comparison between the peak frequency measured in all computer simulations and the calculated value $N^{3.475}$ x $Eh/\mu R_o$ using the parameters input into the simulations. A zoomed-in view of individual data points is shown. Each simulation is marked with a vertical line in the zoomed-in view. **(C)** The value $B\mu R_o/Eh$ was plotted against N in a log-log plot for all data points from the simulations. A power-law fit gave an exponent of 3.591, with the best-fit line shown in red. **(D)** Comparison between the bandwidth measured in all computer simulations and the calculated value $N^{3.591}$ x $Eh/\mu R_o$ using the parameters input into the simulations.

CHAPTER 5: A FINITE-ELEMENT MODEL OF MECHANOSENSATION BY A PACINIAN CORPUSCLE CLUSTER IN HUMAN SKIN

The content of this chapter has been submitted as a research article to the journal *Biomechanics and Modeling in Mechanobiology* (Quindlen and Barocas) and is in review.

5.1 Summary

The goal of this study was to model a cluster of PCs to observe the effect PC distances from the indenter and each other on the cluster's mechanical and neural responses to a vibrating stimulus. I developed a finite-element mechanical model of one or two PCs embedded within human skin, coupled to a multiphysics PC model to simulate action potentials elicited by each PC. A vibration was applied to the skin surface, and the resulting mechanical signal was analyzed using two metrics: the deformation amplitude ratio ($\mathrm{\rho}_{1S}$, $\mathrm{\rho}_{2S}$) and the phase shift of the vibration ($\delta_{S1}^{\mathrm{mech}}$, $\delta_{S2}^{\mathrm{mech}}$) between the stimulus and the PC. The results showed that the amplitude attenuation and phase shift at a PC increased with distance from the stimulus to the PC. Differences in amplitude (ρ_{12}) and phase shift ($\delta_{12}^{\mathrm{mech}}$) between the two PCs in simulated clusters directly affected the interspike interval between the action potentials elicited by each PC ($\delta_{12}^{\mathrm{spike}}$). While $\delta_{12}^{\mathrm{mech}}$ had a linear relationship with $\delta_{12}^{\mathrm{spike}}$, ρ_{12}'s effect on $\delta_{12}^{\mathrm{spike}}$ was greater for lower values of ρ_{12}. In the simulations,

the separation between PCs and the distance of each PC from the stimulus location resulted in differences in amplitude and phase shift at each PC that caused $\delta_{12}^{\mathrm{spike}}$ to vary with PC location. The results of this study suggest that PCs within a cluster receive different mechanical stimuli which may enhance source localization of vibrotactile stimuli, drawing parallels to sound localization in binaural hearing.

5.2 Introduction

While mechanical and mechanoneural models have offered great insight into the behavior of a single, isolated PC and can simulate neurophysiological data obtained in an isolated recording procedure [20], there is much to be done in order to understand how the PC functions *in vivo*. The PC is found embedded deep within the skin and subcutaneous tissues [17,34,54–56] and in other anatomical regions such as ligaments [57–59], joint capsules [60–62], muscles [63,64], and internal organs [25,36,65–67]. Therefore, although a model of a single PC can inform us of its dynamics in response to vibrations applied directly to the receptor, it cannot account for the effects of its anatomical location or the mechanical contributions of the surrounding tissues (possibly including other PCs).

PCs are also often observed in clusters of multiple receptors (Figure 1.2), a phenomenon conserved across species. PC clusters have been identified in the human hand [17,75]; the monkey hand [34,55]; cat foot [46,54,76], ankle joint [77] and knee joint [61]; the rat ankle joint [49]; the elephant foot [78]; the raccoon forepaw [79]; and the interosseous region of the kangaroo leg [80]. The number of PCs found within a cluster varies between species, with clusters of 2-3 PCs in the human [81], 2-5 in the monkey [34,55], 3-4 on average in the elephant [78], and 2-11 in the cat [46,54,61,76,77].

PCs within a cluster can have overlapping or neighboring receptive fields [81], enabling them to respond to the same skin stimulus. However, the distance between each PC and the stimulus, based on the distribution of the PCs within the cluster with respect to the skin surface, could affect the response of each PC to the vibration. Spike latencies across a cluster may play a role in source localization of the stimulus, perhaps via a process that parallels sound localization by the auditory system [169]. The asymmetrical shape of the PC [16] suggests that random orientation within a cluster [17] would cause each PC to respond differently to a mechanical stimulus. In addition, it has been shown theoretically that the size and inner structure of PCs can alter their filtering response to vibrations [33]. Therefore, the location, orientation, and size of PCs within a cluster could produce more nuanced tactile encoding of a vibrational stimulus.

The goal of this study was to explore the mechanoneural behavior of one or two PCs embedded within human skin in response to tactile vibrations *in vivo*. After creating a finite-element model of human skin containing PC models, we investigated the effects of (1) separation distance between two PCs in a simulated cluster and (2) the location of these PCs with respect to a skin stimulus. Mechanical amplitude attenuation and phase shift in waves that reached each PC within a cluster, as well as the phase shifts between resulting spike trains for the clustered receptors, were analyzed.

5.3 Methods

5.3.1 Modeling scheme

5.3.1.2 Homogeneous viscoelastic PC model

The highly-detailed inner core model described in Chapters 3-4 [24,33] is valuable for analyzing PC response, but it is also computationally demanding and poorly suited for incorporation into a larger finite-element model. For the current study, I developed a finite-element model of two PCs embedded within human skin in COMSOL. As a first step (Figure 5.1A), I created a homogenized viscoelastic (VE) model in COMSOL to match the mechanical behavior of the Stage 1 model (henceforth “shell model”) described in Chapters 3-4. By embedding a VE equivalent of the shell model into skin, I could obtain the mechanical deformations that would reach an embedded PC in response to skin surface vibrations and then run the three-stage model with the proper inputs to simulate the PC’s neural response to the surface stimulation.

The isolated shell model was run at frequencies spanning 10-10,000 Hz at the same pressure amplitude profile (200 Pa at PC top) for each case. Because the small displacements (~μm) allow linear mechanical models to be used, the specific choice of pressure was arbitrary. The shell model was run for a PC containing 30 lamellae with a modulus of 3 kPa, an interlamellar fluid viscosity of 1.4 mPa-s, and an outer radius of 255.6 μm [23,24,116]. The maximum outer shell displacement at each indentation frequency was recorded. A homogeneous VE model of a spherical PC was created in COMSOL to match the displacement profile obtained from the shell model. The best-fit PC model was a Standard Linear Solid with the parameters E_1 = 3 kPa, E_2 = 500 kPa, and η = 5.5 Pa-s, implemented using the long-term static stiffness option in COMSOL. The displacement and phase shift profiles of the shell and VE PC models are shown in Figure 5.1B-C.

5.3.1.2 Cluster model

Clusters were simulated by embedding VE spherical PCs in a domain representing the skin (Figure 5.2). The skin and bone mesh was separated into three main domains: Outer Skin (OS), Inner Skin (IS), and Bone (B). Skin and bone were modeled using structural and mechanical parameters for human tissue published in the literature, as listed in Table 5.1. Rayleigh damping was introduced into the tissue domains based on a published model of finger mechanics [170]. The entire structure was meshed with 10,967 tetrahedral elements. The outer skin was vibrated at 150 Hz with a simulated indenter of radius 200 μm. The displacement amplitude was set to 30 μm, well above the threshold reported for PCs firing in response to skin surface stimulation at this frequency [2,70].

Once the skin-scale simulation was completed, the displacement amplitude and the phase shift from the applied pressure wave were obtained for each PC, and used as inputs to the three-stage PC model. Spike trains were calculated for each PC based on its individual mechanical deformation. The spike trains for each PC were added together to simulate the spike train that would be recorded from a cluster of the two PCs since the activity of a nerve bundle [171] or PC cluster [81] has been shown to be the sum of the activities of each individual nerve fiber or PC, respectively.

5.3.2 Case studies

5.3.2.1 Center-to-center separation of PCs

The effect of separation distance between two PCs in an idealized cluster was analyzed. PCs were embedded in the inner skin and arranged either vertically (Figure 5.2A) or horizontally (Figure 5.2B) to analyze the effect of separation distance between the PCs on their relative mechanical and neural responses. In the vertically-arranged case (Figure 5.2A), the center of the superficial PC was located 1 mm beneath the skin surface. The center of the deep PC was initially located 511.2 μm (one PC diameter) beneath the center of the superficial PC. The surface of the skin directly over the PCs was indented, and the resulting spike train from the cluster was obtained. The separation between the two PCs

(L_{12}) was increased in subsequent simulations, as the center of the deep PC was moved in the negative y direction (away from the skin surface) until a maximum separation of 1200 μm was obtained.

In the horizontally-arranged case (Figure 5.2B), the centers of both PCs were located 1mm beneath the skin surface. The central PC was located under the indenter and the separation between the two PCs (L_{12}) was increased from 511.2 to 1200 μm as the lateral PC moved in the positive x direction. The resulting spike train from the PC cluster was obtained at each separation increment.

5.3.2.2 Indenter location on skin surface

The effect of indenter location on the skin surface was analyzed in order to determine whether the spatial distribution of PCs within a cluster could enhance source localization via directional tuning. To do so, a cluster of two horizontally-arranged PCs was created 1 mm beneath the skin surface with an inter-PC separation of 1 mm. Due to symmetry, only one quarter of the skin and PC mesh was analyzed. The location of the indenter was varied across the entire skin surface in increments of 100 μm. The indenter was then varied along an ellipse enclosing both PCs on the skin surface for PCs and PC center depths were increased from 1 to 3 mm.

5.3.3 Nomenclature

The following nomenclature is used in the remainder of this paper. Phase shifts are represented by δ_{ij}^{k}, where the superscript k refers to the physics being analyzed (δ_{ij}^{mech} for a mechanical phase shift and δ_{ij}^{spike} for the phase lag between spikes) and the subscripts i and j correspond to the locations between which phase is measured, where δ_{ij}^{k} is positive if wave i peaks before wave j. The subscripts are S for the stimulus on the skin, 1 for the PC closer to the stimulus, and 2 for the PC further from the stimulus, so δ_{S1}^{mech} and δ_{S2}^{mech} measure the mechanical phase shifts between the surface stimulus and each PC, and δ_{12}^{mech} is the phase shift between the two PCs. Mechanical amplitude ratios are represented by ρ_{ij}, where ρ_{ij} is the ratio between the amplitude at locations i (A_i) and j (A_j) such that $\rho_{ij} = A_i/A_j$. The subscripts S, 1, and 2 again correspond to the stimulus and the PCs closer to and further form the skin stimulus, respectively. Thus, ρ_{1S} and ρ_{2S} measure the amplitude ratio for each PC and the skin stimulus (A_1/A_S and A_2/A_S) and ρ_{12} measures the ratio between the two PC amplitudes (A_1/A_2). L_{12} is used to refer to the center-to-center separation distance between PC_1 and PC_2.

5.4 Results

First, the mechanical effect of embedding PCs within skin was analyzed by observing the resulting oscillation amplitude (ρ_{iS}, Figure 5.3A) and phase shift (δ_{Sj}^{mech}, Figure 5.3B) between the stimulus and location within the tissue in the case where no PCs were embedded within the skin (left) and the case where two PCs were horizontally-arranged with a center-to-center separation (L_{12}) of 800 μm (right). Because the properties of the homogeneous VE PC and inner skin are similar, the wave through the skin slice was not greatly distorted by the presence of the PCs.

5.4.1 Center-to-center separation of PCs

The amplitude ratios (ρ_{1S}, ρ_{2S}) and phase shift (δ_{S1}^{mech}, δ_{S2}^{mech}) between the surface vibration and the top of each PC in the vertically-arranged case are shown in Figure 5.4A. As L_{12} was increased (by moving the deep PC down), the displacement amplitude ratio at the surface of the superficial PC (ρ_{1S}) did not change (Figure 5.4A), but the amplitude ratio for the deep PC (ρ_{2S}) decreased as it moved away from the surface indenter. Likewise, the phase shift between the surface vibration and the vibration of the superficial PC (δ_{S1}^{mech}) did not change (Figure 5.4B), but the phase shift for the deep PC (δ_{S2}^{mech}) increased with L_{12}. Thus, as the deep PC moved further away from the indenter and deeper into the skin model, both the amplitude ratio (ρ_{2S}) and phase (δ_{S2}^{mech}) of the vibration acting on this PC changed.

A similar trend was seen in the horizontally-arranged case (Figures 5.4C and 5.4D) as the lateral PC was moved away from the indenter in the positive x direction. The amplitude ratio (ρ_{1S}) and phase shift (δ_{S1}^{mech}) of the vibration that reached the central PC remained unchanged, but the lateral PC saw a decrease in amplitude ratio (ρ_{2S}) and increase in phase shift (δ_{S2}^{mech}) as L_{12}, and thus distance from the indenter, increased. While the L_{12} values in the vertically- and horizontally-arranged cases were the same, the amplitude ratio for the lateral PC was ~2-3 μm greater than that for the deep PC at a specific separation. Additionally, the phase shift for the lateral PC in the horizontal case was ~1.5-2° (28-37 μs) less than the phase shift for the deep PC in the vertical case. Therefore, the effect of distance was always greater for vertical than for horizontal separation.

Neural spike trains for the PC cluster in both alignment cases at different values of L_{12} were simulated. In both alignment cases, the phase shift between action potentials (δ_{12}^{spike}) increased with PC separation (Figure 5.5). Reflecting the differences seen in the mechanical signals of Figure 5.4, δ_{12}^{spike} in the horizontally-arranged case was 20-30 μs shorter than that in the vertically-arranged case for all separations (corresponding to ~1-1.6° of phase).

5.4.2 Indenter location on skin surface

Two PCs were placed 1 mm beneath the skin surface in the horizontal configuration with L_{12} = 1 mm, and the indenter was moved across the entire surface of the skin in increments of 100 μm. The oscillation amplitudes and phase shifts that reached both PCs were calculated at each indenter location. Contour plots are shown of the ratio ρ_{12} (Figure 5.6A) and the phase shift δ_{12}^{mech} (Figure 5.6B), where PC_1 is outlined in red in Figure 5.6 and PC_2 is located out of the picture in the negative x direction of this figure. As one would expect, the two PCs experience identical inputs (ρ_{12} = 1, δ_{12}^{mech} = 0) when the stimulus is centered between them (x = 0 in Figure 5.6), but if the stimulus is closer to one PC, both a phase lag and an amplitude difference arise. The amplitude ratio is largely independent of position transverse to the line connecting the PC centers, but the phase lag depends on position in both directions.

Because damping does not have a large effect on the mechanics of these simulations, the computed deformations are similar to those of spherical waves in an elastic half-space [172], for which one would expect amplitude to scale as 1/r and phase lag to scale as r. The deformations do not exactly match those of spherical waves, however, because of the viscoelasticity in the model, the finite size of the domain, and the finite size of the indenter. To compare the model results with those expected from spherical waves in an elastic medium, I plotted the amplitude ratio between each PC and the stimulus (ρ_{1S}, ρ_{2S}) vs. $1/L_{jS}$ (Figure 5.7A) and the phase shift between each PC and the stimulus (δ_{S1}^{mech}, δ_{S2}^{mech}) vs. L_{jS} (Figure 5.7B). There are deviations from the idealized case in Figure 5.7. In the amplitude vs. 1/L_{jS} plot (Figure 5.7A), there are deviations from the linear relationship at small values of 1/L_{jS} (PC_j close to the indenter, attributable to the finite indenter size) and deviations at large values of 1/L_{jS} (PC_j far from the indenter, attributable to edge effects in our domain). In the phase shift vs. L_{jS} plot (Figure 5.7B), there are deviations from the linear relationship at large values of L_{jS} (PC_j far from the indenter, again attributed to edge effects). There are no deviations from a linearity in the phase shift vs. L_{jS} plot at small values of L_{jS}.

Since the neuron exhibits integrate-and-fire type behavior [173,174], a higher-amplitude stimulus can produce a spike more quickly, resulting in a potential amplitude contributing to the phase lag between two PCs. Therefore, following on the data of Figures 5.6 and 5.7, the effect of varying ρ_{12} or δ_{12}^{mech} on the phase shift (δ_{12}^{spike}) between action potentials fired by the two PCs was analyzed. First, two PCs were simulated for simultaneous stimulation (δ_{12}^{mech} = 0) but with ρ_{12} values between 1 and 10, and the measured δ_{12}^{spike} was plotted (Figure 5.8A). The resulting δ_{12}^{spike} vs. ρ_{12} plot depends on the specific amplitude values used, so values of A_1 and A_2 were adjusted so that A_2 was equal to various multiples (1X, 2X, 4X) of the amplitude threshold required for action potential firing. For example, in the 1X case, A_1 and A_2 were both initially set to the amplitude threshold required for firing, and then A_1 was increased until ρ_{12} = 10. Varying ρ_{12} had less of an effect on δ_{12}^{spike} when both PCs had relatively high amplitudes. The resulting δ_{12}^{spike} therefore not only depended on ρ_{12} but also on the specific amplitude values of each PC. In all three amplitude value cases, ρ_{12} showed a large effect on δ_{12}^{spike} at small ratios (ρ_{12} < 4), but the effect plateaued at larger ratios. Next, two PCs with δ_{12}^{mech}

values between 0 ms (0° shift) and 6.67 ms (360° shift at 150 Hz) were simulated at the same amplitude (ρ_{12} = 1). As can be seen in Figures 5.7B and 5.7C, δ_{12}^{mech} had a linear effect on δ_{12}^{spike}, as the mechanical phase shift between two PCs directly correlated to their differences in spiking. The combination of amplitude and phase shift drives the neural response of PCs, and thus both of these mechanical inputs must be considered when modeling the resulting spike trains.

The results of Figure 5.8 can be compared to the contour plots in Figure 5.6 to draw conclusions about the relative contributions of ρ_{12} and δ_{12}^{mech} obtained from surface indentation. The values of δ_{12}^{mech} shown in Figure 5.6B are between 0-111 μs, which would result in equal δ_{12}^{spike} values due to mechanical phase lag. The amplitude ratios shown in Figure 5.6A would likely have a larger contribution to δ_{12}^{spike} based on the δ_{12}^{spike} vs. ρ_{12} relationships in Figure 5.8A. For most values of ρ_{12} in Figure 5.6A, the amplitude contribution to δ_{12}^{spike} would dominate over the mechanical phase lag contribution.

Finally, δ_{12}^{spike} was analyzed for different skin surface indenter locations along an ellipse enclosing both PCs (Figure 5.9A). δ_{12}^{spike} was calculated for the indenter locations shown in Figure 5.9A, as indicated by ϕ (Figure 5.9B). Based on symmetry, locations on opposite sides of the ellipse had inverse values of ρ_{12} and δ_{12}^{mech}, which resulted in opposite δ_{12}^{spike} values. As the PCs were moved deeper into the skin, the absolute value of δ_{12}^{spike} at each ϕ decreased due to decreases in ρ_{12} and δ_{12}^{mech}. The values of δ_{12}^{spike} in Figure 5.8B are quite large, with δ_{12}^{spike} at ϕ = 0° ranging from approximately 11° for the 3 mm depth case to 19° for the 1 mm depth case. In addition, as the PC depth increased, the difference L_{S2}-L_{S1}, where L_{S1} and L_{S2} are the distances from the center of the stimulus indenter to the center of each PC, decreases. For example, for the stimulus at $\phi = 0°$, L_{S2}-L_{S1} is 1 mm on the surface but decreases to 0.68 mm at 1 mm depth and then to 0.44 mm and 0.32 mm at 2 and 3 mm depth, respectively. This decrease in L_{S2}-L_{S1} with increasing depth results in a decrease in the phase lag (δ_{12}^{mech}) measured between the two PCs, which, in addition to the attenuation of amplitude at deeper locations in the skin, causes the decrease in δ_{12}^{spike} seen in Figure 5.9B.

5.5 Discussion

In this work, I used a computational model to investigate how a mechanical stimulus affects a cluster of two PCs embedded within skin. I used a homogeneous viscoelastic PC model embedded within simulated human skin to obtain the mechanical signals experienced by each PC in response to a 150 Hz skin surface vibration. I then used a three-stage model of the PC's mechano-to-neural transduction [24] to simulate the action potentials generated by the PCs.

The small effect of the PC on the wave transmission through the skin (Figure 5.3) suggests that it may not be necessary to model PCs in the skin. Rather, PCs, and potentially other mechanoreceptors, may be able to be modeled as phantom detectors as in the recent model by Saal et al. [174]. A model of skin mechanics, in which deformations at specific depths and locations in the skin resulting from a vibrotactile skin stimulus can be obtained, can be coupled to a model of a single of multiple receptors to simulate the neural response elicited by the measured skin deformation at the receptor's location. This has the advantage of not requiring complex single-receptor models to be reconstructed into an equivalent to insert into the skin mechanics model.

The results of this study suggest an advantage of the natural clustering of PCs *in vivo*, as the geometrical grouping of these PCs causes each receptor in the cluster to receive a different mechanical signal, which in turn causes the spike trains elicited by each PC in response to a skins surface vibration to vary. This variation in signal could allow for the transmission of greater information content and facilitate the recognition and discrimination of complex stimuli.

Parallels between the senses of touch and hearing have been identified in the literature, ranging from the comparison of the structural composition of the filopodia on the PC's neurite [43] with the sterocilia of hair cells [47] to the neural codes responsible for the processing of spike trains in mechanosensitive and auditory afferents [169]. An analogy may also be drawn between sound localization in the auditory system and the potential for stimulus localization with PC clustering. The results of this study show that PCs within a cluster may receive mechanical stimuli with different amplitudes and phase shifts from the stimulus depending on their distance from each other and from the stimulus (Figures 5.4 and 5.6). Likewise, binaural hearing allows for sound localization by comparing the auditory signal at one ear with the signal at the other via interaural level difference and interaural time difference [175,176]. The amplitude and phase shift differences measured between two PCs in this study may have similar roles in the localization of tactile vibrations. Binaural hearing improves auditory performance by enabling better localization of a sound source [175], which suggests that PC clustering may support better source localization of vibratory stimuli and may therefore enhance tactile sensation. A single PC has low spatial sensitivity across the surface of skin, resulting in a receptive field that may span an entire hand [2]. Clusters of multiple PCs may therefore allow for better resolution of vibrotactile stimulus locations. In addition, a human has hundreds of PCs per hand [17,88] but only two ears, so beyond clusters, the potential for multi-PC-based stimulus localization is high.

Source localization could be further explored by modeling the PCs as ellipsoidal, rather than spherical and/or with variation in the number of lamellae. Previous experiments [132,177] identified functional asymmetry within the PC, as the receptor potentials shifted between hyperpolarization and depolarization upon rotation about the PC's axes. This asymmetry may be due to the ellipsoidal shape of the PC's outer core or neurite [108,132,177]. Modeling the ellipsoidal shape of PCs within a cluster and their orientation with respect to each other would allow for the study of how the PC's directional sensitivity may further improve source localization by the cluster. Similarly, since PCs with different numbers of lamellae would be expected to tune to different frequencies [24,33], a cluster could be a more effective sensor than any single PC. Microstructural characterization studies must first be done to document the sizes and structures of PCs within a cluster, as well as their proximity to and orientation with respect to the other receptors in the cluster.

The two simulated PCs in this study had identical nerve fibers, both in their structural and electrochemical properties. The two neurites in the simulated clusters had the same conduction velocities, and varying this as well as other electrochemical properties within each neurite (i.e. neurite dimensions, type and number of ion channels), would affect $\delta_{12}^{\mathrm{spike}}$. The current study measures $\delta_{12}^{\mathrm{spike}}$ resulting from differences in the mechanical signal that reaches each PC (ρ_{1S}, ρ_{2S}, $\delta_{S1}^{\mathrm{mech}}$, $\delta_{S2}^{\mathrm{mech}}$) due to the relative locations of the PCs with respect to each other and the stimulus location, but the measured values could also be affected by differences in the structural and electrochemical properties of the two neurites.

In this study, I simulated a cluster of two PCs. Clusters in the human may include more than two PCs, as clusters of up to 11 PCs have been observed in dissection studies of various animal species [34,46,54,55,61,76–78]. Wu et al. [81] used microneurography to record the activity of afferents in human skin and identified PC afferents by analyzing their receptive field size and response to constant pressure and vibration. Wu et al. recorded the number of PC units at each recording site and found that PC afferent clustering of more than one afferent occurred more often (46%) than expected (6%) based on the proportion of PC afferents (15%) among the four main types of mechanoreceptors in human glabrous skin [22,81]. In their thirteen total observations, two PCs were identified in a single recording site five times and three PC afferents were identified in a single site one time [81]. While groupings of two PCs may enhance the localization of a skin stimulus, larger clusters may provide further improvement of source localization.

The two most important conclusions are a pragmatic one and a scientific one. The pragmatic conclusion is that the PC does not significantly alter wave propagation through the skin, so it does not need to be included explicitly in a model of the wave propagation through the skin, validating an assumption implicit in the creation of one-way coupled models (e.g., Tanaka et al. 2015; Saal et al. 2017). Although this conclusion is not of great scientific interest, it is important in the development of future models of haptic systems. The major scientific conclusion from this work is that even a relatively small amount of separation between two PCs in a cluster can lead to a measurable phase lag in the spike trains of the two neurons, meaning that there is additional information provided to the somatosensory cortex by means of the cluster, which could in turn be used for source localization or signal identification.

Table 5.1: Skin and PC material constants

<table>
<tr><th colspan="8">SKIN</th></tr>
<tr><th>Section Label</th><th>Skin Components</th><th>Thickness (mm)</th><th>Poisson’s Ratio</th><th>Young’s Modulus</th><th>Mass Damping Parameter (s^{-1})</th><th>Stiffness Damping Parameter (s)</th><th>References</th></tr>
<tr><td>Outer Skin (OS)</td><td>Epidermis</td><td>0.5</td><td>0.48</td><td>180 kPa</td><td>$1x10^{-7}$</td><td>$0.4x10^{-3}$</td><td>[123,146,170]</td></tr>
<tr><td>Inner Skin (IS)</td><td>Dermis, Subcutaneous Tissue/ Hypodermis</td><td>6</td><td>0.48</td><td>18 kPa</td><td>$1x10^{-7}$</td><td>$0.4x10^{-3}$</td><td>[30,123,146,170]</td></tr>
<tr><td>Bone (B)</td><td>Bone</td><td>1.5</td><td>0.48</td><td>1.8 GPa</td><td>$1x10^{-4}$</td><td>$1x10^{-7}$</td><td>[146,170]</td></tr>
<tr><th colspan="8">PACINIAN CORPUSCLE</th></tr>
<tr><th colspan="2">Section Label</th><th>Radius (μm)</th><th>Poisson’s Ratio</th><th>E$_1$ (kPa)</th><th>E$_2$ (kPa)</th><th>η (Pa-s)</th><th>References</th></tr>
<tr><td colspan="2">PC</td><td>255.6</td><td>0.48</td><td>3</td><td>500</td><td>5.5</td><td>[23,24,116]</td></tr>
</table>

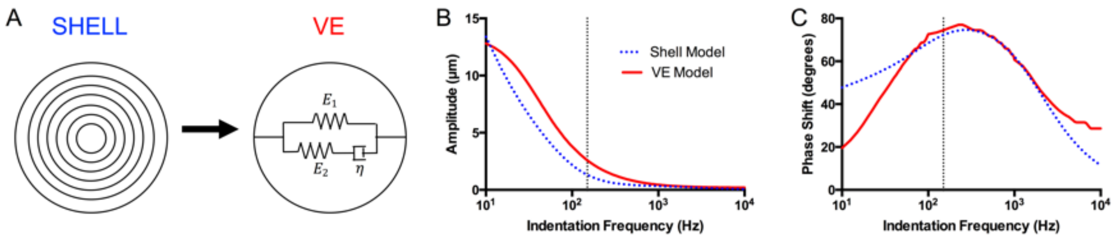

Figure 5.1: Multilayer shell-fluid model and homogeneous viscoelastic equivalent. (A) A multilayer coupled shell-fluid model (left) of the PC outer core was fit to a homogeneous viscoelastic (VE) model in COMSOL. The VE PC was modeled as a standard linear solid with parameters E_1, E_2, and η. **(B)** The maximum displacement amplitude on the PC outer surface at various indentation frequencies for the shell (blue dots) and VE (red solid line) PC models. A vertical dashed black line is drawn at 150 Hz, which is the frequency at which all subsequent simulations were run in this paper. **(C)** The phase shift between maximum pressure and maximum displacement on the PC outer surface for the shell and VE models.

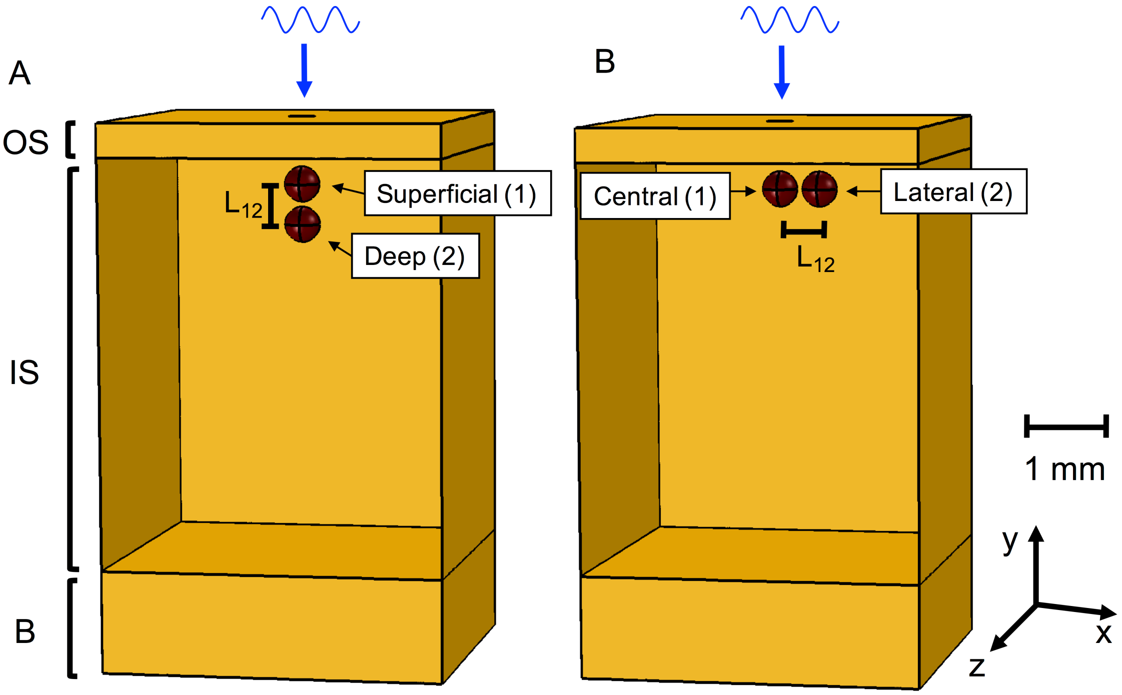

Figure 5.2: Vertically- and horizontally-arranged PC cases. (A) In the vertically-arranged PC case, the two spherical PCs were aligned at the center (x=0, z=0) of the skin mesh, directly under the indenter (arrow). The center of the superficial PC was located 1mm beneath the surface of the skin. In subsequent simulations, the center-to-center separation between the two PCs (L_{12}) was increased as the location of the deep PC was moved in the negative y direction, increasing the separation. Labels on the side correspond to different layers of the skin (Table 5.1): outer skin (OS), inner skin (IS), and bone (B). Numbers next to the PC names correspond to the numbers used to reference the PCs in the nomenclature, where 1 refers to the PC closer to the indenter and 2 refers to the PC farther from the indenter. **(B)** In the horizontally-arranged PC case, the central PC was aligned at the center (x=0, z=0) of the skin mesh, directly under the indenter (blue arrow). The centers of both PCs were located 1 mm beneath the surface of the skin. In subsequent simulations,

L_{12} was increased as the location of the lateral PC was moved in the positive x direction. Numbers next to the PC names correspond to the numbers used to reference the PCs in the nomenclature.

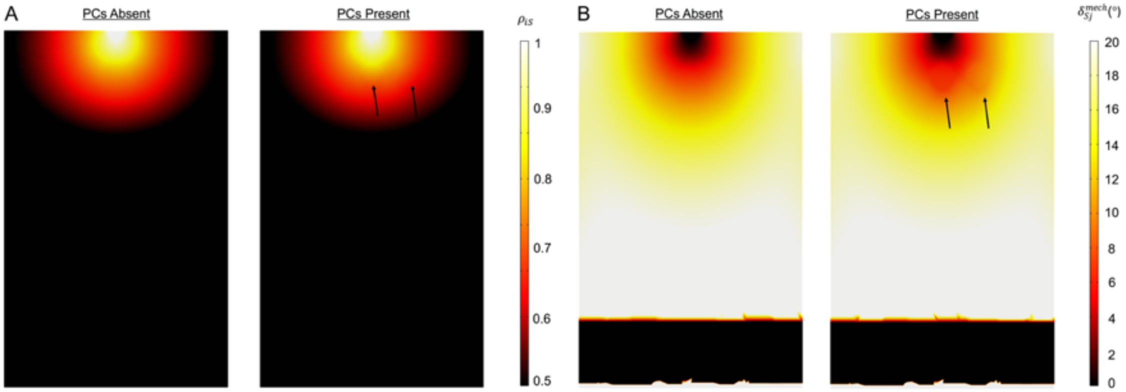

Figure 5.3: Amplitude (ρ_{iS}) and phase shifts (δ_{Sj}^{mech}) through cross-section of skin mesh with and without PCs. (A) The amplitude ratio (ρ_{iS}) between all locations in the mesh (i) and the stimulus (S) plotted in a 2D slice (x-y plane) through the skin mesh (z=0) in Figure 5.2B. ρ_{iS} is plotted in the case where no PCs were located in the skin (left) and the case with the lateral PC located 800 μm away from the central PC in the positive x direction (right) with the PC locations indicated by arrows. **(B)** Phase shift (δ_{Sj}^{mech}) between the stimulus (S) and all locations in the mesh (j) plotted in a 2D slice (x-y plane) through the skin mesh (z=0) in Figure 5.2B for the case of no PCs (left) and the case with the lateral PC located 800 μm away from the central PC in the positive x direction (right) with the PC locations indicated by arrows.

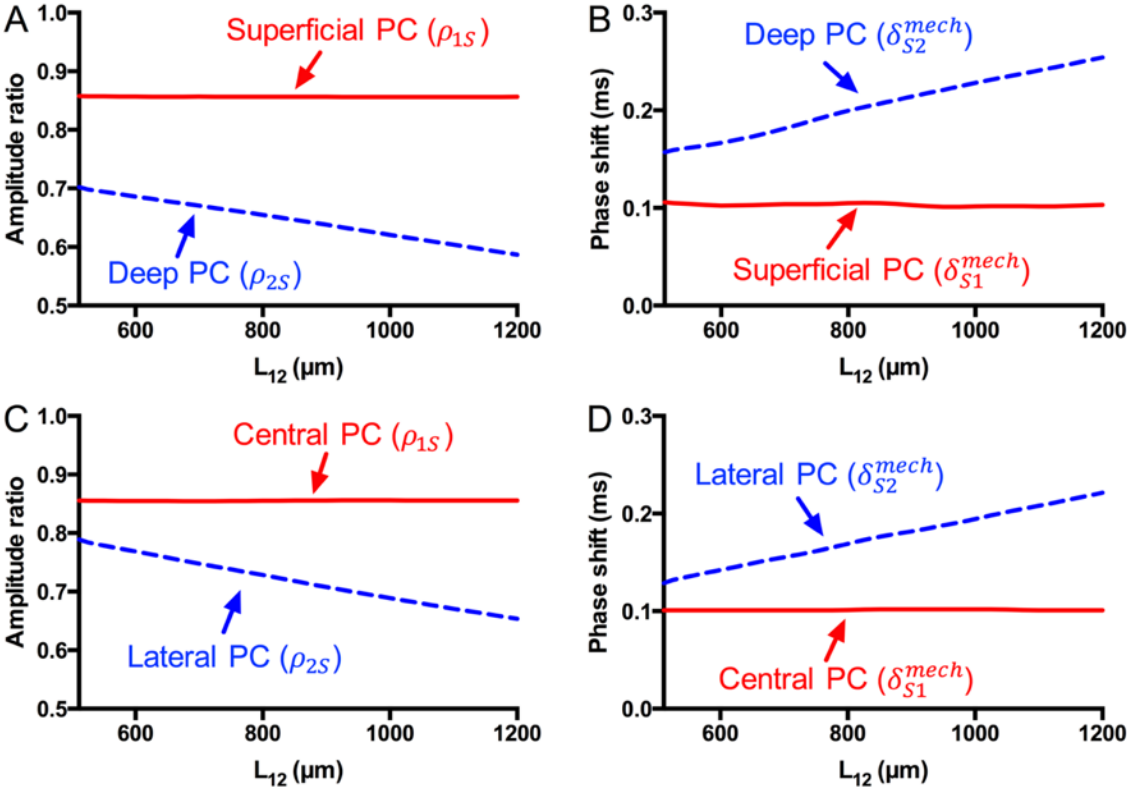

Figure 5.4: Amplitude ratios (ρ_{1S}, ρ_{2S}) and phase shifts (δ_{S1}^{mech}, δ_{S2}^{mech}) for vertically-arranged (A,B) and horizontally-arranged (C,D) PCs with increasing center-to-center separations (L_{12}). (A) Amplitude ratio between the maximum amplitude at the surface of the superficial (ρ_{1S}, solid line) and deep (ρ_{2S}, dashed line) PCs and the surface indentation in the vertically-arranged case (Figure 5.2A) for increasing L_{12}. **(B)** Phase shift between the indenter displacement wave and the maximum PC displacement for the superficial (δ_{S1}^{mech}) and deep (δ_{S2}^{mech}) PCs in the vertically-arranged case. **(C)** Amplitude ratio between for the central (ρ_{1S}, solid line) and lateral (ρ_{2S}, dashed line) PCs and the surface indentation in the horizontally-arranged case (Figure 5.2B) for increasing L_{12}. **(D)** Phase shift between the indenter displacement and PC displacement waves for the central (δ_{S1}^{mech}) and lateral (δ_{S2}^{mech}) PCs in the horizontally-arranged case.

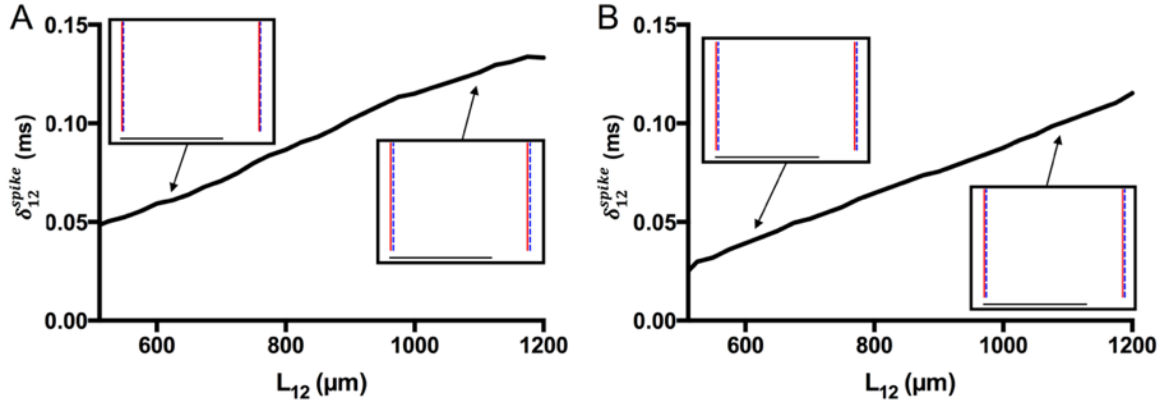

Figure 5.5: Phase shift of action potentials ($\boldsymbol{\delta_{12}^{spike}}$) for vertically- and horizontally-arranged PCs with increasing $\mathbf{L_{12}}$. (A) δ_{12}^{spike} for the superficial (PC_1) and deep (PC_2) PCs in the vertically-arranged case (Figure 5.2A) for increasing L_{12}. Inset figures show representative raster plots of the simulated action potentials from the superficial (solid line) and deep (dashed line) PCs. Inset scale bar corresponds to 5 ms. **(B)** δ_{12}^{spike} for the central (PC_1) and lateral (PC_2) PCs in the horizontally-arranged case (Figure 5.2B) for L_{12}. Inset figures show representative raster plots of the simulated action potentials from the central (solid line) and lateral (dashed line) PCs. Inset scale bar corresponds to 5 ms.

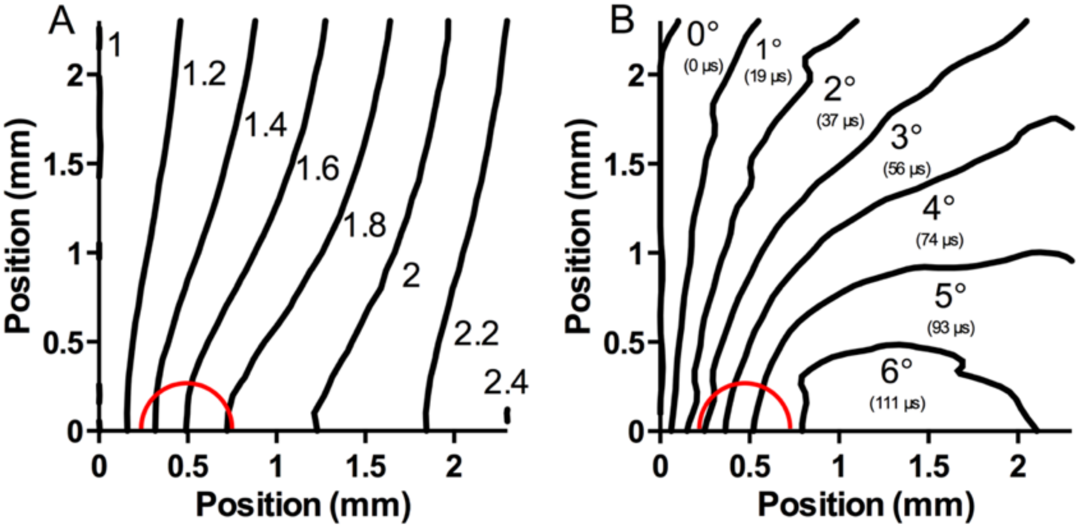

Figure 5.6: Contour plots of $\boldsymbol{\rho_{12}}$ and $\boldsymbol{\delta_{12}^{mech}}$ resulting from stimulation at varying locations on skin mesh surface. (A) Contour plot of the ratio ρ_{12} measured after indentation at each point on the skin surface, where PC$_1$ is outlined in red and PC$_2$ is out of the picture (in the negative x direction) for a quarter of the skin. **(B)** Contour plot of the value δ_{12}^{mech} where phase shifts in degrees are shown with time conversions in parentheses.

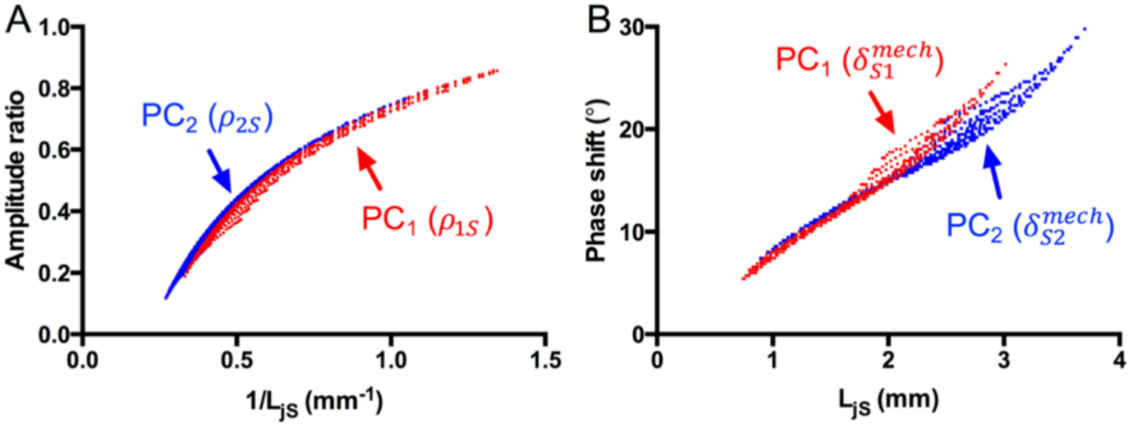

Figure 5.7: Amplitude ratios ($\boldsymbol{\rho_{1S}}$, $\boldsymbol{\rho_{2S}}$) vs. 1/L$_{jS}$ and phase shifts ($\boldsymbol{\delta_{S1}^{mech}}$, $\boldsymbol{\delta_{S2}^{mech}}$) vs. L$_{jS}$ for the two PCs simulated in Figure 5.6. (A) ρ_{1S} (red circles) and ρ_{2S} (blue squares) are plotted vs. 1/L$_{jS}$, where L$_{jS}$ is the distance from the center of each PC to the center of the indenter. PC$_1$ is the PC outlined in red in Figure 5.6 and PC$_2$ is out of the picture (further from the indenter). **(B)** δ_{S1}^{mech} (red circles) and δ_{S2}^{mech} (blue squares) are plotted vs. L$_{jS}$.

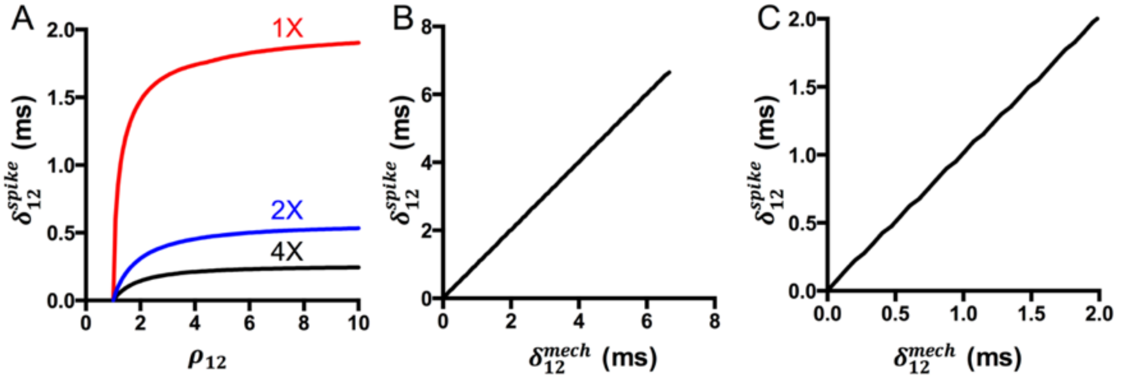

Figure 5.8: Effect of ρ_{12} and δ_{12}^{mech} on δ_{12}^{spike} within a cluster of 2 PCs. (A) δ_{12}^{spike} measured from a cluster of 2 PCs with varying ρ_{12} ratios and $\delta_{12}^{mech} = 0$. The values of A_1 and A_2 were adjusted so that A_1 and A_2 were equal to various multiples (1X, 2X, 4X) of the amplitude threshold required for action potential firing at $\rho_{12} = 1$. **(B)** δ_{12}^{spike} measured from 2 PCs with varying δ_{12}^{mech} and $\rho_{12} = 1$. **(C)** Plot from (B) zoomed in on 0-2 ms range for comparison with (A).

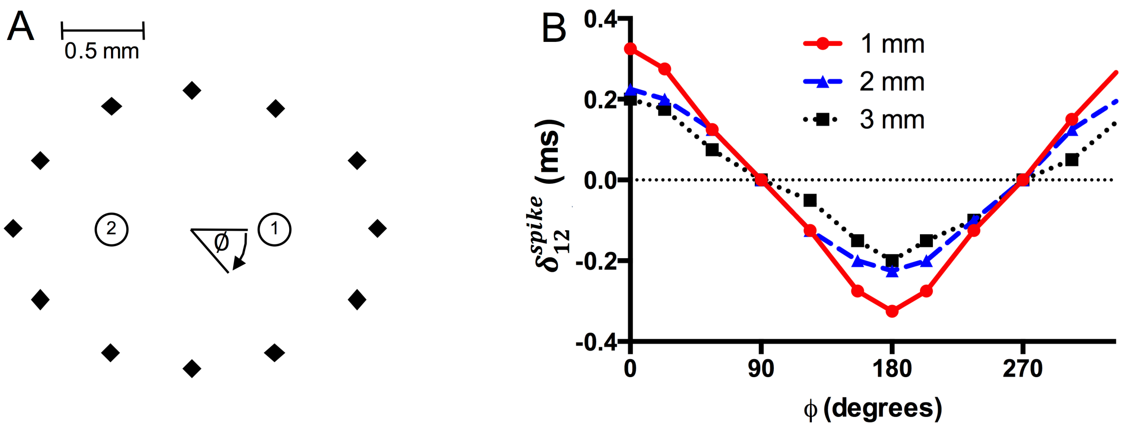

Figure 5.9: Indenter locations around an ellipse and calculated δ_{12}^{spike} at different PC depths. (A) The skin was indented with the indenter located at positions indicated by filled diamonds in the pattern shown here. The locations of the two PCs (black unfilled circles) were kept constant and the angle of the indenter with respect to the axis of PC alignment (ϕ) was varied along the edge of an ellipse with a semimajor axis of length 2 mm and a semiminor axis of length 1.73 mm. **(B)** δ_{12}^{spike} was calculated for each indenter location shown in Figure 5.9A at PC depths of 1, 2, and 3 mm.

CHAPTER 6: MICROPIPETTE ASPIRATION OF THE PACINIAN CORPUSCLE

The content of this chapter was accepted as a research article to the *Journal of Biomechanics* (Quindlen, Bloom, Ortega, Moeller, Barocas) in August 2017 and is currently in press [116].

6.1 Summary

Previous theoretical and computational studies have modeled the physiological response of the PC to sustained or vibrating mechanical stimuli, but they have used estimates of the receptor's mechanical properties, which remain largely unmeasured. In this study, I used micropipette aspiration (MPA) to determine an apparent Young's modulus for PCs isolated from a cadaveric human hand. MPA was applied in increments of 5 mm H_2O (49 Pa), and the change in protrusion length of the PC into the pipette was recorded. The protrusion length vs. suction pressure data was used to calculate the apparent Young's modulus. Using 10 PCs with long-axis lengths of 2.99 mm ± 0.41 mm and short-axis lengths of 1.45 mm ± 0.22 mm, I calculated a Young's modulus of 1.40 ± 0.86 kPa. This measurement is on the same order of magnitude as those approximated in previous models, which estimated the PC to be on the same order of magnitude as skin or isolated cells, so I recommend that a modulus in the kPa range be used in future studies.

6.2 Introduction

The PC has long intrigued biomechanicians, with seminal theoretical work done by Loewenstein and Skalak half a century ago [23]. More recently, the field of haptics and the emerging need for better haptic feedback systems [114] have inspired the development of computer models of how our peripheral nervous system, and specifically mechanoreceptors, encode vibrotactile stimuli. Models of PC mechanics are becoming quite common [23,24,32,109,115]. In spite of the high degree of sophistication and creativity in PC models, the lack of complete data to specify the model parameters remains a considerable obstacle. Previous characterization studies [16,25,35,36] identified the microscopic structure of the PC and thus informed the structural components of theoretical models. Mechanical studies, however, have been much less common and have focused primarily on kinematics, in particular how imposed static surface displacements are transmitted through the PC structure [10,23]. To our knowledge, there has been no published study of PC mechanics that included an actual force or stress measurement. A review article by Bell et al. [18] stated that the Young's modulus of the PC was measured at 1 kPa, but the cited source was a conference abstract [125] that does not include a value or any experimental data; One might guess that Pietras and Bolanowski discussed measurements in the presentation, but they never published their results. As a result, a wide range of values for the Young's modulus of the PC has been used in theoretical models. In their earlier work, Loewenstein and Skalak [23] suggested a PC modulus in the MPa range, comparable to that of arterial wall; in contrast, Güçlü et al. [109] and Biswas et al. [32] argued for a modulus in the kPa range, closer to that of skin or an isolated cell, and obtained much more realistic results from their models when using the lower modulus value, as did

I in my recent work presented in Chapters 2-5 [24,33,115]. None of these studies, however, used a value based on mechanical characterization of the PC.

To address this gap, I performed micropipette aspiration on isolated PCs to characterize the Young's modulus of PCs obtained from the cadaveric human hand.

6.3 Methods

6.3.1 PC isolation

The University Anatomy Bequest program provided a hand specimen for PC collection. Ten PCs were isolated from the palm and index finger of a 63-year-old female. A longitudinal midline incision was made from the distal palmar flexion crease to the distal interphalangeal joint flexion crease of the index finger. Full thickness skin flaps were elevated. The radial and ulnar neurovascular bundles were identified in the proximal aspect of the incision and traced distally. The PCs were identified under loupe magnification and harvested utilizing microsurgery instruments and atraumatic dissection. Mean length values and aspect ratios of the PCs are listed in Table 6.1.

6.3.2 Micropipette aspiration (MPA) experimental set-up

MPA, which has been used often to characterize the mechanical behavior of single cells (e.g. [179–183]), was applied to the PC for our purpose. MPA involves applying negative pressure to the surface of a deformable object with a micropipette, usually in regular pressure and time increments. The protrusion of the aspirated specimen into the micropipette is monitored to determine its Young's modulus [180,184].

The MPA apparatus consisted of a mounted pipette (666 μm inner diameter) connected by polyethylene tubing to a height-adjustable water reservoir. The specimen to be studied was placed in a petri dish filled with 0.9X PBS solution located on the microscope stage at the pipette tip. The water reservoir was raised or lowered until the sample adhered to the pipette tip without entering the pipette. As the fluid surface of the reservoir was lowered below the height of the fluid surface in the petri dish, a negative pressure was applied, and the specimen was drawn into the micropipette. A Leica S6D microscope with a MotiCam 1000 digital microscopy camera working with MoticImages 2.0 Plus was used to image the protrusion of the PC into the micropipette.

Each PC was tested in two different orientations: once with the pipette parallel to the short axis (Figure 6.1A; henceforth "SA orientation") and once with the pipette parallel to the long axis (Figure 6.1B; "LA orientation"). For each orientation, suction pressure was increased as the water reservoir was lowered in 5 mm (49 Pa) increments and held for two minutes at each pressure (henceforth referred to as "increasing" trials). The process was repeated until a total height change of 80 mm (applied suction pressure of 784 Pa) was achieved. Pressure was then decreased at the same rate until the water reservoir had returned to its original position ("decreasing" trials). Images were taken at each pressure step.

Two minutes was deemed a sufficient amount of time to allow the tissue to equilibrate with the applied pressure following preliminary equilibration experiments (Figure 6.2). In these experiments, the PC suction pressure was set to a value in the range 49-196 Pa for 5 minutes and the protrusion length into the pipette (SA orientation) was recorded every 30 seconds. After 2 minutes of equilibration at all four suction pressures, the protrusion length change (Δd) was greater than 99% of the maximum protrusion length change (Δd_{max}) recorded. The data shown in Figure 6.2 were fit to exponential decay (Equation 6.1), where c_1 measures the height of growth and c_2 inversely is the characteristic relaxation time. The time constant c_2 changed for each pressure setting but was never above 38.8 seconds (mean = 19.0 seconds, SD = 14.7 seconds).

$$\Delta d/\Delta d_{max} = 1 - c_1 e^{\left(-t/c_2\right)} \tag{6.1}$$

6.3.3 MPA analysis

The protrusion length of the PC into the pipette tip was determined by calculating an average of three measurements obtained using ImageJ software (U. S. National Institutes of Health, Bethesda, MD, USA, http://imagej.nih.gov/ij/, 1997-2016) at each pressure level. We identified three potential sources of error in the protrusion length measurement. The largest was the pixel size, which was 22.45 µm for our standard image. We also tested intraobserver reproducibility (σ = 3 µm for three independent measurements by the same observer) and interobserver reproducibility (σ = 16.4 µm for measurements by eleven different test observers). Based on these values, we estimate that the error in our measurements was 20-25 µm. In light of the estimated 20-25 µm error, we needed to use a pipette large enough to allow for a protrusion of hundreds of microns. This larger pipette size, however, made the common assumption of a half-space material inaccurate, so data were analyzed using the fitted model of Zhou et al. [183]. The apparent Young's modulus E was calculated by fitting the plot of protrusion length vs. the applied suction pressure to the large-pipette correction equation of Zhou et al.:

$$\frac{3\Delta P}{E} = \left[\beta_1 \frac{\Delta d}{R_p} + \beta_2 \left(\frac{\Delta d}{R_p}\right)^2\right]\left[1 - \left(\frac{R_p}{R_c}\right)^{\beta_3 + \beta_4 \frac{\Delta d}{R_p} + \beta_5 \left(\frac{\Delta d}{R_p}\right)^2}\right] \tag{6.2}$$

where R_p is the inner radius of the pipette, R_c is the radius of the PC, ΔP is the change in applied pressure, Δd is the change in protrusion length of the aspirated sample into the pipette tip, β_1 = 2.0142, β_2 = 2.1186, β_3 = 2.1187, β_4 = -1.4409, and β_5 = 0.3154. The change in protrusion length of the aspirated sample into the pipette tip (Δd) was approximated as

$$\Delta d = L_p - L_o \tag{6.3}$$

where L_p was the aspirated protrusion length of the sample into the pipette at various pressure values as measured in the experiment and L_o was the protrusion of the sample into the pipette at zero pressure. L_o could not be measured in our experiments, so it was also treated as a fitting parameter. Values of 0.16 ± 0.07 mm and 0.20 ± 0.08 mm were obtained for the low suction pressure regimes of the increasing and decrease pressure trials for the SA orientation, respectively. Values of 0.19 ± 0.07 mm and 0.27 ± 0.05 mm were obtained for the low suction pressure regimes of increasing and decrease pressure trials for the LA orientation. L_o changed from the low- to high-pressure regimes due to the nonlinearity of the material, but we only report the L_o values for the low-pressure (small strain) regimes because these values are more relevant.

We refer to E as an *apparent* Young's modulus because Equation 6.2 is derived for a homogeneous linear solid, whereas the PC is not homogeneous and could experience large strains during the experiment. The value used for R_c was an effective radius that was dependent on the pipette's orientation. Due to the PC's ellipsoidal shape, the two radii of curvature ($R_1$and R_2) exposed to the pipette in each orientation were used to calculate the harmonic mean radius (H). H was used for R_c in Equation 6.2 where H is calculated with the equation

$$\frac{1}{H} = \frac{1}{2}\left(\frac{1}{R_1} + \frac{1}{R_2}\right) \tag{6.4}$$

For the SA orientation (Figure 6.1A), the PC surface exposed to the pipette had one radius of curvature equal to the long axis (R_{LA}) and one equal to the short axis (R_{SA}). H was given by

$$\frac{1}{H} = \frac{1}{2}\left(\frac{1}{R_{LA}} + \frac{1}{R_{SA}}\right) \tag{5}$$

For the LA orientation (Figure 6.1B), the radii of curvature exposed to the pipette were both R_{SA}, so the effective radius of the PC was R_{SA}.

The apparent Young's modulus was calculated by fitting Equation 6.2 to protrusion length vs. suction pressure data for each of two suction pressure regimes that occurred in increasing and decreasing pressure trials: low suction pressure (49-392 Pa) and high suction pressure (441-784 Pa).

6.4 Results

A time series of the images acquired at each suction pressure during an experiment is shown in Figure 6.3 for a representative PC tested in the SA orientation. ImageJ was used to measure the protrusion length for each image. Measured protrusion lengths for a representative PC during MPA are shown for both increasing and decreasing pressure trials with the pipette in the SA (Figure 6.4A) and LA orientations (Figure 6.4B). Figures 6.4A and 6.4B show the protrusion length vs. suction pressure for the entire range of pressures, with lines of best fit in the low-pressure (49-392 Pa) and high-pressure (441-784 Pa) regimes. As can be seen in Figure 6.3 and Figures 6.4A and 6.4B, there was a slight plateau in protrusion length for the decreasing pressure trial in the high-pressure regime, as the PC did not exit the pipette at the same rate at which it entered. The final protrusion length measurement at 49 Pa was greater than the initial protrusion length measured at this same pressure at the beginning of the experiment, indicating that the PC did not completely exit the pipette as pressure was decreased.

The data shown in Figures 6.4A and 6.4B were used to calculate E via Equation 6.2 for the low- and high-pressure regions of the increasing and decreasing pressure trials in each pipette orientation, resulting in eight modulus values per PC. The average moduli and 95% confidence intervals are plotted in Figures 6.4C and 6.4D for both pipette orientations and both pressure regimes. All average modulus values in Figures 6.4C and 6.4D are on the order of a few kPa, which is comparable to values recently used in computational PC models [24,32,109] and the value cited in the literature [18,125].

There was no significant difference ($p > 0.05$) between the E values calculated in the SA and LA orientation results for all pressure regimes and trials. Thus, the apparent modulus can be obtained from MPA in either orientation. When considering the apparent modulus calculated for increasing vs. decreasing pressure trials in the different orientations, there was no significant difference ($p > 0.05$) between the E values calculated in the increasing and decreasing pressure trials for either pressure regime in the LA orientation or for the SA orientation low-pressure regime. There was, however, a significant difference between the increasing and decreasing pressure trials in the SA orientation high-pressure regime ($p < 0.02$). There was therefore only a difference in the apparent modulus calculated from increasing vs. decreasing pressure trials in one of the four orientation/pressure regime combinations. The low-pressure regime was deemed the more physiologically-relevant value to characterize the receptor, as the PC responds to low-amplitude vibrations [20,21]. The average apparent Young's modulus for all low-pressure data in both pipette orientations was 1.40 ± 0.86 kPa.

6.5 Discussion

The major contribution of this study is the characterization of the PC's apparent Young's modulus via mechanical experiments. This is, to our knowledge, the first published study to identify the Young's modulus of isolated human cadaveric PCs, or of PCs from any species. The results of this study will better inform future computational models of the receptor and will lead to more accurate simulations of PC dynamics. Evaluating the mechanical characteristics of the PC is a critical step towards understanding the mechanical-to-neural transduction process of the receptor and the phenomenon of vibrotactile sensitivity.

Prior to this study, computational models [23,24,32,109,115] of the PC have largely relied on mechanical comparisons between the PC and other anatomical structures when selecting a Young's modulus approximation for the PC and/or choosing values that resulted in the model matching the PC's characteristic bandpass behavior. The cited studies have modeled PC mechanics with modulus values ranging from the kPa scale, comparing the PC's stiffness to that of an isolated cell [32] or skin [109,115], to the MPa scale, comparing the PC's stiffness to that of arterial walls [23]. The average modulus obtained in this study, 1.40 ± 0.86 kPa, is much closer to the modulus values used in recent publications [24,32,109,115] and that anecdotally mentioned by Bell et al. [18], suggesting that the PC's stiffness is on the same order of magnitude as that of skin [109,185].

The PC has a highly detailed inner structure composed of a central neurite surrounded by an inner core of bilaterally-arranged lamellae derived from Schwann cells [36,43,49], an intermediate growth zone [36], and an outer core of alternating layers of concentrically-aligned epithelial-type lamellae and fluid-filled spaces [18,36]. The PC is therefore a complex, multilayered structure with mechanics that are governed by the lamellar modulus and fluid viscosity within the PC's different inner zones. In this study, however, the PC was analyzed as a homogenous material, yielding a single apparent modulus for the entire structure. Caution must be taken in comparing results of this study to previous models [23,24,32] that used a lamellar modulus and not an effective overall tissue modulus. A single modulus approximation for the entire receptor, however, can still inform computer models of PC mechanics. In this study, we approximated the PC to be a solid sphere, which may be considered one limit at which the PC can behave. The other limit, which involves approximating the PC as a solid shell encapsulating a fluid structure, has been explored in micropipette modeling studies on cell mechanics [186–188]. At this limit, the Young's modulus for the solid shell can be estimated [188,189] from our data, and a value of 2.96 kPa was obtained for the one-shell limit. The actual behavior of the PC likely falls somewhere between these two extremes, as the PC structure contains multiple layers and is not a homogeneous solid [36]. Thus, the PC's Young's modulus can be hypothesized to be on the order of a few kPa.

The experiments performed in this study explored the mechanical properties of the PC under steady-state conditions. While steady-state characterization is an important metric, and these experiments are able to provide us with a first experimental approximation of a PC's properties, they do not do so on a physiologically-relevant time scale, as the PC responds to frequencies in the 20-1000 Hz range [20,190] and therefore behaves on the millisecond time scale [148]. Obtaining the mechanical properties of the PC under dynamic conditions during its normal deformation is critical to understanding how the PC responds to vibrations *in vivo*.

Two pressure regimes were seen in the data: a low-pressure regime, which occurred between 49 and 392 Pa suction pressure and was characterized by high initial deformation, and a high-pressure regime, which was between 441 and 784 Pa and showed less deformation in response to changes in pressure. The apparent Young's modulus E was calculated for both pressure regimes (Figures 6.4C and 6.4D). As mentioned previously, the E value for the low-pressure regime (1.40 ± 0.86 kPa) was deemed the more physiologically-relevant value to characterize PC mechanical behavior. During the experiment, the PC was aspirated into the pipette as pressure was increased. There was no significant difference between the apparent stiffness for the low- and high-pressure regimes when the pipette was in the SA orientation for the increasing ($p = 0.055$) pressure trials. There was, however, a significant difference between the two pressure regimes in the SA orientation for the decreasing ($p = 0.0027$) pressure trials. When the pipette was in the LA orientation, there was a significant ($p = 0.0062$) change in stiffness between the low- and high-pressure regimes of the increasing pressure trial but no significant ($p = 0.062$) difference between the two regimes in the decreasing trial. The increase in apparent modulus between the two regimes may be a result of collagen fiber recruitment in the tissue at higher aspiration pressures [191]. When the maximum suction pressure was reached (784 Pa), pressure was decreased until the PC lost contact with the pipette at 0 Pa. A slight plateau in measured protrusion lengths occurred during the high-pressure region as suction pressure was decreased, suggesting that friction between the sample and the pipette may have limited the sample's motion. Applying non-adhesive agents to the pipette tip may prevent friction between the PC and pipette wall during decreasing pressure trials in future experiments. At the final applied suction pressure during the trial (49 Pa), the measured protrusion length was greater than that measured at 49 Pa suction pressure in the beginning of the aspiration (Figures 6.4A and 6.4B). The aspirated PC therefore did not completely escape from the pipette as pressure decreased. This may be indicative of viscoelastic or poroelastic hysteresis within the tissue, as the PC contains alternating layers of fluid and solid lamellae which contribute to the receptor's viscoelasticity. Future experiments on dynamic loading of isolated PCs will be useful to provide insight into the time-dependent behavior of the tissue.

Table 6.1: Mean length values of PCs used in MPA experiments

Number of samples	10
Long Axis Length (mm)	2.99 ± 0.41
Short Axis Length (mm)	1.45 ± 0.22
Aspect Ratio (Long:Short)	2.09 ±0.33

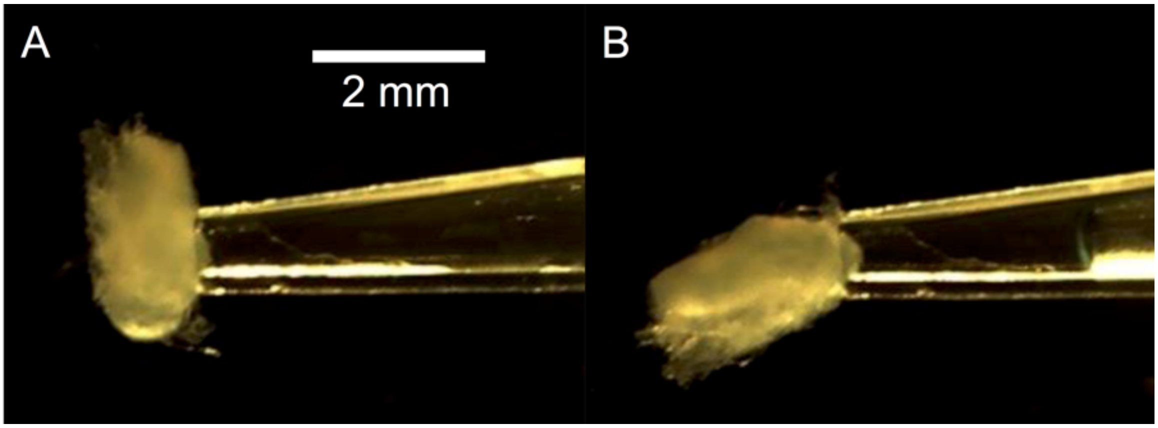

Figure 6.1: PC in two different MPA experiment pipette orientations. The PC was positioned with the micropipette parallel to its **(A)** short axis (SA) and **(B)** long axis (LA). The scale bar is the same for both images.

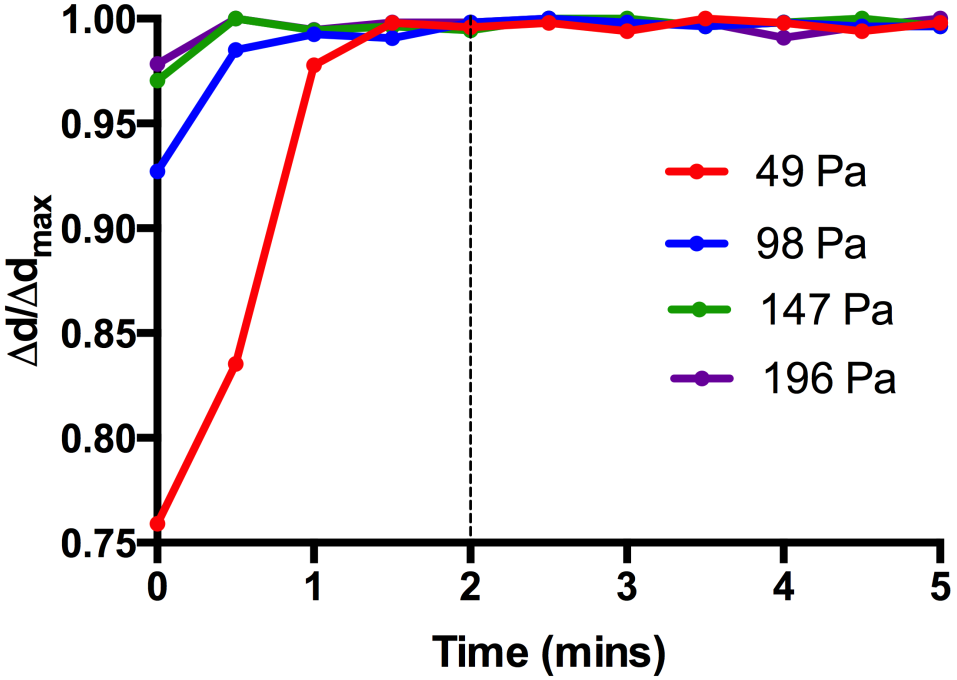

Figure 6.2: PC equilibration time experiment. The suction pressure was set between 49-196 Pa for 5 minutes and the protrusion length of the PC into the pipette was recorded at time intervals of 30 seconds. The ratio of the protrusion length change to the maximum recorded protrusion length change at each pressure (Δd/Δdmax) is plotted. A dashed, vertical line is drawn at 2 minutes, which was the time deemed sufficient to allow the PC to equilibrate with the applied pressure. After 2 minutes, Δd/Δdmax was greater than 0.99 for the four suction pressures tested in this equilibrium study.

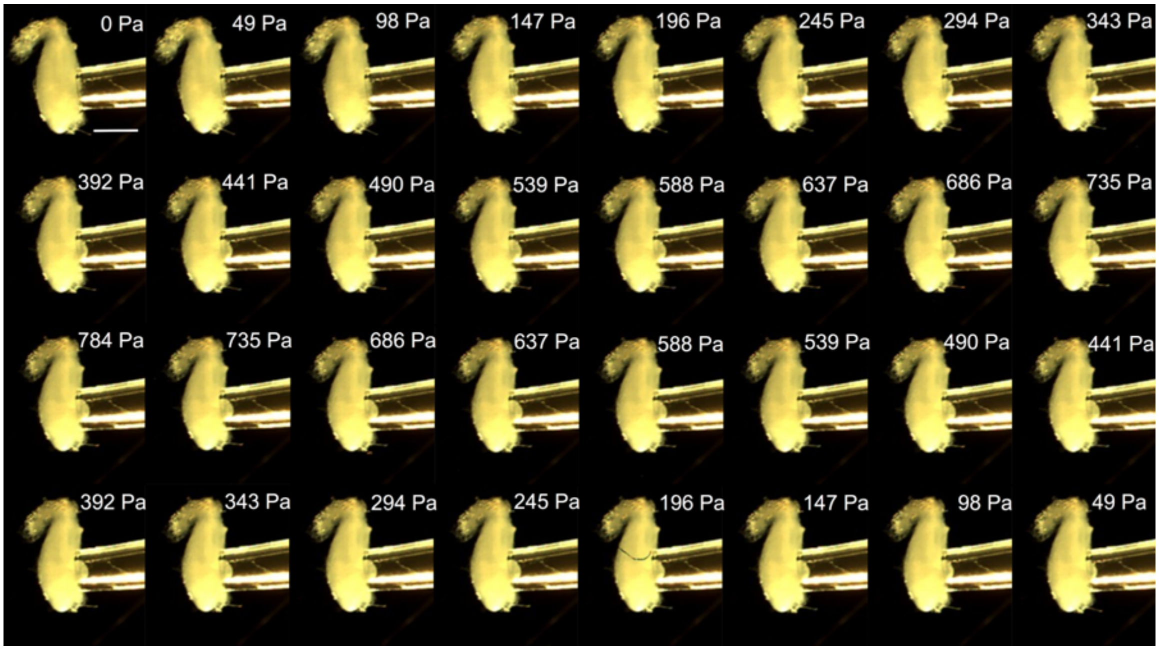

Figure 6.3: Time series of MPA images. Images acquired at each suction pressure for one representative PC in the SA orientation are shown. Suction pressure is written in the upper right hand corner of each image. The images are in the order of increasing followed by decreasing pressure trials. The scale bar in the 0 Pa image indicates 1 mm.

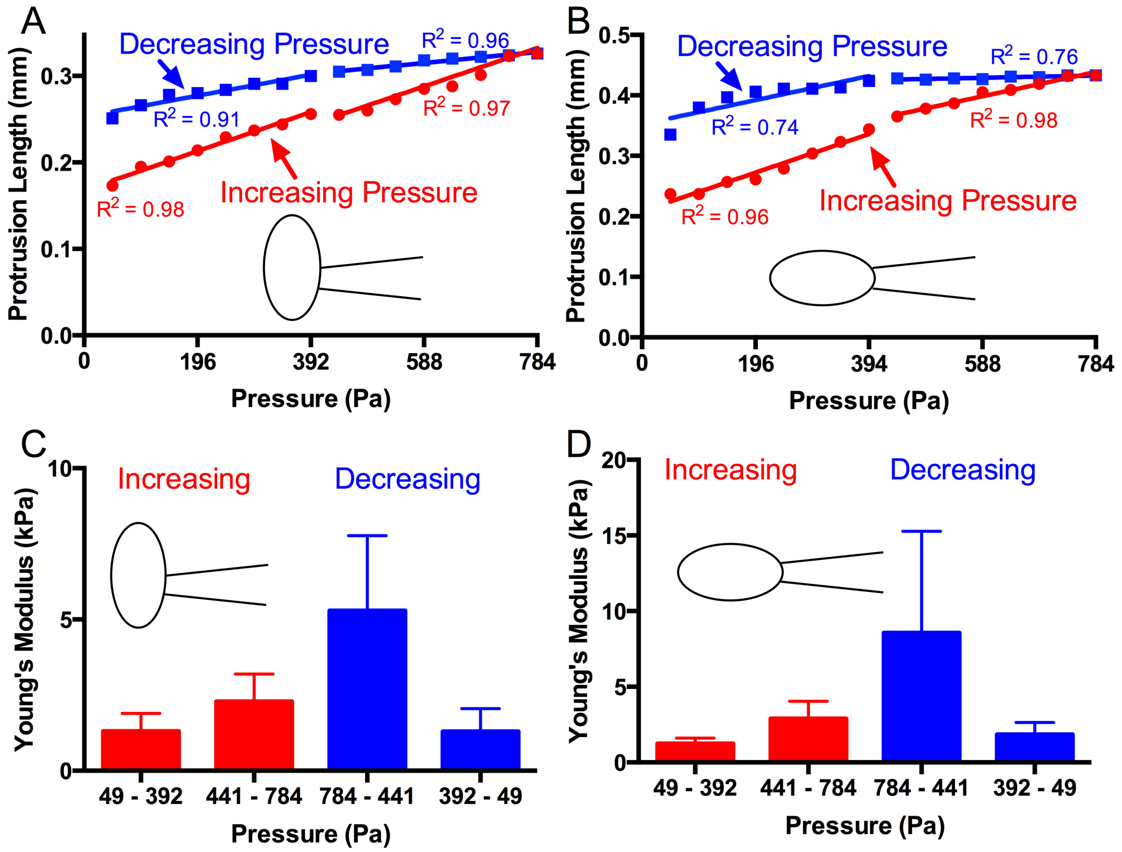

Figure 6.4: MPA results. (A) Average protrusion length vs. pressure for a representative PC with the pipette in the SA orientation (Figure 6.1A). Data points for increasing pressure trials are shown in red circles, with the lines of best fit for the low (49-392 Pa) and high (441-784 Pa) pressure regions plotted as solid red lines. Data points for decreasing pressure trials are shown in blue squares, with the lines of best fit for the low displacement and high displacement regions plotted as solid blue lines. **(B)** Average protrusion length vs. pressure for a representative PC with the pipette in the LA orientation (Figure 6.1B). **(C)** Average moduli calculated for the PCs (N=10) with the pipette in the SA orientation for low- and high- pressure regimes for increasing (red) and decreasing (blue) pressure trials. Error bars indicate the 95% confidence interval. **(D)** Average moduli calculated for the PCs (N=10) with the pipette in the LA orientation. Error bars indicate the 95% confidence interval.

CHAPTER 7: AN INTER-SPECIES ANALYSIS OF THE PACINIAN CORPUSCLE’S FREQUENCY SENSITIVITY

The content of this chapter is still in preparation. Only preliminary findings are reported.

7.1 Summary

The somatosensory systems of different species are specialized to the needs of the species. The location and structure of the PC and its avian-equivalent, the Herbst corpuscle (HC), can be fine-tuned to reflect the functional needs of an individual species. In this study, I performed a thorough literature search to compile the structural parameters of PCs and HCs from various species based on the availability of histological images. I then used the previously-derived equations [33] for peak frequency and bandwidth to predict these frequency responses of each species. Our preliminary findings show that frequency response does not correlate with animal size or class. These findings can be compared to experimentally-obtained frequencies sensitivities of various animals reported in the literature.

7.2 Introduction

Vibrotactile sensitivity across different groups of animals is fine-tuned to fit the needs of a specific species [192]. Different species rely on vibrotactile sensitivity for various purposes, such as hunting prey or detecting predators. The PC has been reported in species ranging from mammals to reptiles to amphibians and has been located in various anatomical locations, from the hands of humans [17] to the feet of elephants [78]. The PC’s avian equivalent, the Herbst corpuscle (HC), is found in the bill and other anatomical locations in birds [6,192]. The PC and HC show functional similarities but some structural differences, such as their inner core organization [6,18].

Corpuscles are used for hunting and catching prey in various species. The somatosensory organs of snakes are specialized to aid in hunting, as they must rely on their sense of touch to hunt and catch fish in complete darkness and may use vibrations of surrounding water to locate their prey [192,193]. Crocodiles also rely on their sense of touch to hunt in dark environments [192]. The star-nosed mole uses its star organ, which includes 22 mechanosensitive appendages (Eimer's organs) around the nostrils, to forage in muddy soil [194]. Each Eimer's organ is innervated by various mechanoreceptor units, including Pacinian-like corpuscles, and is the densest population of mechanosensitive end organs found in mammals [192,194,195].

Birds rely on tactile sensitivity within their skin and beaks or bills (rostrum). Birds that forage for prey, such as the kiwi and sandpipers, rely on their sense of touch in their bills to locate invertebrates in sand and soil via "remote touch", through which birds sense the vibrotactile signals of burrowing prey to locate them [192,196]. Anseriformes, which is an order of birds that includes ducks, geese, and swans, rely on their sense of touch to hunt in aquatic environments. Some species of ducks use "dabbling", during which they move their mechanosensitive bill back and forth in water, to forage [192].

The PCs of mammals are implicated in various functions depending on their anatomical location. The PCs of human and monkey hands are localized to areas necessary for gripping and tool manipulation [34]. Elephants are believed to use PCs located within their feet to sense low-frequency (20-40 Hz) seismic waves for long-distance communication [78]. It has been suggested that kangaroos and cats, with PCs located in their extremities, use PCs to sense ground vibrations, which could aid in the detection of predators [80].

The goal of this study was to use my previously-developed PC model [24,33] to predict functional differences between PCs and HCs of different species based on their structural differences. Specifically, peak frequency and bandwidth were analyzed via previously-derived equations [33] that predict these frequency responses from the structural parameters of the PC or HC outer core.

7.3 Methods

7.3.1 Modeling scheme

The previously published [24,33] three-stage model of the PC's mechano-to-neural transduction process presented in Chapters 3-5 was used to simulate the response of PCs to vibration. In Chapter 4, the Stage 1 model was run for various values of its five key structural parameters and equations were obtained for peak frequency (ω_{peak}, defined as the frequency of peak strain amplification) and bandwidth (B, defined as the frequency range over which strain amplification occurred) as a function of the following structural parameters: lamellar modulus (E), lamellar thickness (h), fluid viscosity (μ), PC outer radius (R_o), and number of lamellae (N). The following equations were obtained from this analysis:

$$\omega_{peak} = 1.605x10^{-6} N^{3.475} \frac{Eh}{\mu R_o} \tag{7.1}$$

$$B = 1.747x10^{-6} N^{3.951} \frac{Eh}{\mu R_o} \tag{7.2}$$

The structural parameters N, R_o, and h were collected for various animals as described below. The value for E was approximated to be 1.4 kPa, which is the apparent modulus value obtained from micropipette aspiration of human cadaveric PCs in Chapter 6 [116]. No experimental data has been obtained for the properties of the inter-lamellar fluid in PCs, so μ was approximated to be 3.5 mPa-s, or approximately 5 times that of water, as the viscosity value has been suggested to be 2-10 times that of water [32].

7.3.2 Species selection and PC structural analysis

A thorough literature search was performed to obtain the structural parameters of the PC's outer core required to run the model. Species were selected based on the availability of relevant data and quality of published histological figures. For the cat PC, the number of lamellae (N), lamellar thickness (h), and outer radius (R_o) were obtained from previously published findings [23,36]. All other species' properties were estimated in ImageJ [197] (U.S. National Institutes of Health, Bethesda, MD, USA, http://imagej.nih.gov/ij/, 1997-2017). N was counted by an observer and R_o and average h was measured using the provided scale bars for the obtained images. In the cases where a scale bar was not provided, R_o and average h were reported in terms of pixel quantity, as only the ratio between these measurements and not the actual values was necessary in Equations 7.1 and 7.2. The structural data obtained from each species and the relevant references are listed in Table 7.1 and shown in Figure 7.1. These parameters were used as inputs to Equations 7.1 and 7.2 to calculate ω_{peak} and B for each animal.

7.4 Results

The structural parameters listed in Table 7.1 were used as inputs to Equations 7.1 and 7.2 to calculate the frequency response properties of the corpuscles of various species. The values of ω_{peak} and B for each animal are shown in Figure 7.2. The data in Figure 7.2 are categorized by animal class. Despite their differences in mass, both reptiles analyzed in this study (snake and crocodile) have similar ω_{peak} values at 80.06 and 81.03 Hz, respectively (Figure 7.2A). There is no clear trend in ω_{peak} for the four birds analyzed in this study as the goose and rooster have similar masses (4.38 kg and 3.45 kg) but show large differences in peak frequency (62.62 Hz and 19.80 Hz). Finally, there is no relationship between animal mass and peak frequency for the mammals tested in this study, as the results show the star-nosed mole and gray whale, which have large differences in mass (55 g vs. 36 Mg) have similar peak frequencies at 46.67 Hz and 55.70 Hz.

7.5 Discussion

The frequency sensitivity results predicted by the model can be compared to experimental findings or observations reported in the literature. While the vibrotactile sensitivity of corpuscles within all species analyzed in this study has not been reported, experimentally-obtained frequency responses or hypothesized results have been reported for some species and are discussed below.

Electrophysiological recordings from trigeminal neurons of tentacled snakes showed maximum sensitivity and phase-locking with the stimulus in the 50-150 Hz frequency range in response to mechanical stimulation of the tentacles [198]. My results predict peak sensitivity of the PCs of Japanese-striped snake to be 80.05 Hz, which falls within the range reported for tentacled snakes.

Recordings from geese and ducks show sensitivity to vibrations between 50 and 1000 Hz [199,200]. The peak frequency of 62.62 Hz predicted in this study falls within the broad frequency range reported in the literature.

While the activity of PCs in the elephant foot has not been recorded, it is believed that PCs play a role in sensing the low frequency (20-40 Hz) seismic waves in the air and ground used by elephants for long-distance communication [78]. The results of this study, however, suggest that the peak frequency of elephant PCs is 1024.99 Hz, which is much greater than the low-frequency communication waves. However, the large bandwidth (5260.93 Hz) reported in this study suggests that elephant PCs may also have an effect at lower frequencies. The outer radius and number of lamellae in elephant PCs are on the same order of magnitude as smaller animals, such as the human and cat (Figure 7.1). If these properties were to scale with animal size, the peak frequency of elephant PCs would be much larger than 1024.99 Hz.

Electrophysiological recordings of isolated PCs from cat mesentery showed that the average peak frequency at which PCs fired 1 spike per stimulus cycle was 270 Hz [20]. My predicted peak frequency for the cat PC, 68.23 Hz, is less than the reported average frequency but on similar orders of magnitude.

While the peak frequency of isolated human PCs has not been reported, experiments by Brisben et al., [70] in which human subjects held a vibrating rod, reported peak frequencies between 150 and 200 Hz. My reported peak frequency for human PCs, 397.24 Hz, is larger than this value but is within the typical human sensitivity range for PCs [18,19].

The preliminary results presented in this chapter provide a first glance into a computational comparison of the frequency response of PCs and HCs in different species. Animals with masses spanning over five orders of magnitude were analyzed in this study. Despite such a large mass difference between the animals, PC and HC outer radii collected from histological images only spanned two orders of magnitudes and the number of lamellae ranged from 7-30. Therefore, the enormous range of animal sizes was not represented by an equally large span of PC properties. The predicted peak frequencies spanned two orders of magnitude, with the smallest predicted peak frequency (10.62 Hz) modeled for dog PCs and the largest (1024.99 Hz) modeled for elephant PCs. The results of this study show that animal size alone cannot be used to predict differences in PC or HC structure or peak frequency. Future work must be done to understand the physiological reasons behind the different frequency sensitivities of the species analyzed in this study and to validate the model with experimental findings.

Table 7.1: Animal and PC information

Animal	Species Name	Animal mass (kg)	Corpuscle radius (µm)	Number of lamellae	Lamellar thickness (µm)	Peak Frequency (Hz)	Bandwidth (Hz)	Ref.
Cat	Felis catus	4.04	255.6	30	0.2	68.23	374.91	[23,36]
Crocodile	Crocodylus niloticus	386	75.14	10	3.18	81.03	263.9	[201]
Dog[1]	Canis familiaris	46.5	1971.24	10	10.92	10.62	34.58	[202]
Elephant	Elephas maximus	4082	317.3	26	6.13	1024.99	5260.93	[78]
Emu	Dromaius novaehollandiae	37.9	61	15	1.77	226.99	896.71	[203]
Frog	Rana esculata	0.04	59.99	15	1.60	208.85	825.05	[204]
Goose	Anserini	4.38	33.83	9	1.60	62.62	193.99	[205]
Human	Homo sapien	62.1	190	28	1.1	397.24	2112.09	[24]
Kangaroo	Macropus giganteus	90.7	240.7	15	4.14	134.80	532.52	[80]
Star-nosed Mole	Condylura cristata	0.055	4.6	10	0.11	46.67	151.99	[206]
Monkey[1]	Ateles fusciceps	1.81	720.9	10	16.92	44.98	146.49	[207]
Mouse	Mus musculus	0.0193	54.67	12	2.77	183.15	650.59	[208]
Ostrich	Struthio camelus	107	37.51	7	3.20	47.39	130.26	[203]
Porpoise	Phocoena phocoena	54.4	18.6	10	0.89	91.30	297.36	[209]
Rat	Rattus	0.23	92.67	18	1.97	314.69	1355.85	[2]
Rooster[1]	Gallus gallus	3.45	203.8	8	4.57	19.80	57.98	[210]
Snake[1]	Elaphe quadrivirgata	0.33	977.6	18	5.30	80.06	344.93	[211–213]
Whale	Eschrichtius robustus	36000	74.02	9	3.10	55.70	172.55	[214]

---

[1] Outer radius and lamellar thickness reported in pixels

[2] Figure generously provided by Dr. Burak Güçlü (Bogaziçi University) for analysis

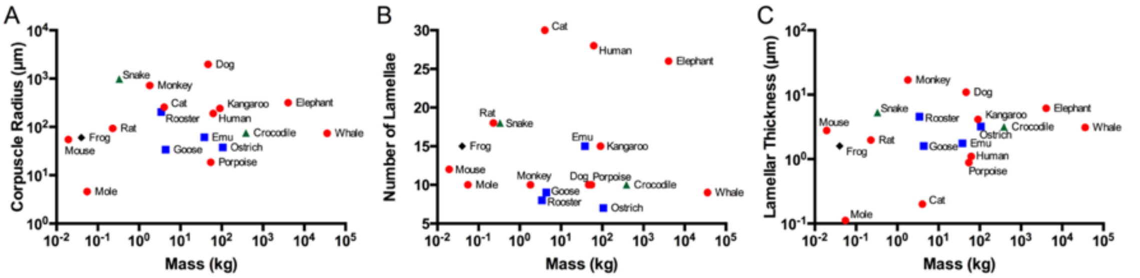

Figure 7.1: PC and HC structural parameters (R_o, N, h) for various species. (A) Corpuscle radius (R_o) vs. animal mass for the animals analyzed in this study. The color and shape of the data points reflect the class of each animal. Red circles indicate mammals, blue squares indicate birds, green triangles indicate reptiles, and black diamonds indicate amphibians. The name of each animal is listed next to the corresponding data point. **(B)** Number of lamellae (N) in the corpuscle outer core vs. animal mass. **(C)** Average lamellar thickness (h) vs. animal mass.

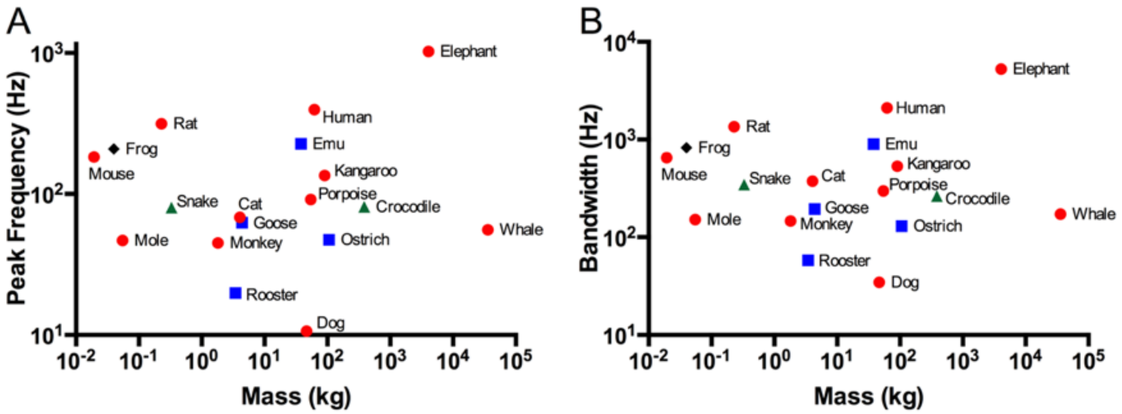

Figure 7.2: Peak frequency (ω_{peak}) and bandwidth (B) for various animals. (A) The peak frequency (ω_{peak}) calculated via Equation 7.1 for the animals listed in Table 7.1 vs. animal mass. The color and shape of the data points reflect the class of each animal. Red circles indicate mammals, blue squares indicate birds, green triangles indicate reptiles, and black diamonds indicate amphibians. The name of each animal is listed next to the corresponding data point. **(B)** Bandwidth (B) calculated via Equation 7.2 vs. animal mass.

CHAPTER 8: DISCUSSION AND CONCLUSIONS

8.1 Summary

The research presented in Chapters 2-7 of this dissertation focuses on computational and experimental characterization of the mechanical behavior of PCs. In my thesis research, I used computer modeling of single PCs (isolated or *in vivo*) or multiple PCs (*in vivo*) under steady-state or dynamic mechanical stimuli to model the mechanical and neural behavior of the receptor. I also performed experiments to characterize the steady-state mechanical behavior of single, isolated human cadaveric PCs, which not only provides insight into the mechanics of the receptor but can also be used to inform future models of PC mechanics.

8.2 Significance and broader impact

The major contributions of the research presented in this dissertation are comprehensive computer models of the entire mechano-to-neural transduction process of the PC. Both mechanical and neural models were developed to simulate various aspects of the PC's response to mechanical stimuli, providing insight into the effects of the PC's structural and mechanical properties on its behavior. The models developed in this dissertation captured and simulated the PC's response to instantaneous, vibratory, and sustained mechanical stimuli, which are all important mechanical regimes to consider in the study of the PC.

The two main models developed in this thesis, which are the multiscale modeled presented in Chapter 2 and the three-stage multiphysics model introduced in Chapter 3, were compared to mechanical [109] and neural [20] experimental data previously published in the literature. The multiscale model in Chapter 2 [115] was compared to experimental data published by Güçlü et al. [109] in which PCs isolated from cat mesentery were indented by cylindrical contactors with step waveforms. In their study, Güçlü et al. [109] compared the experimental displacements through the PCs to those obtained in finite-element simulations of an isotropic linear elastic ellipsoid, but their model was unable to capture the nonlinear trend of the experimental data. The multiscale model developed in Chapter 2, however, was able to capture the experimental data when circumferentially-aligned Delaunay networks were inserted into model to mimic the lamellae (Figure 2.4A). The neural output of the three-stage multiphysics model first introduced in Chapter 3 [24] was compared to Bolanowski and Zwislocki's [20] action potential firing rates recorded from cat mesenteric PCs stimulated with sinusoidal indentations at increasing displacements. Both experiments and simulations showed a U-shaped trend (Figure 3.9) of indentation displacement vs. frequency when reporting the indentation displacements required to initiate any neural firing (response threshold) and the displacements required to initiate firing at the indentation frequency (tuning threshold).

The research completed in this thesis resulted in detailed mechanical and neural models of the PC that can simulate the entire process through which a mechanical stimulus applied to the PC results in neural spiking. These models covered single and multiple PCs, isolated and embedded PCs, and accounted for the detailed structure of the PC to varying degrees. In addition, the first published mechanical experiments on human cadaveric PCs, as well as the first published experiments obtaining a force or stress measurement on a PC, were performed. The content of this thesis has greatly contributed to the PC literature by increasing our knowledge of the PC's mechano-to-neural transduction process. By understanding this process, we can also begin to characterize the mechanosensation of other receptors and nerve endings and to explore how hundreds of receptors in a single hand interact to send detailed sensory feedback to our somatosensory cortex and create our sensation of touch. Characterization of the PC and other mechanoreceptors on the single receptor level is critical to the scientific community's understanding of how a network of multiple receptors behaves on the whole-hand or whole-organ level. The emergence of the field of haptics and the need for better neural feedback systems [114] have exposed the urgent need for this fundamental understanding of mechanoreceptors. This research is therefore a necessary first step towards the development of haptic feedback-enabled prosthetics [114] and understanding the vibrotactile sensitivity associated with aging and diseases, such as diabetic peripheral neuropathy [90,91].

8.3 The PC as a multiscale structure

The study of the PC and vibrotactile sensitivity is a multiscale problem that can be analyzed on various levels with distinct length scales and tissues of interest. While most the work presented in this thesis focused on the PC at the single-receptor level, the PC can also be studied at the channel level, multi-receptor level, and whole-hand level. The following sections discuss the current state of research at these different scales and what the research presented in this thesis means in the context of each field.

8.3.1 The channel level (~nm)

The PC's neurite contains various types of ion channels responsible for its neural functioning. Ion channels have also been identified on the non-neuronal cells of the PC's inner core. Acid-sensing ion channels (ASICs), which belong to the degenerin/epithelial sodium channel (DEG/ENaC) superfamily and are non-voltage gated channels, are expressed in sensory neurons and have been proposed to play a role in mechanotransduction [42,150–152]. Immunohistochemical studies on the presence of ASICs in PCs identified ASIC1 protein expression in the neurites of human PCs [153] and ASIC2 expression in the neurites and inner core lamellar cells of human and murine PCs [152–154], which has also been detected in human Merkel cells and Meissner corpuscles [154]. The role of ASIC2 in PC transduction remains unclear, as ASIC2 knockout in mice did not significantly alter cutaneous mechanosensation [155], but the presence of these channels in low-threshold mechanoreceptors suggests a role in mechanotransduction [154]. Immunocytochemical studies have also detected voltage-gated sodium and potassium channels [40] and positive labeling for glutamate and glutamate receptors [26] on the inner core lamellar cells of the cat PC.

The localization of ASIC2, voltage-gated channels, and glutamate on the non-neuronal cells of the inner core suggest a possible chemical involvement of the inner core in mechanotransduction. The lamellae of the inner core are believed to be specialized Schwann cells [7,43,49], but no patch-clamp experiments have been performed on these cells to characterize their electrical activity. In the models presented in this thesis, the inner core was treated as a purely mechanical component of the PC as the chemical involvement of the inner core in the PC's transduction process is unknown.

The mechanically-gated channels of the PCs have not been studied at the single channel level. Very little is known about the specific properties of these channels, despite their role in the PC's mechanotransduction process. Their location is hypothesized to be at the bases of filopodial projections on the neurite's membrane [27,43,46], as discussed in

Section 1.2.1.1. While the properties of Pacinian mechanosensitive channels have not been studied, the mechanosensitive channels of many other tissues, such as rat DRG neurons [144], chick skeletal muscle [215] and crayfish receptor organs [216], have been probed. In the absence of data on the mechanically-gated Pacinian channels, published research on other channels [144] was used to convert measured strains on the neurite membrane into an injectable current in the three-stage model introduced in Chapter 3 [24]. A sigmoidal activation curve was constructed based on the activation time constants of a rapidly relaxing current in rat DRG sensory neurons [144] for the conversion of strain to current. While many other channels could have been selected as the PC analogue in this study, the activation curves published by Hao and Delmas were selected based on their rapid relaxation. A slowly-adapting type 1 (SA-1) receptor model by Lesniak and Gerling [110] also used a sigmoidal function to convert the strain energy density of the receptor into receptor current, and fit the parameters of their function to reproduce *in vivo* SA-1 firing rates. Experiments on the mechanosensitive channels of the PC and other receptors are necessary to provide information about the relationship between the receptor mechanics and its current.

8.3.2 The single PC level (~µm-mm)

The PC has been studied extensively on the single-receptor level in both experimental and computational approaches. Previous electrophysiological experiments on cat mesenteric PCs have probed the neural responses (action potentials and receptor potentials) of PCs in response to vibratory [20,21] and sustained [11] mechanical stimuli. Experiments by Hubbard [10] in 1958 and later by Güçlü [109] in 2006 analyzed the displacement of lamellae in response to compression of the PC outer surface, and these data were later modeled in published computational studies [23,109,115].

Many experimental investigations into the PC have focused on microscopy of the PC's inner structure, specifically the neurite's shape and lamellar organization. Early experiments involved microscopy of the PC's outer and inner cores [36,46] and neurite [35,36], which have resulted in very detailed descriptions of the inner structure of cat mesenteric PCs. Recent work by Pawson et al. used immunocytochemistry to identify proteins [43] and neurotransmitters [26,27] located on the PC's lamellae and neurite and draw conclusions about their possible involvement in the PC's mechanotransduction.

As mentioned throughout this thesis, previous computational studies have created detailed models of the mechanics and/or neuronal response of single mechanoreceptors, including Merkel cells [110], Meissner corpuscles [107], and PCs [24,32]. Single-PC models have examined different aspects of the PC's structure, including the interaction between fluid and lamellar layers [23,32], the concentric arrangement [115] and number [24,32] of lamellae in the PC's capsule, the PC's ellipsoidal shape [109], and the PC's depth within the skin [115].

These published models have greatly informed the scientific community of mechanoreceptor behavior, but they have limitations that must be considered in their interpretation. The isotropic PC modeled developed by Güçlü et al. [109], for example, considered the shape of the PC but did not account for its detailed inner structure. The limitations of Güçlü et al.'s model in capturing experimental displacement trends through the PC were overcome in Chapter 2. By modeling an ellipsoidal PC with concentric collageneous layers [115], I was able to simulate Güçlü et al.'s experimental data and specifically capture the nonlinear trend in displacement as a function of distance into the PC's core.

While some models of PC mechanics, such as the model originally developed by Loewenstein and Skalak [23] and later extended by Biswas et al. [124], did account for the PC's layered structure, these models had other limitations such as the overall shape of the PC, which was modeled as a cylinder, or failing to account for the geometry of the inner neurite. The modeled developed by Holmes and Bell [28,29] used a two-dimensional approach to analyze the PC, and Grandori and Pedotti [108] employed a series of transfer functions to simulate the receptor potential generated in the PC's neurite. These models have contributed to the understanding of the PC and other mechanoreceptors but they have not been able to unify various characteristic properties of the PC, such as the geometry of its lamellae and neurite and the behavior and location of its stretch-gated ion channels, into a single, comprehensive model. The major contributions to the modeling of single PCs arising from the research presented in Chapters 2-7 of this dissertation are discussed in the subsequent paragraphs.

The research presented in this thesis modeled the three-dimensional structure of the PC and its neurite. While the PC was modeled as an ellipsoid in Chapter 2 [115], the overall shape of the PC was modeled as a sphere in Chapters 3-5 and 7 [24,33] to reduce the dimensionality of the problem. Studies by Loewenstein and Skalak [23] and Biswas et al. [124] modeled the PC outer core as a series of cylinders, which represents one limit of the PC's shape, while the spherical model described in this dissertation represents the other. The PC's shape is ellipsoidal, which falls somewhere between these two limits. While the PC is not spherical, modeling it as a series of spheres greatly reduced computational time and complexity. The model presented in Chapters 3-5 can be expanded to account for the ellipsoidal shape of the PC, but these spherical models provide us with important results that can be considered as a contrast to the results of the published cylindrical models. Additionally, while the shape of the PC is more ellipsoidal than spherical, it has been shown that the ellipsoidal shape alone does not affect the displacement through the PC in static indentation simulations [109].

The three-dimensional structure of the neurite is also important to consider in modeling the PC. No previous model of the PC has accounted for the neurite's geometry, including the filopodia, which are hypothesized to be the location of mechanogated cation channels [27,43,46] and are therefore critical to the mechano-to-neural transduction of the receptor. Due to our ability to model the entire geometry of the neurite, I was able to place three filopodia at the terminal region of the neurite and two filopodia jutting into the cleft at the central region of the neurite [18,45] and observe the resulting high strains at the filopodial bases in the simulations. Incorporating the detailed morphology of the neurite in the model allowed me to observe the mechanical influence of the filopodia and its effect on the neurite strain, which governs the behavior of the mechanogated channels. The model presented in Chapters 3-5 also allowed for quantification of strain amplification from the PC surface to the location of mechanogated channels on the neurite and the three-dimensional distribution of this strain. This model is the first to account for the structure of the neurite or the mechanical influence of filopodia, both of which are critical to the PC's mechano-to-neural transduction process.

The research presented in Chapter 6 is the first published study to probe the mechanics of isolated human PCs, and the first published measurement of an apparent

Young's modulus for the receptor. Prior to this project, there was no published study of PC mechanics that included an actual force or stress measurement. Bell et. al [18] stated that the Young's modulus of the PC was measured at 1 kPa and cited a conference abstract as the source of this measurement [125]. That abstract, however, did not include a value or any experimental data. A range of values from 1 kPa to 100 MPa has been used to approximate the PC's stiffness in published theoretical models [23,30,109,124]. It was therefore necessary to perform a mechanical characterization study on isolated PCs to address this gap in the literature. Through micropipette aspiration, I measured an apparent Young's modulus for isolated human cadaveric PCs, which was on the single kPa scale and on the same order of magnitude as the value attributed to Pietras and Bolanowski [125] and the estimates used in recent models [30,109,124]. Obtaining an approximation for the stiffness of the PC is a step towards understanding the mechanics of the receptor and producing more accurate simulations of PC dynamics, as well as addressing an unanswered question in the PC literature.

The apparent modulus measured in Chapter 6 represents an important aspect of the PC's mechanical response, but the analysis required that the PC be considered a solid ellipsoid. The PC's core is not completely solid and is composed of a series of lamellae separated by fluid, so more complex models require a value for the modulus of each individual lamellar layer in order to simulate the fluid-lamellae interaction. The study performed in Chapter 4 was the first to analyze the effect of varying the Young's modulus of the lamellae, in addition to other properties such as lamellar thickness, number of lamellae, and outer PC radius. In this study, I derived dimensionless equations relating these properties to the peak frequency and bandwidth of my simulated PC. Simulations showed that increasing the lamellar modulus increased the peak frequency and bandwidth. The results of this study are especially important when considering diseases such as diabetes that can affect vibrotactile sensation. Structural changes in PCs with diabetes [93,94], as well as vascular [97–100] and tissue [101–103] stiffening that occurs as a result of advanced glycation, may cause changes in the lamellar modulus that would affect the PC's frequency response. The sensitivity of the PC's frequency response to lamellar modulus highlights the importance of obtaining correct approximations for the mechanical and structural properties of the PC capsule.

The results presented in Chapter 7 show that the PC's frequency response is also sensitive to the structural parameters of the PC. In this study, I used equations developed in Chapter 4 to compare the simulated frequency response of PCs and HCs in various species. While the masses of the various species tested spanned a range of five orders of magnitude, the outer radii of the corpuscles as measured in histological images spanned two orders of magnitude. The simulated peak frequencies also spanned two orders of magnitude. Therefore, while PC frequency sensitivity cannot be predicted from animal size alone, it is extremely sensitive to the structural properties of the corpuscle.

While models and studies on isolated PCs can provide great insight into the behavior of the receptor, there is a significant gap in the literature on the PC's *in vivo* response to tactile stimuli. The PC resides deep within the dermis and subcutaneous tissues [17,34,54–56], as well as in other anatomical regions. Isolated PC models cannot account for the mechanical effect of the surrounding skin or tissue on the PC's mechanical or neural response. In the only previously-published study of an embedded PC, Biswas et al. [30] used transfer functions to relate compression of the outermost layer of a PC to compression of skin. In Chapter 5, I embedded my 3D mechanical-to-neural PC model in a finite-element model of human skin to model the mechanical effects of skin on PC's response to vibration.

8.3.3 The multi-receptor level (~mm)

There has been a great deal of advanced modeling approaches taken to simulate single mechanoreceptors, which have the benefit of informing us of the detailed mechanical and neural mechanisms that govern the specific receptor's behavior. However, receptors are not isolated *in vivo* and co-exist with three other types of cutaneous mechanoreceptors in the skin. Mechanical stimuli may reach and excite more than one receptor in the skin. In addition, while each of the four main types of mechanoreceptors is tuned to respond to a specific type of mechanical stimulus from light touch to pressure to vibrations, a single stimulus may excite more than one type of mechanoreceptor. In fact, most physical actions excite more than one type of mechanoreceptor, so the somatosensory cortex often receives input from a population containing multiple afferent subtypes [82]. Johansson and Vallbo [22] classified the proportions of the four main mechanoreceptive subtypes in the human hand and identified that PCs made up 15% of the sampled population. The PC is therefore surrounded by Meissner corpuscles, Merkle cells, and Ruffini corpuscles, which may respond to components of the same mechanical stimuli that excite the PC. Therefore, it is often necessary to model PCs and other mechanoreceptors on the multi-receptor level in order to better understand the *in vivo* response of the somatosensory system.

In 1982, Freeman and Johnson developed a simple receptor model [104,105] consisting of an electrical circuit to match neural data collected from slowly adapting (SA), rapidly adapting (RA), and Pacinian afferents in the macaque monkey hand in response to skin vibration. Their basic model contained 4 degrees of freedom, which were fit to the neural data from the three different mechanoreceptors (SA, RA, PC). Their analysis and model fitting focused on the temporal structure of the afferent discharge, including overall firing patterns and impulse phase [104], and the stimulus-response functions that relate neural discharge to vibratory amplitude at different frequencies [105]. Instead of implementing individual, complex models for each mechanoreceptor, Freeman and Johnson modeled different receptors by adjusting a few parameters within a single model. The Freeman-Johnson model was later extended by Slavik and Bell [106], who introduced hyperexcitability and an absolute refractory period following each action potential to improve the model's fidelity to neural data. These studies on the multi-receptor level enabled the authors to model how multiple, rather than one, mechanoreceptor would respond to various stimuli.

Recent work by the Bensmaia group has also focused on modeling the response of a population of mechanoreceptive afferents to a range of mechanical stimuli. Muniak et al. [4] first performed neurophysiological experiments to characterize the spiking responses of a population of afferents (SA type 1, RA, and PC) of macaque monkeys to various mechanical stimuli. In their study, they set out to determine the underlying neural codes representing the population response and the corresponding weights of each afferent type in the hypothesized neural codes. Kim et al. [217] then fit an integrate-and-fire model to this data to predict the spike timing of each of the three afferent subtypes in response to vibration. The resulting model captured the behavior of the neurophysiological data and showed how each receptor subtype responds to different components of a single stimulus.

Dong et al. [218] later improved upon this model by reducing complexity and introducing a saturating component.

These functional models can simulate the responses of an afferent population to arbitrary mechanical stimuli, but do not explain the underlying behavior of each individual receptor. Mechanistic individual receptor models, such as those introduced in Chapters 2 and 3, focus on the physical mechanisms that govern the receptor's behavior. The detailed single receptor models that have been developed for different receptors, from the PC models discussed in this thesis to the Meissner corpuscle model developed by Bensmaia [107] to the SA-1 models of Gerling [110,219], inform us of the detailed mechanical and neural components that govern the response of each receptor to its preferred mechanical stimuli. These models, however, are too computationally-intensive to be combined into a multi-receptor model and cannot provide the population response to a stimulus. There are therefore tradeoffs between the complexity of a single receptor model and the robustness of a multi-receptor approach.

8.3.4 The whole hand level (~cm)

The largest level on which the PC can be studied is the whole-hand level, which models the activity of a population of afferents embedded within the hand. The whole-hand level accounts for the mechanics of the hand so that the embedded mechanoreceptors are deformed based on the transmission of the stimulus through the skin. The whole-hand level enables researches to analyze the population response to more natural and complex touch stimuli, such as texture scanning, edge detection, and the direction of motion.

A recent model by Saal et al. [174] analyzed the response of a population of mechanoreceptors embedded within the hand at their relative densities within human skin.

The palm or fingertips of their modeled hand were stimulated, and the mechanoreceptors were then deformed based on the estimated resulting stress at each receptor's location. The authors were able to compare the results of their model to population responses in the literature. A major benefit to the whole-hand level of mechanoreceptor modeling is the ability to compare simulated data to neurophysiological data resulting from skin stimulation and test more physiologically-relevant tactile stimuli. Whole-hand models of mechanoreceptors can enable researchers to simulate the neural response to natural actions, such as tool manipulation and grasping, which can have direct implications in the fields of haptics and prosthetics.

Shao et al. [148] mapped the spatial distribution of vibrations as they propagate across the surface of skin in the hand, which is a process that lasts on the millisecond time scale. Their results suggest that vibrotactile waves that propagate across the entire hand, and not just at the point of stimulation, can provide information about the stimulus. Therefore, PCs and mechanoreceptors within the entire hand, and not just directly under the indenter, can be excited by a mechanical stimulus or contact with an object and must be accounted for to truly capture the population response.

The mechanics of skin, bone, and the soft tissues of the hand can affect wave propagation both across the hand (perpendicular to a stimulus) and through the skin (parallel to the stimulus) and must be incorporated into a whole-hand model to capture the response to a skin-surface stimulus. The model presented in Chapter 5 introduces this idea and, while it only models two PCs within the skin, expands the mechano-to-neural PC model of Chapter 3 to a more physiologically-relevant domain.

8.4 Future directions

Computational and experimental future directions for this research are discussed in the following sections.

8.4.1 Computational

The three-stage multiphysics model [24] introduced in Chapter 3 approximated the outer core geometry as a series of concentric spheres, rather than cylinders [23,32]. As mentioned previously, however, the lamellae form layers that are more ellipsoidal than spherical, giving the PC its characteristic ellipsoidal shape. A previous study by Güçlü et al. [109] hypothesized that the PC's ellipsoidal shape alone was not responsible for the transmission of displacements through the receptor in static indentation tests, which suggested that modeling our PC as spherical rather than ellipsoidal may not have had a large effect on the overall results of the study presented in Chapter 3. For future studies, however, it is necessary to model the outer core as presented in Chapter 3 with the equations for ellipsoidal, rather than spherical, shells. This can be completed by altering Equations 3.1-3.31 [24] in a MATLAB finite-element model or by constructing a comparable model in COMSOL Multiphysics.

An ellipsoidal model of the PC's lamellae will allow for the study of directional sensitivity within the PC. Previous experiments by Ilyinsky [177] and Nishi and Sato [132] on isolated PCs demonstrated that, after 90° rotation along the PC's long axis, the tested PC's depolarizing receptor potential during compression was shifted to a hyperpolarizing response and vice versa. This functional asymmetry was later simulated in the transfer function PC model by Grandori and Pedotti [108], which showed similar trends in receptor potentials after 90° rotation of the PC, with the PC stimulated perpendicular to its long or short axis. While this rotation is within the scope of the spherical model, the model cannot account for differences in the length of these axes. These previous studies [108,132,177] hypothesized that this directional sensitivity is due to the ellipsoidal shape of the PC or the ellipsoidal cross section of the neurite, as stimulation along different axes of the PC produces different deformations of the inner neurite, which results in changes in membrane potential. An ellipsoidal model of the PC will allow for further investigation of the PC's directional sensitivity by providing both a mechanical and neural analysis of this phenomenon.

An ellipsoidal PC model will also allow for a study of the effect of size and outer dimensions on the PCs response. PC size can vary with age [89] and disease [74] or between anatomical locations within an individual [16]. Specifically, short and long axis diameters can vary between locations, as shown in different regions of the fingers and palm of monkey hands [34]. An ellipsoidal PC model will allow for investigation of the different mechanical and neural responses of PCs with varying length aspect ratios, which is not possible with the current spherical model.

8.4.2 Experimental

There is a need for further microstructural characterization of PCs within the human hand. Stark et al. [17] published a study on the distribution of PCs within ten cadaver hands. While this study presented mean numbers of PCs within various areas of the finger and palm, the authors did not present detailed reports on the length dimensions of these PCs. There is therefore a need to characterize both the distribution and the dimensions of PCs in the human hand. This size distribution can also be characterized at different ages and disease states to investigate the effect of age and disease on the size and distribution of PCs in the hand. There is also a need for microstructural characterization on PC clusters within the hand. The relative sizes of PCs within a cluster, as well as their proximity and orientation with respect to the other receptors in the cluster, would provide key information on PC clustering. A microstructural study on PC clustering will greatly inform models of clusters and allow for the study of directional tuning within a PC cluster.

The micropipette aspiration experiments performed in Chapter 6 probed the mechanics of the PC under steady-state conditions. The PC responds to frequencies in the 20-1000 Hz range [20,190], and therefore behaves on a millisecond time scale. It is necessary to perform mechanical experiments on the PC's response to dynamic stimuli to further characterize the receptor's properties and understand how it responds to vibrations *in vivo*. The PC contains alternating layers of fluid and solid lamellae, which makes it viscoelastic. Dynamic experiments must therefore be completed to probe this viscoelasticity and understand the role of the fluid component in the PC's dynamic behavior.

8.5 Conclusion

The research presented in this thesis is a significant contribution to the PC and mechanoreceptor literature. This work involved mechanical and neural models of the PC under steady-state and vibratory stimuli and provided the first reported Young's modulus for the receptor. The research drew from fundamental mechanics, basic neuroscience and neurobiology, computer modeling, and mechanotransduction and applied principles from these areas to study the PC, resulting in a truly multiphysics and multidisciplinary analysis of the receptor. While there remains much to be done in the study of vibration sensation and mechanoreceptors, this research provides a far-reaching and innovative exploration into the fundamental science of the PC.

REFERENCES

[1] Abraira, V. E., and Ginty, D. D., 2013, “The Sensory Neurons of Touch,” Neuron, **79**(4), pp. 618–639.

[2] Johnson, K. O., 2001, “The Roles and Functions of Cutaneous Mechanoreceptors,” Curr. Opin. Neurobiol., **11**(4), pp. 455–61.

[3] Bolanowski, S. J., Gescheider, G. a, Verrillo, R. T., and Checkosky, C. M., 1988, “Four channels mediate the mechanical aspects of touch.,” J. Acoust. Soc. Am., **84**(5), pp. 1680–1694.

[4] Muniak, M. A., Ray, S., Hsiao, S. S., Dammann, J. F., and Bensmaia, S. J., 2007, “The Neural Coding of Stimulus Intensity: Linking the Population Response of Mechanoreceptive Afferents with Psychophysical Behavior,” J. Neurosci., **27**(43), pp. 11687–11699.

[5] Johnson, K. O., 1974, “Reconstruction of population response to a vibratory stimulus in quickly adapting mechanoreceptive afferent fiber population innervation glabrous skin of the monkey,” J. Neurophysiol., **37**(1), pp. 48–71.

[6] Iggo, A., and Andres, K. H., 1982, “Morphology of cutaneous receptors.,” Annu. Rev. Neurosci., **5**, pp. 1–31.

[7] Munger, B. L., and Ide, C., 1988, “The Structure and Function of Cutaneous Sensory Receptors,” Arch Histol Cytol, **51**(1), pp. 1–34.

[8] Jones, L. A., and Smith, A. M., 2014, “Tactile sensory system: encoding from the periphery to the cortex.,” Wiley Interdiscip. Rev. Syst. Biol. Med., **6**(3), pp. 279–87.

[9] Zimmerman, A., Bai, L., and Ginty, D. D., 2014, "The gentle touch receptors of mammalian skin," Science (80-.)., **346**(6212), pp. 950–954.

[10] Hubbard, S. J., 1958, "A Study of Rapid Mechanical Events in a Mechanoreceptor," J. Physiol., **141**, pp. 198–218.

[11] Loewenstein, W., and Mendelson, M., 1965, "Components of Receptor Adaptation in a Pacinian Corpuscle," J. Physiol., **177**, pp. 377–397.

[12] Shanthaveerappa, T. R., and Bourne, G. H., 1963, "New observations on the structure of the pacinian corpuscle and its relation to the perineural epithelium of peripheral nerves," Am. J. Anat., **112**(1), pp. 97–109.

[13] Bentivoglio, M., and Pacini, P., 1995, "Filippo Pacini: A determined observer," Brain Res. Bull., **38**(2), pp. 161–165.

[14] Pacini, F., 1835, "Sopra un particolare genere di piccoli corpi globosi scoperti nel corpo umano da Filippo Pacini, Alumno interno degli Spedali riuniti di Pistoria," Lett. to Accad. Medico-Fisica di Firenze.

[15] Pacini, F., 1840, Nuovi organi scoperti nel corpo umano, Tipografia Cino, Pistoria.

[16] Cauna, B. Y. N., and Mannan, G., 1958, "The Structure of Human Digital Pacinian Corpuscles (Corpuscula Lamellosa) and Its Functional Significance," J. Anat., **92**(1), p. 1–20.4.

[17] Stark, B., Carlstedt, T., Hallin, R., and Risling, M., 1998, "Distribution of Human Pacinian Corpuscles in the Hand: A Cadaver Study," J. Hand Surg. [Br], **23**(3), pp. 370–372.

[18] Bell, J., Bolanowski, S., and Holmes, M. H., 1994, "The Structure and Function of Pacinian Corpuscles: A Review," Prog. Neurobiol., **42**(1), pp. 79–128.

[19] Talbot, W., Darian-Smith, I., Kornhuber, H., and Mountcastle, V., 1968, “The Sense of Flutter-Vibration: Comparison of the Human Capacity With Response Patterns of Mechanoreceptive Afferents from the Monkey Hand,” J. Neurophysiol., **31**, pp. 301–334.

[20] Bolanowski, S. J., and Zwislocki, J. J., 1984, “Intensity and Frequency Characteristics of Pacinian Corpuscles. I. Action Potentials,” J. Neurophysiol., **51**(4), pp. 793–811.

[21] Bolanowski, S. J., and Zwislocki, J. J., 1984, “Intensity and Frequency Characteristics of Pacinian Corpuscles. II. Receptor Potentials,” J. Neurophysiol., **51**(4), pp. 812–830.

[22] Johansson, R., and Vallbo, A. B., 1979, “Tactile Sensibility in the Human Hand: Relative and Absolute Densities of Four Types of Mechanoreceptive Units in Glabrous Skin,” J Physiol, **286**, pp. 283–300.

[23] Loewenstein, W., and Skalak, R., 1966, “Mechanical Transmission in a Pacinian Corpuscle. An Analysis and a Theory,” J. Physiol., **182**, pp. 346–378.

[24] Quindlen, J. C., Stolarski, H. K., Johnson, M. D., and Barocas, V. H., 2016, “A Multiphysics Model of the Pacinian Corpuscle,” Integr. Biol., **8**, pp. 1111–1125.

[25] Nishi, K., Oura, C., and Pallie, W., 1969, “Fine structure of Pacinian corpuscles in the mesentery of the cat,” J. Cell Biol., **43**, pp. 539–552.

[26] Pawson, L., Pack, A. K., and Bolanowski, S. J., 2007, “Possible glutaminergic interaction between the capsule and neurite of Pacinian corpuscles,” Somatosens. Mot. Res., **24**(June), pp. 85–95.

[27] Pawson, L., Prestia, L. T., Mahoney, G. K., Güçlü, B., Cox, P. J., and Pack, A. K.,

2009, “GABAergic/Glutamatergic-Glial/Neuronal Interaction Contributes to Rapid Adaptation in Pacinian Corpuscles,” J. Neurosci., **29**(9), pp. 2695–705.

[28] Holmes, M. H., and Bell, J., 1990, “A Model of a Sensory Mechanoreceptor Derived From Homogenization,” SIAM J. Appl. Math., **50**(1), pp. 147–166.

[29] Bell, J., and Holmes, M., 1992, “Model of the Dynamics of Receptor Potential in a Mechanoreceptor,” Math. Biosci., **110**(2), pp. 139–74.

[30] Biswas, A., Manivannan, M., and Srinivasan, M., 2013, “A Biomechanical Model of Pacinian Corpuscle and Skin,” Proc Biomed Sci Eng Conf, pp. 1–4.

[31] Biswas, A., Manivannan, M., and Srinivasan, M. A., 2014, “Nonlinear Two Stage Mechanotransduction Model and Neural Response of Pacinian Corpuscle,” Proc. Biomed. Sci. Eng. Conf., pp. 1–4.

[32] Biswas, A., Manivannan, M., and Srinivasan, M. A., 2015, “Multiscale Layered Biomechanical Model of the Pacinian Corpuscle,” IEEE Trans. Haptics, **8**(1), pp. 31–42.

[33] Quindlen, J. C., Güçlü, B., Schepis, E. A., and Barocas, V. H., 2017, “Computational Parametric Analysis of the Mechanical Response of Structurally Varying Pacinian Corpuscles,” J. Biomech. Eng., **139**(7), pp. 71012-71012–9.

[34] Kumamoto, K., Senuma, H., Ebara, S., and Matsuura, T., 1993, “Distribution of Pacinian Corpuscles in the Hand of the Monkey, Macaca fuscata,” J. Anat., **183**, pp. 149–54.

[35] Quilliam, T., and Sato, M., 1955, “The Distribution of Myelin on Nerve Fibres From Pacinian Corpuscles,” J. Physiol., **129**, pp. 167–176.

[36] Pease, D., and Quilliam, T., 1957, “Electron Microscopy of the Pacinian Corpuscle,”

J. Biophys. Biochem. Cytol., **3**, pp. 331–342.

[37] Gray, J., and Sato, M., 1953, “Properties of the receptor potential in Pacinian corpuscles,” J. Physiol., **122**, pp. 594–607.

[38] Diamond, J., Gray, J. A. B., and Sato, M., 1956, “The site of initiation of impulses in Pacinian Corpuscles,” J. Physiol., **133**, pp. 54–67.

[39] Loewenstein, W., and Rathkamp, R., 1958, “The sites for mechano-electrical conversion in a Pacinian corpuscle,” J. Gen. Physiol., **41**(6), pp. 1245–1265.

[40] Pawson, L., and Bolanowski, S. J., 2002, “Voltage-gated sodium channels are present on both the neural and capsular structures of Pacinian corpuscles,” Somatosens. Mot. Res., **19**(3), pp. 231–237.

[41] Hodgkin, A. L., and Huxley, A. F., 1952, “A Quantitative Description of Membrane Current and its Application to Conduction and Excitation in Nerves,” J. Physiol., **117**, pp. 500–544.

[42] Vega, J. A., García-Suárez, O., Montaño, J. A., Pardo, B., and Cobo, J. M., 2009, “The Meissner and Pacinian Sensory Corpuscles Revisited New Data From the Last Decade,” Microsc. Res. Tech., **72**, pp. 299–309.

[43] Pawson, L., Slepecky, N. B., and Bolanowski, S. J., 2000, “Immunocytochemical identification of proteins within the Pacinian corpuscle,” Somatosens. Mot. Res., **17**(2), pp. 159–170.

[44] Ide, C., 1976, “The fine structure of the digital corpuscle of the mouse toe pad, with special reference to nerve fibers,” Am. J. Anat., **147**, pp. 239–356.

[45] Ide, C., and Hayashi, S., 1987, “Specializations of plasma membranes in Pacinian corpuscles: implications for mechano-electric transduction,” J Neurocytol, **16**, pp.

759–773.

[46] Spencer, P. S., and Schaumburg, H. H., 1973, “An ultrastructural study of the inner core of the Pacinian corpuscle,” J Neurocytol, **2**, pp. 217–235.

[47] Hudspeth, A. J., 1985, “The cellular basis of hearing: the biophysics of hair cells.,” Science (80-.)., **230**(4727), pp. 745–752.

[48] Bolanowski, S. J., Schuyler, J., Sulitka, D., and Pietras, B., 1996, “Mitochondrial distribution within the terminal neurite of the pacinian corpuscle,” Somatosens. Mot. Res., **13**(1), pp. 49–58.

[49] Zelená, J., 1978, “The Development of Pacinian Corpuscles,” J. Neurocytol., **7**(1), pp. 71–91.

[50] Gray, J., and Matthews, P., 1951, “A Comparison of the Adaptation of the Pacinian Corpuscle With the Accommodation of its Own Axon,” J. Physiol., **114**, pp. 454–464.

[51] Sato, M., 1961, “Response of Pacinian Corpuscles to Sinusoidal Vibration,” J. Physiol., **159**, pp. 391–409.

[52] Ozeki, M., and Sato, M., 1965, “Changes in the membrane potential and the membrane conductance associated with a sustained compression of the non-myelinated nerve terminal in Pacinian corpuscles.,” J. Physiol., **180**(1), pp. 186–208.

[53] Gray, J., and Malcolm, J., 1950, “The Initiation of Nerve Impulses by Mesenteric Pacinian Corpuscles,” Proc. R. Soc. B Biol. Sci., **137**(886), pp. 96–114.

[54] Kumamoto, K., Takei, M., Kinoshita, M., Ebara, S., and Matsuura, T., 1993, “Distribution of Pacinian Corpuscles in the Cat Forefoot,” J. Anat., **182**, pp. 23–28.

[55] Paré, M., Smith, A. M., and Rice, F. L., 2002, "Distribution and terminal arborizations of cutaneous mechanoreceptors in the glabrous finger pads of the monkey," J. Comp. Neurol., **445**(4), pp. 347–359.

[56] Halata, Z., Munger, B. L., Hamburg, D. U., Anatomic, F., and Hamburg, F. R. G., 1986, "The Neuroanatomical Basis for the Protopathic Sensibility of the Human Glans Penis," **371**, pp. 205–230.

[57] Schutte, M., Dabezies, E., Zimny, M., and Happel, L., 1987, "Neural Anatomy of the Human Anterior Cruciate Ligament," J. Bone Jt. Surg., **69**(2), pp. 243–247.

[58] Vangsness, C. T., Ennis, M., Taylor, J. G., and Atkinson, R., 1995, "Neural anatomy of the glenohumeral ligaments, labrum, and subacromial bursa," Arthrosc. J. Arthrosc. Relat. Surg., **11**(2), pp. 180–184.

[59] Yahia, L. H., Newman, N., and Rivard, C. H., 1988, "Neurohistology of lumbar spine ligaments.," Acta Orthop. Scand., **59**(5), pp. 508–512.

[60] Kallakuri, S., Li, Y., Chen, C., and Cavanaugh, J. M., 2012, "Innervation of Cervical Ventral Facet Joint Capsule: Histological Evidence," World J. Orthop., **3**(2), pp. 10–4.

[61] Halata, Z., and Groth, H. P., 1976, "Innervation of the Synovial Membrane of the Cats Joint Capsule," Cell Tissue Res., **169**, pp. 415–418.

[62] Halata, Z., 1977, "The Ultrastructure of the Sensory Nerve Endings in the Articular Capsule of the Knee Joint of the Domestic Cat (Ruffini Corpuscles and Pacinian Corpuscles)," J. Anat., **124**(Pt 3), pp. 717–729.

[63] Bowden, R. E. M., 1960, "Innervation of Skeletal Muscle," Br. Med. J., **5174**, pp. 971–974.

[64] Richmond, F. J. R., and Stuart, D. G., 1985, “Distribution of sensory receptors in the flexor carpi radialis muscle of the cat,” J. Morphol., **183**(1), pp. 1–13.

[65] Owaki, M., Oono, H., Nakajima, N., Ohta, G., Okano, S., Kakizaki, T., and Yoshioka, K., 2013, “Morphology and Distribution of Lamellar Corpuscles in the Mesentery of the Cat,” Anat. Histol. Embryol., pp. 3–6.

[66] Shehata, R., 1970, “Pacinian Corpuscles in the Bladder Wall and Outside Ureter of the Cat,” Acta Anat., **77**, pp. 139–143.

[67] Shehata, R., 1972, “Pacinian Corpuscles in Pelvic Urogenital Organsa and Outside Abdominal Lymph Glands of the Cat,” Acta Anat., **83**, pp. 127–138.

[68] García, F. C., Acosta, D. R., Manuel, J., González, D., and Lima, M. S., 2015, “Hyperplasia and Hypertrophy of Pacinian Corpuscles: A Case Report,” Am. J. Dermatopathol., **37**(8), pp. e100–e101.

[69] Roset-Llobet, J., and Domenech-Mateu, J. M., 1991, “Uncommon Number and Distribution of the Pacinian Corpuscles in a Human Hand,” J. Hand Surg. Am., **16B**(1), pp. 89–91.

[70] Brisben, A. J., Hsiao, S. S., and Johnson, K. O., 1999, “Detection of Vibration Transmitted Through an Object Grasped in the Hand,” J. Neurophysiol., **81**, pp. 1548–1558.

[71] Sandzen, S., and Baksic, R., 1974, “Pacinian Hyperplasia,” Hand, **6**(3), pp. 273–274.

[72] Guha, A. R., McMurtrie, A., and Singh, R., 2009, “The Pacinian corpuscle: a method of locating the digital nerve.,” J. Hand Surg. Eur. Vol., **34**(5), pp. 696–7.

[73] Irie, H., Kato, T., Yakushiji, T., Hirose, J., and Mizuta, H., 2011, “Painful

heterotopic pacinian corpuscle in the hand: a report of three cases.," Hand Surg., **16**(1), pp. 81–5.

[74] Ehrmantant, W. R., Graham, W. P., Towfighi, J., Mackay, D. R., and Ehrlich, H. P., 2004, "A histological and anatomical profile of pacinian corpuscles from Dupuytren's contracture and the expression of nerve growth factor receptor.," Plast. Reconstr. Surg., **114**(3), pp. 721–727.

[75] Sathian, K., and Devanandan, M. S., 1983, "Receptors of the metacarpophalangeal joints: a histological study in the bonnet monkey and man.," J. Anat., **137 (Pt 3)**, pp. 601–13.

[76] Lynn, B., 1969, "The nature and location of certain phasic mechanoreceptors in the cat's foot," J Physiol, **201**, pp. 765–773.

[77] Hunt, C. C., 1961, "On the nature of vibration receptors in the hind limb of the cat," J Physiol, **155**, pp. 175–186.

[78] Bouley, D. M., Alarcón, C. N., Hildebrandt, T., and O'Connell-Rodwell, C. E., 2007, "The Distribution, Density and Three-dimensional Histomorphology of Pacinian Corpuscles in the Foot of the Asian Elephant (Elephas maximus) and their Potential Role in Seismic Communication," J. Anat., **211**(4), pp. 428–435.

[79] Rice, F. L., and Rasmusson, D. D., 2000, "Innervation of the Digit on the Forepaw of the Raccoon," J. Comp. Neurol., **490**, pp. 467–490.

[80] Gregory, J. E., McIntyre, A. K., and Proske, U., 1986, "Vibration-evoked responses from lamellated corpuscles in the legs of kangaroos," Exp. Brain Res., **62**(3), pp. 648–653.

[81] Wu, G., Ekedahl, R., Stark, B., Carlstedt, T., Nilsson, B., and Hallin, R. G., 1999,

"Clustering of Pacinian corpuscle afferent fibres in the human median nerve.," Exp. brain Res., **126**(3), pp. 399–409.

[82] Saal, H. P., and Bensmaia, S. J., 2014, "Touch is a team effort: Interplay of submodalities in cutaneous sensibility," Trends Neurosci., **37**(12), pp. 689–697.

[83] Hollins, M., Bensmaia, S. J., and Roy, E. A., 2002, "Vibrotaction and texture perception," Behav. Brain Res., **135**, pp. 51–56.

[84] Weber, A. I., Saal, H. P., Lieber, J. D., Cheng, J.-W., Manfredi, L. R., Dammann, J. F., and Bensmaia, S. J., 2013, "Spatial and temporal codes mediate the tactile perception of natural textures.," Proc. Natl. Acad. Sci. U. S. A., **110**(42), pp. 17107–12.

[85] Manfredi, L. R., Saal, H. P., Brown, K. J., Zielinski, M. C., Dammann, J. F., Polashock, V. S., and Bensmaia, S. J., 2014, "Natural scenes in tactile texture," J. Neurophysiol., **111**(9), pp. 1792–1802.

[86] Westling, G., and Johansson, R. S., 1987, "Responses in glabrous skin mechanoreceptors during precision grip in humans.," Exp. Brain Res., **66**(1), pp. 128–140.

[87] Srinivasan, M. A., Whitehouse, J. M., and LaMotte, R. H., 1990, "Tactile detection of slip: surface microgeometry and peripheral neural codes.," J. Neurophysiol., **63**(6), pp. 1323–1332.

[88] Johnson, K. O., Yoshioka, T., and Vega–Bermudez, F., 2000, "Tactile Functions of Mechanoreceptive Afferents Innervating the Hand," J. Clin. Neurophysiol., **17**(6), pp. 539–558.

[89] Cauna, N., 1965, "The Effects of Aging on the Receptor Organs of the Human

Dermis," Adv. Biol. Skin, **6**, pp. 63–96.

[90] Verrillo, R. T., 1980, "Age Related Changes in the Sensitivity to Vibration," J. Gerontol., **35**(2), pp. 185–193.

[91] Vinik, A. I., Nevoret, M.-L., Casellini, C., and Parson, H., 2013, "Diabetic Neuropathy," Endocrinol. Metab. Clin. North Am., **42**(4), pp. 747–787.

[92] Shun, C. T., Chang, Y. C., Wu, H. P., Hsieh, S. C., Lin, W. M., Lin, Y. H., Tai, T. Y., and Hsieh, S. T., 2004, "Skin Denervation in Type 2 Diabetes: Correlations With Diabetic Duration and Functional Impairments," Brain, **127**(7), pp. 1593–1605.

[93] Alsunousi, S., and Marrif, H. I., 2014, "Diabetic Neuropathy and the Sensory Apparatus 'Meissner Corpuscle and Merkel Cells,'" Front. Neuroanat., **8**, p. 79.

[94] Paré, M., Albrecht, P. J., Noto, C. J., Bodkin, N. L., Pittenger, G. L., Schreyer, D. J., Tigno, X. T., Hansen, B. C., and Rice, F. L., 2007, "Differential Hypertrophy and Atrophy Among All Types of Cutaneous Innervation in the Glabrous Skin of the Monkey Hand During Aging and Naturally Occurring Type 2 Diabetes," J. Comp. Neurol., **501**, pp. 543–567.

[95] Gregersen, G., 1968, "Vibratory Perception Threshold and Motor Conduction Velocity in Diabetics and Non-Diabetics," Acta Med. Scand., **183**(1–6), pp. 61–65.

[96] Whanger, A. D., and Wang, H. S., 1974, "Clinical Correlates of the Vibratory Sense in Elderly Psychiatric Patients," J. Gerontol., **29**(1), pp. 39–45.

[97] Goh, S.-Y., and Cooper, M. E., 2008, "The Role of Advanced Glycation End Products in Progression and Complications of Diabetes," J. Clin. Endocrinol. Metab., **93**(4), pp. 1143–52.

[98] Sims, T. J., Rasmussen, L. M., Oxlund, H., and Bailey, A. J., 1996, "The Role of

Glycation Cross-links in Diabetic Vascular Stiffening," Diabetologia, **39**(8), pp. 946–951.

[99] Aronson, D., 2003, "Cross-linking of Glycated Collagen in the Pathogenesis of Arterial and Myocardial Stiffening of Aging and Diabetes," J. Hypertens., **21**(1), pp. 3–12.

[100] Pallie, W., Nishi, K., and Oura, C., 1970, "The Pacinian Corpuscle, its Vascular Supply and the Inner Core," Acta Anat., **77**, pp. 508–520.

[101] Verzijl, N., DeGroot, J., Zaken, C. B., Braun-Benjamin, O., Bank, R. A., Mizrahi, J., Schalkwijk, C. G., Thorpe, S. R., Baynes, J. W., Bijlsma, J. W., Lafeber, F. P. J. G., and Tekoppele, J. M., 2002, "Crosslinking by Advanced Glycation End Products Increases the Stiffness of the Collagen Network in Human Articular Cartilage," Arthritis Rheum., **46**(1), pp. 114–123.

[102] Reddy, G. K., Stehno-Bittel, L., and Enwemeka, C. S., 2002, "Glycation-Induced Matrix Stability in the Rabbit Achilles Tendon," Arch. Biochem. Biophys., **399**(2), pp. 174–180.

[103] Klaesner, J. W., Hastings, M. K., Zou, D., Lewis, C., and Mueller, M. J., 2002, "Plantar Tissue Stiffness in Patients With Diabetes Mellitus and Peripheral Neuropathy," Arch. Phys. Med. Rehabil., **83**(12), pp. 1796–1801.

[104] Freeman, A., and Johnson, K., 1982, "Cutaneous mechanoreceptors in macacque monkey: temporal discharge patterns evoked by vibration, and a receptor model," J Physiol, **323**, pp. 21–41.

[105] Freeman, A. W., and Johnson, K. O., 1982, "A model accounting for effects of vibratory amplitude on responses of cutaneous mechanoreceptors in Macaque

monkey," J Physiol, **323**, pp. 43–64.

[106] Slavik, P., and Bell, J., 1995, "A Mechanoreceptor Model for Rapidly and Slowly Adapting Afferents Subjected to Periodic Vibratory Stimuli," Math. Biosci., **130**, pp. 1–23.

[107] Bensmaïa, S., 2002, "A transduction model of the Meissner corpuscle," Math. Biosci., **176**(2), pp. 203–217.

[108] Grandori, F., and Pedotti, A., 1980, "Theoretical analysis of mechano-to-neural transduction in Pacinian corpuscle.," IEEE Trans. Biomed. Eng., **27**(10), pp. 559–65.

[109] Güçlü, B., Schepis, E. A., Yelke, S., Yucesoy, C. A., and Bolanowski, S. J., 2006, "Ovoid Geometry of the Pacinian Corpuscle is Not the Determining Factor For Mechanical Excitation," Somatosens. Mot. Res., **23**(3/4), pp. 119–26.

[110] Lesniak, D. R., and Gerling, G. J., 2009, "Predicting SA-I mechanoreceptor spike times with a skin-neuron model," Math. Biosci., **220**(1), pp. 15–23.

[111] Gerling, G. J., and Thomas, G. W., 2008, "Fingerprint lines may not directly affect SA-I mechanoreceptor response.," Somatosens. Mot. Res., **25**(1), pp. 61–76.

[112] Bensmaïa, S., and Hollins, M., 2000, "Complex Tactile Waveform Discrimination," J. Acoust. Soc. Am., **108**(3), pp. 1236–1245.

[113] Bensmaïa, S., Hollins, M., Yau, J., Carolina, N., and Hill, C., 2005, "Vibrotactile intensity and frequency information in the Pacinian system: A psychophysical model," Percept. Psychophys., **67**(5), pp. 828–841.

[114] Choi, S., and Kuchenbecker, K. J., 2013, "Vibrotactile Display: Perception, Technology, and Applications," Proc. IEEE, **101**(9), pp. 2093–2104.

[115] Quindlen, J. C., Lai, V. K., and Barocas, V. H., 2015, “Multiscale Mechanical Model of the Pacinian Corpuscle Shows Depth and Anisotropy Contribute to the Receptor’s Characteristic Response to Indentation,” PLoS Comput. Biol., **11**(9), p. e1004370.

[116] Quindlen, J. C., Bloom, E. T., Ortega, L. E., Moeller, A. T., and Barocas, V. H., 2017, “Micropipette Aspiration of the Pacinian Corpuscle,” J. Biomech.

[117] Lai, V. K., Hadi, M. F., Tranquillo, R. T., and Barocas, V. H., 2013, “A multiscale approach to modeling the passive mechanical contribution of cells in tissues.,” J. Biomech. Eng., **135**(7), p. 71007.

[118] Chandran, P. L., and Barocas, V. H., 2007, “Deterministic material-based averaging theory model of collagen gel micromechanics.,” J. Biomech. Eng., **129**(2), pp. 137–47.

[119] Stylianopoulos, T., and Barocas, V. H., 2007, “Volume-averaging theory for the study of the mechanics of collagen networks,” Comput. Methods Appl. Mech. Eng., **196**(31–32), pp. 2981–2990.

[120] Alford, P. W., and Taber, L. A., 2008, “Computational study of growth and remodeling in the aortic arch,” Comput Methods Biomech Biomed Engin, **11**(5), pp. 525–538.

[121] Ateshian, G. A., Maas, S., and Weiss, J. A., 2013, “Multiphasic finite element framework for modeling hydrated mixtures with multiple neutral and charged solutes.,” J. Biomech. Eng., **135**(11), p. 111001.

[122] Lanir, Y., and Fung, Y. C., 1974, “Two-dimensional mechanical properties of Rabbit skin—II. Experimental results,” J. Biomech., **7**, pp. 171–182.

[123] Silver, F., Freeman, J., and DeVore, D., 2001, “Viscoelastic properties of human

skin and processed dermis," Ski. Res. Technol., **7**, pp. 18–23.

[124] Biswas, A., Manivannan, M., and Srinivasan, M., 2014, "Multiscale Layered Biomechanical Model of Pacinian Corpuscle," IEEE Trans. Haptics, **1412**(c), pp. 1–12.

[125] Pietras, B., and Bolanowski, S., 1992, "Mechanics of the Pacinian Corpuscle: Static and Dynamic Measurements," Proceedings of the 22nd Annual Society for Neuroscience Meeting; 1992 Oct 25-30; Anaheim, CA., p. 829.

[126] Shen, Z. L., Dodge, M. R., Kahn, H., Ballarini, R., and Eppell, S. J., 2010, "In vitro fracture testing of submicron diameter collagen fibril specimens.," Biophys. J., **99**(6), pp. 1986–95.

[127] Welling, L. W., and Grantham, J. J., 1972, "Physical properties of isolated perfused renal tubules and tubular basement membranes.," J. Clin. Invest., **51**(5), pp. 1063–75.

[128] Powell, T. A., Amini, R., Oltean, A., Barnett, V. A., Dorfman, K. D., Segal, Y., and Barocas, V. H., 2010, "Elasticity of the porcine lens capsule as measured by osmotic swelling.," J. Biomech. Eng., **132**(9), p. 91008.

[129] David, G., Pedrigi, R. M., Heistand, M. R., and Humphrey, J. D., 2007, "Regional multiaxial mechanical properties of the porcine anterior lens capsule.," J. Biomech. Eng., **129**(1), pp. 97–104.

[130] Krag, S., and Andreassen, T. T., 2003, "Mechanical properties of the human lens capsule," Prog. Retin. Eye Res., **22**(6), pp. 749–767.

[131] Gray, J. A. B., and Ritchie, M., 1954, "Effects of Stretch on Single Myelinated Nerve Fibres," J. Physiol., **124**, pp. 84–99.

[132] Nishi, K., and Sato, M., 1968, “Depolarizing and hyperpolarizing receptor potentials in the non-myelinated nerve terminal in Pacinian corpuscles,” J Physiol, **199**, pp. 383–396.

[133] Il’inskii, O. B., Volkova, N. K., and Cherepnov, V. ., 1968, “Structure and function of Pacinian corpuscles,” Neurosci. Transl., **2**(2), pp. 637–643.

[134] Biswas, A., Manivannan, M., and Srinivasan, M. a, 2014, “Vibrotactile Sensitivity Threshold: Nonlinear Stochastic Mechanotransduction Model of Pacinian Corpuscle.,” IEEE Trans. Haptics, **1412**(4).

[135] Wang, Y., Marshall, K. L., Baba, Y., Gerling, G. J., and Lumpkin, E. A., 2013, “Hyperelastic Material Properties of Mouse Skin under Compression.,” PLoS One, **8**(6), p. e67439.

[136] Wu, J. Z., Dong, R. G., Smutz, W. P., and Schopper, A. W., 2003, “Nonlinear and viscoelastic characteristics of skin under compression: experiment and analysis,” Biomed. Mater. Eng., **13**, pp. 373–385.

[137] Hendriks, F. M., Brokken, D., Oomens, C. W. J., Bader, D. L., and Baaijens, F. P. T., 2006, “The relative contributions of different skin layers to the mechanical behavior of human skin in vivo using suction experiments,” Med. Eng. Phys., **28**, pp. 259–266.

[138] Flynn, C., Taberner, A., and Pielsen, P., 2011, “Modeling the Mechanical Response of In Vivo Human Skin Under a Rich Set of Deformations,” Ann. Biomed. Eng., **39**(7), pp. 1935–1946.

[139] Oomens, C., and van Campen, D., 1987, “A mixture approach to the mechanics of skin,” J Biomech., **20**(9), pp. 877–885.

[140] Johansson, R., 1978, "Tactile Sensibility in the Human Hand: Receptive Field Characteristics of Mechanoreceptive Units in the Glabrous Skin Area," J. Physiol., **281**, pp. 101–123.

[141] Gould, P. L., 1988, Analysis of Shells and Plates, Springer-Verlag, New York.

[142] Wilkinson, J., 1965, "Natural Frequencies of Closed Spherical Shells," J. Acoust. Soc. Am., **38**, p. 367.

[143] Grevesse, T., Dabiri, B. E., Parker, K. K., and Gabriele, S., 2015, "Opposite rheological properties of neuronal microcompartments predict axonal vulnerability in brain injury.," Sci. Rep., **5**, p. 9475.

[144] Hao, J., and Delmas, P., 2010, "Multiple desensitization mechanisms of mechanotransducer channels shape firing of mechanosensory neurons.," J. Neurosci., **30**(40), pp. 13384–95.

[145] Poole, K., Herget, R., Lapatsina, L., Ngo, H.-D., and Lewin, G. R., 2014, "Tuning Piezo ion channels to detect molecular-scale movements relevant for fine touch," Nat. Commun., **5**, p. 3520.

[146] Dandekar, K., Raju, B. I., and Srinivasan, M. A., 2003, "3-D Finite-Element Models of Human and Monkey Fingertips to Investigate the Mechanics of Tactile Sense," J. Biomech. Eng., **125**(5), p. 682.

[147] Tanaka, Y., Ito, Y., Hashimoto, M., Fukasawa, M., Usuda, N., and Sano, A., 2015, "Collagen fibers induce expansion of receptive field of Pacinian corpuscles," Adv. Robot., **29**(11), pp. 735–741.

[148] Shao, Y., Hayward, V., and Visell, Y., 2016, "Spatial patterns of cutaneous vibration during whole-hand haptic interactions," Proc. Natl. Acad. Sci., **113**(15), pp. 4188–

93.

[149] Checkosky, C. M., and Bolanowski, S. J., 1992, “Effects of stimulus duration on the response properties of Pacinian corpuscles: Implications for the neural code,” J Acoust Soc Am, **91**(6), pp. 3372–3380.

[150] Ranade, S. S., Syeda, R., and Patapoutian, A., 2015, “Mechanically Activated Ion Channels,” Neuron, **87**(6), pp. 1162–1179.

[151] García-Añoveros, J., Samad, T. A., Zuvela-Jelaska, L., Woolf, C. J., and Corey, D. P., 2001, “Transport and Localization of the DEG/ENaC Ion Channel BNaC1alpha to Peripheral Mechanosensory Terminals of Dorsal Root Ganglia Neurons,” J. Neurosci., **21**(8), pp. 2678–2686.

[152] Montaño, J. A., Calavia, M. G., García-Suárez, O., Suarez-Quintanilla, J. A., Gálvez, A., Pérez-Piñera, P., Cobo, J., and Vega, J. A., 2009, “The expression of ENa+C and ASIC2 proteins in Pacinian corpuscles is differently regulated by TrkB and its ligands BDNF and NT-4,” Neurosci. Lett., **463**(2), pp. 114–118.

[153] Calavia, M. G., Montaño, J. A., García-Suárez, O., Feito, J., Guervós, M. A., Germanà, A., Del Valle, M., Pérez-Piñera, P., Cobo, J., and Vega, J. A., 2010, “Differential localization of Acid-sensing ion channels 1 and 2 in human cutaneus pacinian corpuscles,” Cell. Mol. Neurobiol., **30**(6), pp. 841–8.

[154] Cabo, R., Alonso, P., Viña, E., Vázquez, G., Gago, A., Feito, J., Pérez-Moltó, F. J., García-Suárez, O., and Vega, J. A., 2014, “ASIC2 is present in human mechanosensory neurons of the dorsal root ganglia and in mechanoreceptors of the glabrous skin,” Histochem. Cell Biol., **143**(3), pp. 267–276.

[155] Roza, C., Puel, J.-L., Kress, M., Baron, A., Diochot, S., Lazdunski, M., and

Waldmann, R., 2004, “Knockout of the ASIC2 channel in mice does not impair cutaneous mechanosensation, visceral mechanonociception and hearing.,” J. Physiol., **558**(Pt 2), pp. 659–669.

[156] Todd, R., and Bowman, W., 1845, The physiological anatomy and physiology of man, London.

[157] Loewenstein, W., 1956, “Excitation and Changes in Adaptation By Stretch of Mechanoreceptors,” J. Physiol., **133**, pp. 588–602.

[158] Yankner, B. A., Lu, T., and Loerch, P., 2008, “The Aging Brain,” Annu. Rev. Pathol., **3**, pp. 41–66.

[159] Verdú, E., Ceballos, D., Vilches, J. J., and Navarro, X., 2000, “Influence of Aging on Peripheral Nerve Function and Regeneration,” J. Peripher. Nerv. Syst., **5**(4), pp. 191–208.

[160] Wells, C., Ward, L. M., Chua, R., and Inglis, J. T., 2003, “Regional Variation and Changes With Aging in Vibrotactile Sensitivity in the Human Footsole,” J. Gerontol. A. Biol. Sci. Med. Sci., **58**(8), pp. 680–686.

[161] Deshpande, N., Metter, E. J., Ling, S., Conwit, R., and Ferrucci, L., 2008, “Physiological Correlates of Age-Related Decline in Vibrotactile Sensitivity,” Neurobiol. Aging, **29**(5), pp. 765–773.

[162] Era, P., Jokela, J., Suominen, H., and Heikkinen, E., 1986, “Correlates of Vibrotactile Thresholds in Men of Different Ages,” Acta Neurol. Scand., **74**(3), pp. 210–217.

[163] Zelená, J., 1994, Nerves and Mechanoreceptors: the Role of Innervation in the Development and Maintenance of Mammalian Mechanoreceptors, Chapman and

Hall, London.

[164] Zelená, J., 1980, “Rapid Degeneration of Developing Rat Pacinian Corpuscles After Denervation,” Brain Res., **187**(1), pp. 97–111.

[165] Zelená, J., 1982, “Survival of Pacinian Corpuscles After Denervation in Adult Rats,” Cell Tissue Res., **224**, pp. 673–683.

[166] Zelená, J., 1981, “Multiple Innervation of Rat Pacinian Corpuscles Regenerated After Neonatal Axotomy,” Neuroscience, **6**(8), pp. 1675–1686.

[167] Zelená, J., 1984, “Multiple Axon Terminals in Reinnervated Pacinian Corpuscles of Adult Rat,” J. Neurocytol., **13**(5), pp. 665–684.

[168] Bolanowski, S. J., 1984, “Intensity and Frequency Characteristics of Pacinian Corpuscles. III . Effects of Tetrodotoxin on Transduction Process,” J. Neurophysiol., **51**(4), pp. 831–839.

[169] Saal, H. P., Wang, X., and Bensmaia, S. J., 2016, “Importance of spike timing in touch: an analogy with hearing?,” Curr. Opin. Neurobiol., **40**, pp. 142–149.

[170] Wu, J. Z., Dong, R. G., and Welcome, D. E., 2006, “Analysis of the point mechanical impedance of fingerpad in vibration,” Med. Eng. Phys., **28**(8), pp. 816–826.

[171] Dick, D. E., Meyer, J. R., and Weil, J., 1974, “A new approch to quantitation of whole nerve bundle activity,” J. Appl. Physiol., **36**, pp. 393–397.

[172] Fitzpatrick, R., 2013, Oscillations and waves: an introduction, CRC Press.

[173] Dong, Y., Mihalas, S., Kim, S. S., Yoshioka, T., Bensmaia, S., and Niebur, E., 2013, “A simple model of mechanotransduction in primate glabrous skin.,” J. Neurophysiol., **109**(5), pp. 1350–1359.

[174] Saal, H. P., Delhaye, B. P., Rayhaun, B. C., and Bensmaia, S. J., 2017, “Simulating

tactile signals from the whole hand with millisecond precision," Proc. Natl. Acad. Sci., **114**(28), pp. E5693–E5702.

[175] Culling, J. F., and Akeroyd, M. A., 2010, "Spatial hearing," The Oxford Handbook of Auditory Science: Hearing, C.J. Plack, ed., Oxford University Press, Oxford, New York, pp. 123–144.

[176] Moore, D. R., 1991, "Anatomy and Physiology of Binaural Hearing," Audiology, **30**, pp. 125–134.

[177] Ilyinsky, O., 1965, "Process of excitation and inhibition in single mechanoreceptors (Pacinian corpuscles)," Nature, **206**(5008), pp. 351–353.

[178] Tanaka, Y., Ito, Y., Hashimoto, M., Fukasawa, M., Usuda, N., and Sano, A., 2015, "Collagen fibers induce expansion of receptive field of Pacinian corpuscles," Adv. Robot., **29**(11), pp. 735–741.

[179] Aoki, T., Ohashi, T., Matsumoto, T., and Sato, M., 1997, "The pipette aspiration applied to the local stiffness measurement of soft tissues," Ann. Biomed. Eng., **25**(3), pp. 581–7.

[180] Boudou, T., Ohayon, J., Arntz, Y., Finet, G., Picart, C., and Tracqui, P., 2006, "An extended modeling of the micropipette aspiration experiment for the characterization of the Young's modulus and Poisson's ratio of adherent thin biological samples: Numerical and experimental studies," J. Biomech., **39**(9), pp. 1677–1685.

[181] Kee, Y., and Robinson, D. N., 2013, "Micropipette aspiration for studying cellular mechanosensory responses and mechanics," Dictyostelium discoideum Protocols, L. Eichinger, and F. Rivero, eds., Humana Press, Totowa, NJ, pp. 367–382.

[182] Shojaei-Baghini, E., Zheng, Y., and Sun, Y., 2013, "Automated micropipette aspiration of single cells.," Ann. Biomed. Eng., **41**(6), pp. 1208–16.

[183] Zhou, E. H., Lim, C. T., and Quek, S. T., 2005, "Finite Element Simulation of the Micropipette Aspiration of a Living Cell Undergoing Large Viscoelastic Deformation," Mech. Adv. Mater. Struct., **12**(6), pp. 501–512.

[184] Oh, M.-J., Kuhr, F., Byfield, F., and Levitan, I., 2012, "Micropipette aspiration of substrate-attached cells to estimate cell stiffness.," J. Vis. Exp., **67**, pp. 1–7.

[185] Daly, C. H., 1982, "Biomechanical properties of dermis.," J. Invest. Dermatol., **79**, p. 17s–20s.

[186] Dong, C., and Skalak, R., 1992, "Leukocyte Deformability: Finite Element Modeling of Large Viscoelastic Deformation," J. Theor. Biol., **158**(2), pp. 173–193.

[187] Dong, C., Skalak, R., Sung, K. L., Schmid-Schönbein, G. W., and Chien, S., 1988, "Passive Deformation Analysis of Human Leukocytes," J Biomech Eng, **110**(1), pp. 27–36.

[188] Khalilian, M., Navidbakhsh, M., Valojerdi, M. R., Chizari, M., and Yazdi, P. E., 2010, "Estimating Young's Modulus of Zona Pellucida By Micropipette Aspiration in Combination With Theoretical Models of Ovum," J. R. Soc. Interface, **7**(45), pp. 687–94.

[189] Alexopoulos, L. G., Haider, M. A., Vail, T. P., and Guilak, F., 2003, "Alterations in the Mechanical Properties of the Human Chondrocyte Pericellular Matrix with Osteoarthritis," J. Biomech. Eng., **125**(June 2003), pp. 323–333.

[190] Johansson, R., Landstrom, U., and Lundstrom, R., 1982, "Responses of mechanoreceptive afferent units in the glabrous skin of the human hand to sinusoidal

skin displacements," Brain Res., **244**, pp. 17–25.

[191] Cacho, F., Elbischger, P. J., Rodriguez, J. F., Doblare, M., and Holzapfel, G. A., 2007, "A constitutive model for fibrous tissues considering collagen fiber crimp," Int. J. Non. Linear. Mech., **42**(2), pp. 391–402.

[192] Schneider, E. R., Gracheva, E. O., and Bagriantsev, S. N., 2016, "Evolutionary Specialization of Tactile Perception in Vertebrates," Physiology, **31**, pp. 193–200.

[193] Catania, K. C., 2010, "Born knowing: Tentacled snakes innately predict future prey behavior," PLoS One, **5**(6).

[194] Catania, K. C., and Kaas, J. H., 1997, "Somatosensory fovea in the star-nosed mole: Behavioral use of the star in relation to innervation patterns and cortical representation," J. Comp. Neurol., **387**(2), pp. 215–233.

[195] Sawyer, E. K., Leitch, D. B., and Catania, K. C., 2014, "Organization of the spinal trigeminal nucleus in Star-Nosed Moles," J Comp Neurol, **522**(14), pp. 3335–3350.

[196] Cunningham, S. J., Castro, I., Jensen, T., and Potter, M. A., 2010, "Remote touch prey-detection by Madagascar crested ibises Lophotibis cristata urschi," J. Avian Biol., **41**(3), pp. 350–353.

[197] Schneider, C. a, Rasband, W. S., and Eliceiri, K. W., 2012, "NIH Image to ImageJ: 25 years of image analysis," Nat. Methods, **9**(7), pp. 671–675.

[198] Catania, K. C., Leitch, D. B., and Gauthier, D., 2010, "Function of the appendages in tentacled snakes (Erpeton tentaculatus).," J. Exp. Biol., **213**(3), pp. 359–367.

[199] Gottschaldt, K. M., 1974, "The Physiological Basis of Tactile Sensibility in the Beak of Geese," J Comp Physiol, **95**, pp. 29–47.

[200] Gottschaldt, K. M., and Lausmann, S., 1974, "Mechanorceptors and Their Properties

in the Beak Skin of Geese," Brain Res., **65**, pp. 510–515.

[201] Putterill, J. F., and Soley, J. T., 2003, "General Morphology of the Oral Cavity of the Nile Crocodile, Crocodylus niloticus (Laurenti, 1768). I. Palate and gingivae," Onderstepoort J. Vet. Res., **70**(4), pp. 281–97.

[202] Rico, B., Solas, M. T., Clément, J., Suárez, I., and Fernández, B., 1996, "Ultrastructural Study of the Pacinian Corpuscles in the Newborn and Adult Dog Forefoot," Eur. J. Morphol., **34**(4), pp. 311–320.

[203] Crole, M. R., du Plessis, L., and Soley, J. T., 2015, "Morphological Features of Herbst Corpuscles in the Oropharynx of the Ostrich (Struthio camelus) and Emu (Dromaius novaehollandiae)," Anat. Rec., **298**(5), pp. 783–796.

[204] von Düring, M., and Seiler, W., 1974, "The Fine Structure of Lamellated Receptors in the Skin of Rana Esculenta," Z. Anat. Entwicklungsgesch., **144**(2), pp. 165–172.

[205] Gottschaldt, K. M., and Lausmann, S., 1974, "The Peripheral Morphological Basis of Tactile Sensibility in the Beak of Geese," Cell Tissue Res., **153**, pp. 477–496.

[206] Marasco, P. D., Tsuruda, P. R., Bautista, D. M., and Catania, K. C., 2007, "Fine Structure of Eimer's Organ in the Coast Mole (Scapanus orarius)," Anat. Rec., **290**(5), pp. 437–448.

[207] Organ, J. M., Muchlinski, M. N., and Deane, A. S., 2011, "Mechanoreceptivity of Prehensile Tail Skin Varies Between Ateline and Cebine Primates," Anat. Rec., **294**(12), pp. 2064–2072.

[208] Albuerne, M., De Lavallina, J., Esteban, I., Naves, F. J., Silos-Santiago, I., and Vega, J. a, 2000, "Development of Meissner-like and Pacinian sensory corpuscles in the mouse demonstrated with specific markers for corpuscular constituents.," Anat.

Rec., **258**(3), pp. 235–42.

[209] Prahl, S., Huggenberger, S., and Schliemann, H., 2009, "Histological and Ultrastructural Aspects of the Nasal Complex in the Harbour Porpoise, Phocoena phocoena," J. Morphol., **270**(11), pp. 1320–1337.

[210] Winkelmann, R. K., and Myers, T. T., 1961, "The histochemistry and morphology of the cutaneous sensory end-organs of the chicken," J. Comp. Neurol., **117**(1), pp. 27–35.

[211] Kuriyama, T., Brandley, M. C., Katayama, A., Mori, A., Honda, M., and Hasegawa, M., 2011, "A time-calibrated phylogenetic approach to assessing the phylogeography, colonization history and phenotypic evolution of snakes in the Japanese Izu Islands," J. Biogeogr., **38**(2), pp. 259–271.

[212] Feldman, A., and Meiri, S., 2013, "Length – mass allometry in snakes," Biol. J. Linn. Soc., **108**, pp. 161–172.

[213] Nishida, Y., Yoshie, S., and Fujita, T., 2000, "Oral sensory papillae, chemo- and mechano-receptors, in the snake, Elaphe quadrivirgata. A light and electron microscopic study.," Arch. Histol. Cytol., **63**(1), pp. 55–70.

[214] Berta, A., Ekdale, E. G., Zellmer, N. T., Deméré, T. A., Kienle, S. S., and Smallcomb, M., 2015, "Eye, Nose, Hair, and Throat: External Anatomy of the Head of a Neonate Gray Whale (Cetacea, Mysticeti, Eschrichtiidae)," Anat. Rec., **298**(4), pp. 648–659.

[215] Guharay, F., and Sachs, F., 1984, "Stretch-activated single ion channel currents in tissue-cultured embryonic chick skeletal muscle," J. Physiol., **352**, pp. 685–701.

[216] Erxleben, C., 1989, "Stretch-activated Current through Single Ion Channels in the

Abdominal Stretch Receptor Organ of the Crayfish," J. Gen. Physiol., **94**, pp. 1071–1083.

[217] Kim, S. S., Sripati, A. P., and Bensmaia, S. J., 2010, "Predicting the Timing of Spikes Evoked by Tactile Stimulation of the Hand," J Neurophysiol, **104**, pp. 1484–1496.

[218] Dong, Y., Mihalas, S., Kim, S. S., Yoshioka, T., Bensmaia, S., and Niebur, E., 2013, "A simple model of mechanotransduction in primate glabrous skin.," J. Neurophysiol., **109**(5), pp. 1350–1359.

[219] Lesniak, D. R., Wellnitz, S. a, Gerling, G. J., and Lumpkin, E. a, 2009, "Statistical analysis and modeling of variance in the SA-I mechanoreceptor response to sustained indentation.," Conf. Proc. IEEE Eng. Med. Biol. Soc., **2009**, pp. 6814–7.